
Modelling, Control and Stability Analysis of an RF Cavity in CERNs LINAC4

Martin Søndergaard Andersen

Master's Thesis



Aalborg University and CERN
Control & Automation



AALBORG UNIVERSITY

STUDENT REPORT

Department of
Automation & Control
Control & Automation
Fredrik Bajers Vej 7C
DK-9000 Aalborg
www.es.aau.dk

Title:

Modelling, Control and Stability Analysis of an RF Cavity in CERNs LINAC4

Theme:

Master's Thesis

Semester:

10th semester Control & Automation

Project Period:

Spring semester 2020

Project Group:

CA10-1038

Author:

Martin Søndergaard Andersen

Supervisors:

Jan Dimon Bendtsen
dimon@es.aau.dk

Bartosz Przemysław Bielawski
bartosz.bielawski@cern.ch

Report:

104 pages

Submitted:

June 3, 2020

Abstract:

This thesis set out to explore ways to optimize cavity control loops for CERNs LINAC4 linear particle accelerator. It was found that most RF cavities in linear particle accelerators in the world modelled the cavity as a first order low pass filter, and used either PI or LQ Regulators to correct for beam loading.

This thesis modelled the RF accelerating cavity as a 2nd order system, which were able to describe the dynamics of the voltage in the cavity better than the first order model generally used. The thesis also designed a Kalman observer for delay handling, an LQR controller for beam loading correction and conducted a stability analysis of the designed closed loop system.

It was found, that including delayed states in the Kalman predictor, can make the Kalman observer predict current states given delayed output measurements. It was also found that including an estimate of the effect to the voltage during beam loading in the input to the Kalman filter vastly improved the response to beam loading in terms of reaction time, undershoot and settling time. Lastly it was found during the stability analysis that, depending on the controller tune, the model parameters can vary at least up to 25% of the real cavity before the system becomes unstable.

Contents

Reading Guide	vi
1 Introduction	1
1.1 Introduction to Particle Physics	1
1.2 CERNs Accelerator Complex	2
1.3 Accelerating particles using RF cavities	4
1.4 Current Strategies for Cavity Control Loops	7
1.5 Thesis Delimitation	8
2 Modelling	9
2.1 1st Order Modelling of a Particle Accelerating RF Cavity	10
Discretisation	19
2.2 Modelling a Particle Accelerating RF Cavity as a 2nd Order System	19
Discretisation	22
2.3 Noise Analysis in Voltage measurement	23
2.4 Model Verification	27
3 Summary of Internship Project	33
3.1 Cavity Control Loop Optimisation	33
3.2 Comparison of Full State and Single State Feedback in Simulation	34
Results	35
3.3 LINAC4 cavity testing	37
PIMS0304 Cavities	37
CCDTL0506 Cavities	40
4 Control Design	44
4.1 Kalman Estimation of Voltage in LINAC4 RF Cavity	44
4.2 Verification of Kalman Voltage Estimator	50
Kalman Verification Using Model of System	50
Kalman Verification Using CCDTL7 Open Loop Data	55
4.3 LQR Regulator for Cavity Voltage Control	57
Adding Integral Control	58
Choosing Q and R	59

5	Simulation	61
5.1	Simulation Environment	61
5.2	Simulating LQR Response to Beam Loading	62
5.3	Including Beam Loading in Kalman Estimator Input	66
6	Stability Analysis	70
6.1	Controller Gain Stability	70
6.2	Model Parameter Variation	74
7	Evaluation	79
7.1	Conclusion	79
7.2	Future Work	80
	Bibliography	82
A	Interfacing with LINAC4	84
A.1	Introduction to Interfacing with CERNs Accelerators	84
A.2	FESA Classes, PyJapc and Navigators	87
B	Python Control Toolbox	90
B.1	Implementation of a Python Toolbox for Calculating Kalman Gain	91
B.2	Implementation of a Python Toolbox for Calculating LQ Controller Gain	92
B.3	Kalman Gain Code	93
B.4	LQ Gain Code	93
C	LINAC4 Commisioning	95
C.1	Commissioning of LINAC4	95
D	Modelling	99
D.1	Modelling a Particle Accelerating RF Cavity as a 2nd Order System	99

PREFACE

This thesis is written to document the work conducted by the author on 10th semester Control & Automation at Aalborg University. This thesis is a result of a collaboration between the author and the European Organisation for Nuclear Research (CERN) during the spring semester 2020. This project builds on top of an academic internship project conducted by the author in the fall semester 2019 at CERN and therefore some figures, knowledge and experiences from that project are included in this thesis where relevant. The internship project was titled “Cavity Control Loop Optimisation For CERNs LINAC4 Linear Particle Accelerator” [1].

The author would like to thank Jan Dimon Bendtsen, Associate Professor at Aalborg University for his extensive guidance throughout the creation of this Master’s Thesis. The author would also like to thank the assigned supervisor at CERN, Bartosz Bielawski for his help and great insight in the system and LINAC4 LLRF control loops. The author would also like to acknowledge Robert Borner and Philippe Baudrenghien, both CERN Staff for their insight into the control theory applied in the LINAC4 cavity control loops.

Aalborg University, June 3, 2020



Martin Andersen

`martan15@student.aau.dk`

READING GUIDE

This thesis begins with an *Introduction* chapter, introducing particle physics, CERN and how particles are being accelerated in RF cavities around the world. The *Modelling* chapter models and RF accelerating cavity both as a first and second order model. It also investigates the noise characteristics of the voltage signals from the cavities before verifying the derived models. Following this, the *Summary of Internship Project* chapter summarises a previous project conducted by the author of this thesis at CERN, as some of the findings from that project are used to design control strategies in this thesis. After this the *Control Design* chapter designs a Kalman observer for handling a measurement delay, and LQR controllers are designed based on the Kalman estimations. The *Simulation* chapter sets up a simulation environment and tests the designed controllers to verify they are in fact regulating as intended. A stability analysis of the system and the designed control strategies are done in the *Stability Analysis* chapter, before the thesis' conclusion is made in the *Evaluation* chapter.

The *Appendix* presents chapters not directly relevant to the content of this thesis, but presents context for more in depth interaction with the LINAC4 machine, Implementation of control algorithms in python. It also presents another version of the second order model where the complex terms are kept.

This thesis will number figures and tables as X.X related to the chapter they are located. Citations are put in square brackets as [x], where x is a number referring to a specific source in the bibliography. A citation placed after a full stop at the end of a paragraph applies to the whole paragraph. If placed before a full stop, it only applies to the sentence in which it is placed. Periods are used as the decimal separator.

INTRODUCTION

1.1 INTRODUCTION TO PARTICLE PHYSICS

In 1929 Edwin Hubble made the observation that galaxies are moving away from each other. This backed up Georges Lemaître's Big Bang Theory formulated in 1927. Ever since that first observation, particle physics has been and are continuing to be an ever so important study of the fundamentals of the universe [2].

Particle physics is a branch within physics studying the fundamental particles of the universe. Particle physicists seek to find a model describing the entire universe. This involves discovering what gives particles mass, what gravity is, how it works, what the universe is made of and how the universe came into existence? This is no simple task and often require very large, expensive and specialised equipment to study. Starting in the 1950s up through the 60s and 70s particle physics and high energy nuclear physics became a high priority field of study within physics. In this period some of the worlds largest particle physics research institutions (DESY, Fermilab and CERN) all started. These institutions have been investigating and trying to find the fundamental particles that make up the universe which have then been compiled into the Standard Model. The standard model describes the elemental particles of mass and elemental forces. The elementary particles of mass, also defined as the building blocks of matter, are separated into two categories - Quarks and Leptons. Both categories contain six particles connected in 3 generations. The first generation of quarks, "up" and "down" quarks, are the lightest and most stable mass particles. The higher the generation, the heavier the particles are and the less stable they are. This means the higher generation quarks will at some point decay into the first generation [3]. The standard model is considered to be the most accurate description of subatomic behaviour currently, yet it only describes approximately 4% of the known masses, forces and particles in the universe [3]. The standard model does not describe 1 of the 4 elementary forces, namely gravity, as the particle believed to be the carrier for the gravitational force is yet to be discovered. It also does not have explanations of the concepts of "dark matter" or "dark energy" believed to take up around 26% and 70%, respectively, of the mass-energy content of the universe [2].

An achievement worth mentioning is the recent discovery and detection of the Higgs boson in 2012 at CERN. The Higgs boson was included as an addition to the Standard Model to explain, how the electroweak force (a combination of two of the fundamental forces - weak and electromagnetic force) and its carrying force-particles W and Z bosons does in fact have a mass. This would not be the case without the Higgs field added to the Standard Model. Although very interesting, particle physics is not directly the focus of this thesis, and therefore more information on the standard model, Higgs boson and more can be found in [4].

What is however the focus of this thesis is the infrastructure and machines making discoveries like the Higgs boson possible. CERN is the largest particle physics research institution in the world and have the worlds largest particle accelerator complex. CERN is located on the border between Switzerland and France near Geneva, Switzerland. The next section 1.2 will give an overview of the different machines and the chain of particle accelerators used at CERN, before section 1.3 will give a detailed introduction to particle acceleration and how it is done using RF cavities. Lastly section 1.5 will specify scope of this thesis.

1.2 CERNs ACCELERATOR COMPLEX

The CERN accelerator complex is made up of a chain of particle accelerators and a multitude of experiments. This section will merely highlight the most known

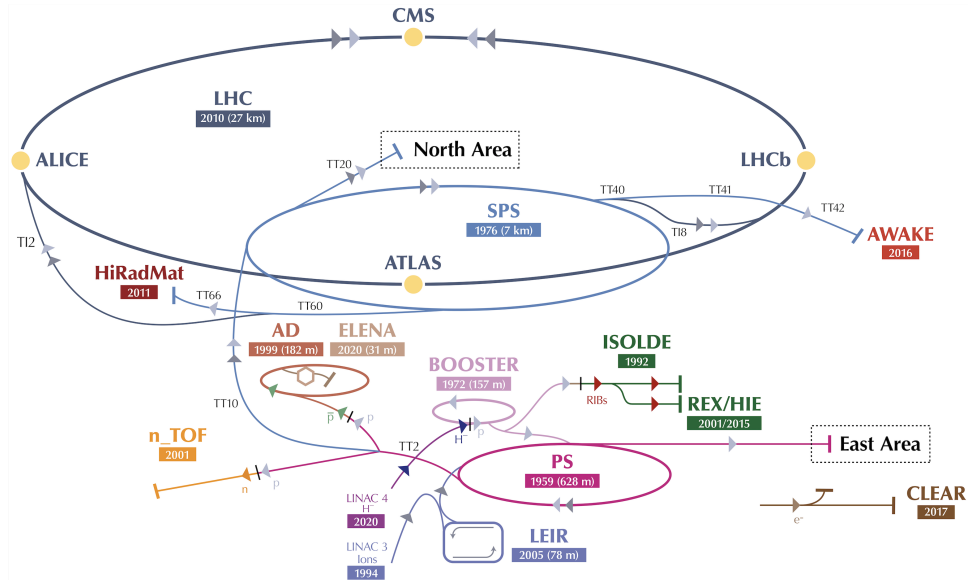


Figure 1.1: Figure outlining CERNs complete accelerator complex. It shows all the accelerators and experiments at CERN, and how the particles travel from LINAC4, through the BOOSTER, PS and SPS before entering the LHC for head on collisions. [5]

accelerators and describe the ones relevant for this thesis. Currently the largest and most well known machine at CERN is the Large Hadron Collider (LHC). It has 4 experiments placed at 4 different points on the 27km ring. In the LHC particles travel very close to the speed of light being accelerated by RF cavities. RF cavities uses a dynamically oscillating electric fields to accelerate particles. This will be explained in further detail in the following section 1.3. The protons collide at four points in the LHC which correspond to the 4 experiments highlighted as yellow dots in figure 1.1. The four experiments (detectors) are called ATLAS, CMS, ALICE and LHCb. Pictures of the two largest detectors, CMS and ATLAS, can be seen in the following figure 1.2.



(a) Image taken of the CMS detector. It is opened up in sections during the long shut-down period for upgrades and repairs.



(b) The ATLAS detector is CERNs largest detector. In this image the detector is opened up for upgrades and repairs.

Figure 1.2

Particle beams, which is a group of particles under acceleration bunched together to a certain size, travel in two tubes (beam pipes) clockwise and anti clockwise. The beam pipes intersect each other at the four before mentioned colliding points. However, the LHC is not the only machine responsible for the acceleration of the particles. This happens in several stages in several machines. The particles due to be accelerated are initiated from a source of hydrogen becoming H⁻ ions in the beginning of the Linear Accelerator 4 (LINAC4). LINAC4 is a new addition to the

accelerator complex as it replaces LINAC2 (LINAC3 is still in operation) during the Long Shutdown 2 2019-2020 (LS2), in order to support the long term goal of increasing the energy in the accelerator complex. The H^- ions are accelerated through LINAC4 up to 160 MeV. This happens in several different stages in the LINAC, as there are multiple different types of cavities. Firstly the particles are accelerated to 3 MeV in a radio frequency quadrupole (RFQ). The particles then enter a group of cavities called Drift Tube Linacs (DTLs) where they are accelerated to 50 MeV, before they enter the next group of cavities, namely the Cell-Coupled Drift Tube Linacs (CCDTLs). Lastly they are accelerated to 160 MeV through Pi-Mode structures (PIMS). [6]

After the H^- ions have been accelerated through the entire LINAC4, they are stripped of their 2 electrons at injection to the Proton Synchrotron Booster (PSB), marked with just “BOOSTER” in figure 1.1. From this point on, the particle beam consists of pure proton beams. The booster is an accelerator of 4 rings stacked on top of each other, creating 4 bunches and accelerates them to 1.4 GeV [7]. After the booster, the protons go into the Proton Synchrotron (PS), where they are accelerated to 25 GeV before they are injected into the Super Proton Synchrotron (SPS) to be accelerated to 450 GeV. The SPS is the final machine in the chain before the particle beams enter the LHC, where they will have reached an almost constant velocity of close to the speed of light. The protons are accelerated to 6.5 TeV per beam in the LHC, making the final collision energy around 13 TeV. Apart from LINAC4 the energies mentioned in this section are based on the last run of the LHC in 2018 [7]. Currently CERN is undergoing one of the largest upgrade projects yet, to reach what is called the High-Luminosity LHC (HL-LHC). This involves upgrading almost all the accelerators in the accelerator chain described, to reach even higher accelerating energies and also increase the number of particle collisions by a factor of 5-7, when the HL-LHC in 2027 is expected to start up [8].

1.3 ACCELERATING PARTICLES USING RF CAVITIES

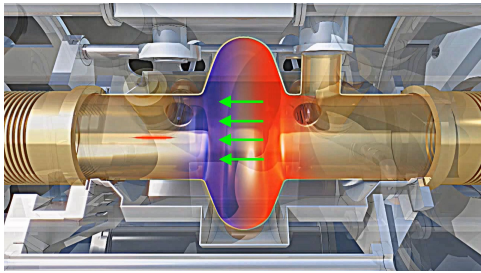
In the previous section 1.2, it was explained how the particles travel through the chain of accelerators before collisions in the LHC. This section will dive into the process of particle acceleration and give an introduction to the concepts behind and different methods for doing so.

Although this thesis focuses on linear accelerators, this section will explain the basics of RF particle acceleration using a single cell superconducting cavity in the LHC for illustrational purposes. Also, in CERN's accelerator complex several particles are used for example protons, electrons, lead-ions and more, and although the theory for accelerating these are similar, this section will describe the concept of accelerating positively charged protons.

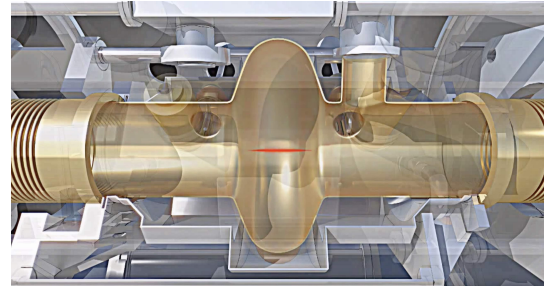
Electric fields are used to accelerate charged particles. Two types of fields can be used for acceleration: an electrostatic field and a dynamic/oscillating electric field. An electrostatic field is a field where DC power is used, and the electrical polarity remains constant. This creates an electric field between two charge potentials with a fixed acceleration direction. An electrostatic field has a downside to particle acceleration. Although the field is constant and particles can be constantly accelerated through the field, it becomes difficult to scale, as higher constant voltage differences often results in discharging sparks. Therefore electrostatic fields used for acceleration is often limited to a few MeV. [9, 10]

Instead, by using RF power in a resonating cavity resulting in an oscillating electric field, this limit can be overcome, as the cavity resonance functions as an amplifier. By using oscillating RF power with the correct timing, the electric field will “push” the particles to accelerate them. The polarity of the field will reverse just before the particles enter the cavity to minimise the deceleration of the particles. This is illustrated in figure 1.3, where the particle beam is depicted as a red horizontal line in the centre of the beam pipe. The cavity itself is illustrated as the oval shape in the middle of the beam pipe. In figure 1.3a the positively charged protons are travelling towards the cavity. The electric field (green arrows) is facing towards the beam and has just passed its peak strength. As the beam enters the cavity, the polarity is reversed leaving a small time slot with a non existing to weak electric field as illustrated in figure 1.3b. Just as the entire beam passes the centre point of the cavity, the field is again growing in intensity and pushing the beam away and thereby accelerating it. [10]

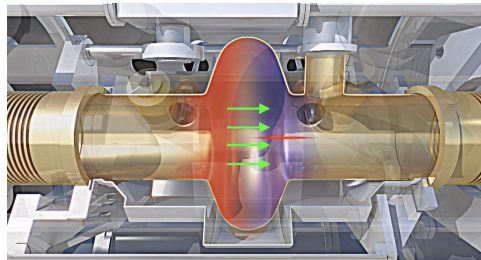
Timing the RF oscillation in a cavity is crucial for keeping a continuous acceleration going as just explained. Timing also has another very important property, namely bunching of the beam. Bunching is the process of compressing the particle beam to a certain size in the longitudinal plane. The specific bunching depends on several design parameters, such as desired bunch length, number of RF buckets etc.. Until now, the oscillation of the electric field in the cavity has been explained as changing electrical polarity. In reality this happens by supplying the cavity with a sinusoidal RF power signal, which makes the voltage in the cavity oscillate around 0 V, with some amplitude, frequency and phase. In figure 1.4 three different scenarios are outlined for when a bunch arrives and what effect it has on the acceleration and behaviour of the particles in the bunch. The individual particles in a bunch has different velocities and energies. The first particles to arrive to the cavity are the fastest ones with the highest energy. If a bunch arrives prior to the peak of the electric field, as shown in figure 1.4a, the fastest arriving particles will be accelerated less and thereby to a lower energy than the slowest arriving particles. The slowest arriving particles sees a stronger field, and thereby gains more energy, causing a bunching effect and compresses the particles closer together. In the case where the centre of the particle bunch lines up with the peak strength of the electric field, as



(a) Beam travelling towards cavity cell. At this point the beam is outside the accelerating cell, the electric field just passed its peak strength and the accelerating direction (green arrows) is pointing towards the beam.



(b) The polarity of the field changes just when the particles enter the cavity. At this point the electric field is at its minimum, and the beam is not accelerated or decelerated.



(c) As soon as the beam passes the middle of the cavity, the electric field grows in intensity and pushes the beam along the direction of the electric field (green arrows).

Figure 1.3: Illustration of the particle acceleration process in an RF cavity [11].

shown in Fig. 1.4b, it will cause the bunch to be split in two smaller bunches. If the bunch of particles arrive after the peak magnitude of the field, the fastest arriving particles will see the strongest field, and get accelerated even more than the slower arriving particles, as shown in figure 1.4c. Therefore, the desirable option in particle accelerators is often the case where the bunch arrives before the peak strength of the electric field causing the slowest particles to be accelerated more than the fastest part of the bunch. This allows the slower particles to catch up and thereby compressing the bunch. The process of aligning the bunch arrival with the cavity frequency is called phasing, and will not be covered any further. This section is merely meant as an introduction to particle acceleration.

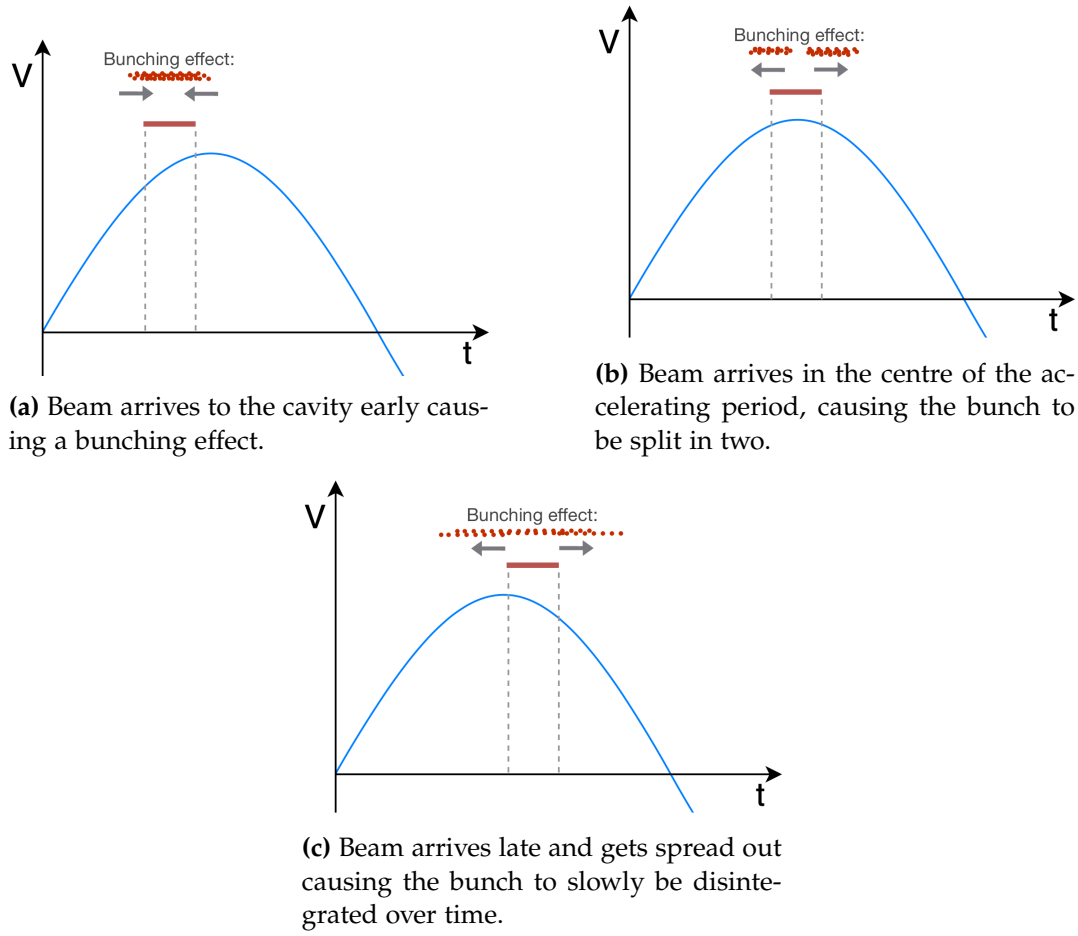


Figure 1.4: Illustrating the timing of beam arrival effects on acceleration.

1.4 CURRENT STRATEGIES FOR CAVITY CONTROL LOOPS

To accelerate particles evenly through a cavity in a linear particle accelerator, the voltage amplitude has to be kept constant. This requires control strategies to be implemented to keep the voltage in the cavity constant, even when charged particles pass through and absorb some of the energy stored in the cavity. Both [12], [13] and [14] model the cavity as a first order low pass filter and find it to be a well enough fit to describe the cavity dynamics. [13] and [14] design PI regulators to stabilise the voltage in the cavity, and achieve this without any steady state errors. [14] also finds that a derivative element in the regulator is not needed, and that the proposed PI regulator is able to keep the cavity operating under stable conditions. [15] proposes a feedback controller based on a designed Active Disturbance Rejection Control (ADRC) observer as a replacement to PI control. It shows promise of

being able to detect beam loading and correct for it, and the authors also propose the ADRC disturbance observer to be used for model identification.

[16] outlines the newest developments in control systems relating to the LINAC4 machine at CERN. The authors explain the cavity modelled as a first order low pass filter, and that LQ Regulators are able to improve the feedback regulator to minimise effect of beam loading. The authors also describe an Adaptive Feedforward Filter (AFF), which is able to learn to correct for beam loading given information on the exact time when the beam enters the cavity. Both the LQ regulator and AFF are able to improve the response greatly in terms of disturbance rejection compared to a PI controller. Findings outlined in this article form the basis of this thesis investigation, and aims to further improve the control strategies for LINAC4.

1.5 THESIS DELIMITATION

CERNs accelerator complex is currently undergoing large upgrades to meet energy and luminosity levels for the upcoming HL-LHC in 2027. LINAC4 is the newest linear accelerator replacing the previous LINAC2. LINAC4 will be capable of accelerating particles up to energies of 160 MeV compared to LINAC2s 50 MeV.

This thesis will focus on optimising cavity control loops for the LINAC4 accelerator. The main objective of this thesis is to investigate methods of making the control system respond to process noise (in this case the effect of beam loading) quickly.

The scope of the thesis is therefore to model an RF accelerating cavity, design a Kalman observer to handle time delays in a very fast system and to design and test LQR controllers. A stability analysis of the designed control strategies will also be made, to gain insight into how fast the control system can be tuned while the system remains stable.

This thesis is a continuation of an internship project of the same author and the project is titled “Cavity Control Loop Optimisation For CERNs LINAC4 Linear Particle Accelerator”. This project investigated how the already implemented control structures could be optimised in terms of computational complexity without losing performance. Findings from this project will be used in this thesis and form a basis for modelling and control design. A full summary of the project is presented in chapter 3.

MODELLING

This chapter will model a particle accelerating RF cavity in two different ways. The aim is to find an expression for the voltage in a cavity during operation. Modelling is similar for cavities for both linear and circular accelerators, but this chapter will model a cavity based on CERNs LINAC4 machine. A cavity in a linear accelerator is of second order, however currently most LINACs around the world are modelled as a first order system due to its simplicity. As this project investigates ways to optimise cavity control loops for CERNs LINAC4, which is currently designed to be a 1st order system, this chapter will model the cavity as both a 1st order and a 2nd order system for comparison. Overall the system surrounding a cavity loop can be illustrated as in figure 2.1, where a klystron (type of amplifier) is generating the necessary RF power being sent to the RF accelerating cavity via transmission lines with impedance Z . If a cavity is not perfectly matched on its resonance frequency and RF frequency, some power may be reflected back from the cavity. Therefore a circulator is placed between the klystron and the cavity to redirect the reflected power to a load instead of it going back into and destroying the klystron. For the modelling of an RF accelerating cavity in this chapter a cavity on tune is assumed, and therefore only the cavity itself coupled with the transmission line is modelled omitting the Klystron, Circulator and load.

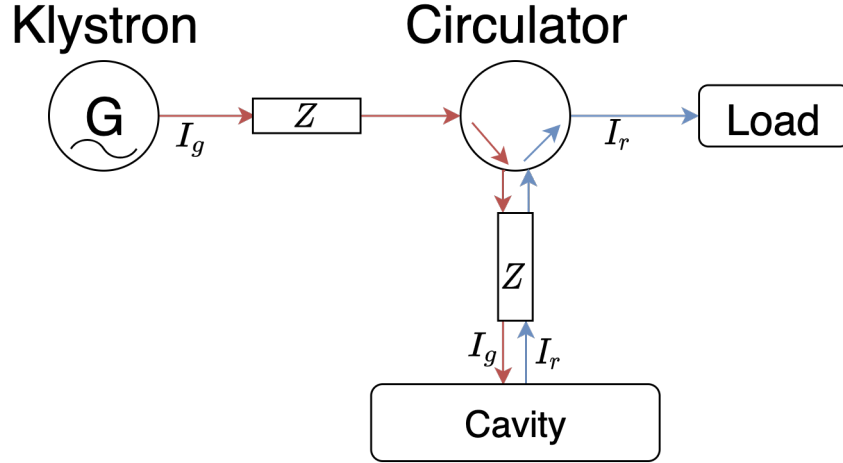


Figure 2.1: Illustration of overall cavity loop. Power is being generated in a Klystron (amplifier) and sent to the cavity via transmission lines with impedance Z . A circulator is added to redirect the generated current I_g to the cavity and the reflected current I_r from the cavity to a load, in order to not damage the Klystron.

Section 2.1 will derive the 1st order model, and section 2.2 will derive the 2nd order model. Section 2.3 will analyse the measurement noise in the system to gain to investigate if a model of the noise is necessary, and lastly section 2.4 will verify all the derived models.

2.1 1ST ORDER MODELLING OF A PARTICLE ACCELERATING RF CAVITY

The modelling in this section will be based on [12], but with a slightly different notation and progression.

A cavity is supplied with an RF wave, and can be modelled as a parallel LCR circuit as shown in figure 2.2. The cavity is being supplied by the I_g generator current coming from a klystron as illustrated in figure 2.1. I_r is the reflected wave current, I_b is the induced beam loading current, L is the inductance property of the cavity, R is the resistivity of the cavity, C is the capacitance and Z is the impedance on the transmission line transmitting the power from the klystron to the cavity.

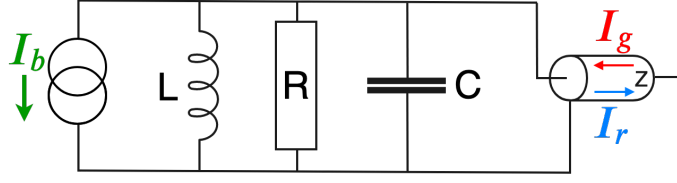


Figure 2.2: Circuit model of the cavity coupled with the transmission line with impedance Z . Here I_g is the generator current to the cavity, I_r is the reflected wave current, L is the inductance, C is the capacitance and R is the resistance. I_b is the current induced by the beam loading.

Starting off with describing the current through the circuit:

$$I_{LCR} = I_g - I_r - I_b \quad (2.1)$$

Given that it is a parallel circuit, the voltage is the same at any point in the line, and can be defined by the forward V_{forw} and reflected V_{refl} :

$$V = V_{forw} + V_{refl} = Z(I_g + I_r)$$

$$I_r = \frac{V}{Z} - I_g \quad (2.2)$$

Substituting equation 2.2 in equation 2.1 makes the reflected wave current I_r disappear:

$$I_{LCR} = I_g - \left(\frac{V}{Z} - I_g \right) - I_b$$

$$I_{LCR} = 2I_g - I_b - \frac{V}{Z} \quad (2.3)$$

For each of the three LCR components there exists relations for both voltage and current. For the inductor, the relations between $V_L(t)$ and $I_L(t)$ are given by:

$$V_L(t) = L \frac{dI_L(t)}{dt} \quad (2.4)$$

$$I_L(t) = \frac{1}{L} \int V_L(t) dt + I_0 \quad (2.5)$$

$V_L(t)$ is the voltage over the inductor, $I_L(t)$ is the current through the inductor and I_0 is the initial current flowing through the inductor, which in this case is neglected as there is no initial current.

For the resistor the following relations hold, where R is the resistance:

$$V_R(t) = RI_R(t) \quad (2.6)$$

$$I_R(t) = \frac{V_R(t)}{R} \quad (2.7)$$

Lastly for the capacitor, following relations are used:

$$V_C(t) = V_0 + \frac{1}{C} \int I_C(t) dt \quad (2.8)$$

$$I_C(t) = C \frac{dV_C(t)}{dt} \quad (2.9)$$

Here V_0 is also an initial 'state' representing the voltage over the capacitor at $t = 0$. As there is no voltage in the cavity initially this is neglected.

In a parallel circuit the voltage over each component is equal:

$$V(t) = V_L(t) = V_C(t) = V_R(t) \quad (2.10)$$

And the total current through the system is also the sum of currents going through all the components in the LCR lump:

$$I_{LCR}(t) = I_L(t) + I_C(t) + I_R(t) \quad (2.11)$$

Inserting the relations in equations 2.5, 2.7 and 2.9 for current through each component into equation 2.11 results in:

$$I_{LCR}(t) = \frac{1}{L} \int V(t) dt + C \frac{dV(t)}{dt} + \frac{V(t)}{R} \quad (2.12)$$

Two expressions for I_{LCR} has now been found in equation 2.3 and 2.12, combining them will give:

$$\begin{aligned}
2I_g(t) - I_b(t) - \frac{V(t)}{Z} &= \frac{1}{L} \int V(t)dt + C \frac{dV(t)}{dt} + \frac{V(t)}{R} \\
2I_g(t) - I_b(t) &= \frac{1}{L} \int V(t)dt + C \frac{dV(t)}{dt} + V(t) \left(\frac{1}{R} + \frac{1}{Z} \right)
\end{aligned} \tag{2.13}$$

From equation 2.13 it is evident that expressions for both $V(t)$, $\frac{dV(t)}{dt}$ and $\int V(t)dt$ are needed. The circuit is AC and the voltage is given by the complex-valued function [12]:

$$V(t) = A(t)e^{i\omega t} \tag{2.14}$$

Here $A(t)$ is the amplitude of the oscillating voltage, ω is the angular frequency. Based on this expression for $V(t)$, $\frac{dV(t)}{dt}$ and $\int V(t)dt$ can be found. Starting with $\frac{dV(t)}{dt}$ using the product rule $\frac{d(uv)}{dt} = u \frac{dv}{dt} + v \frac{du}{dt}$:

$$\begin{aligned}
\frac{dV(t)}{dt} &= A(t) \frac{de^{i\omega t}}{dt} + \frac{dA(t)}{dt} e^{i\omega t} \\
&= i\omega A(t)e^{i\omega t} + \frac{dA(t)}{dt} e^{i\omega t} \\
&= \left(i\omega A(t) + \frac{dA(t)}{dt} \right) e^{i\omega t}
\end{aligned} \tag{2.15}$$

The integral of $V(t)$ can be found using the rule of integration by parts, as $V(t)$ is a product of two functions. Integration by parts states $\int v \frac{du}{dt} dt = uv - \int u \frac{dv}{dt} dt$. In equation 2.14 $A(t)$ is chosen to be v and $e^{i\omega t}$ is $\frac{du}{dt}$, thereby obtaining:

$$\begin{aligned}
\int V(t)dt &= \int A(t)e^{i\omega t}dt \\
&= \frac{A(t)}{i\omega} e^{i\omega t} - \int \frac{dA(t)}{dt} \frac{1}{i\omega} e^{i\omega t} dt
\end{aligned} \tag{2.16}$$

A new integral with the product of two functions is observed. Using integration by parts again on this term using $v = \frac{dA(t)}{dt}$ and $\frac{du}{dt} = \frac{1}{i\omega} e^{i\omega t}$ results in:

$$\begin{aligned}
\int V(t)dt &= \frac{A(t)}{i\omega} e^{i\omega t} + \frac{1}{\omega^2} \frac{dA(t)}{dt} e^{i\omega t} + \int \frac{1}{\omega^2} \frac{d^2 A(t)}{dt^2} e^{i\omega t} dt \\
&= \left(\frac{A(t)}{i\omega} + \frac{1}{\omega^2} \frac{dA(t)}{dt} \right) e^{i\omega t} + \int \frac{1}{\omega^2} \frac{d^2 A(t)}{dt^2} e^{i\omega t} dt
\end{aligned} \tag{2.17}$$

Looking at the last integral term in equation 2.17, two observations are made. Firstly, the expression $\frac{1}{\omega^2}$ becomes a very small number close to 0 for very high frequency systems as this (352.2 MHz). Secondly, the amplitude $A(t)$ is expected to change very little in one RF oscillation, due to the high frequency, therefore the double derivative of the amplitude $\frac{d^2 A(t)}{dt^2}$ will also be very close to 0. This last integral term is therefore neglected as it is considered to be without influence. This therefore results in the integral of $V(t)$ which will further be used for modelling:

$$\int V(t)dt = \left(\frac{A(t)}{i\omega} + \frac{1}{\omega^2} \frac{dA(t)}{dt} \right) e^{i\omega t} \tag{2.18}$$

Substituting equations 2.14, 2.15 and 2.18 into equation 2.13 gives:

$$\begin{aligned}
2I_g(t) - I_b(t) &= \frac{1}{L} \left(\frac{A(t)}{i\omega} + \frac{1}{\omega^2} \frac{dA(t)}{dt} \right) e^{i\omega t} + C \left(i\omega A(t) + \frac{dA(t)}{dt} \right) e^{i\omega t} \\
&\quad + A(t) e^{i\omega t} \left(\frac{1}{R} + \frac{1}{Z} \right)
\end{aligned} \tag{2.19}$$

It was previously assumed that the amplitude $A(t)$ changes very little per RF oscillation, and [12] states that all variables including $I_g(t)$ and $I_b(t)$ is also proportional to $e^{i\omega t}$. By therefore dividing through by $e^{i\omega t}$ results in:

$$\begin{aligned}
2I_g(t) - I_b(t) &= \frac{1}{L} \left(\frac{A(t)}{i\omega} + \frac{1}{\omega^2} \frac{dA(t)}{dt} \right) + C \left(i\omega A(t) + \frac{dA(t)}{dt} \right) \\
&\quad + A(t) \left(\frac{1}{R} + \frac{1}{Z} \right)
\end{aligned} \tag{2.20}$$

Putting $A(t)$ and $\frac{dA(t)}{dt}$ outside parentheses yields:

$$\begin{aligned}
2I_g(t) - I_b(t) &= \frac{A(t)}{Li\omega} \frac{1}{L\omega^2} \frac{dA(t)}{dt} + Ci\omega A(t) + C \frac{dA(t)}{dt} + \frac{A(t)}{R} + \frac{A(t)}{Z} \\
&= \left(\frac{1}{Li\omega} + Ci\omega + \frac{1}{R} + \frac{1}{Z} \right) A(t) + \left(\frac{1}{L\omega^2} + C \right) \frac{dA(t)}{dt} \\
&= \left(-\frac{i}{L\omega} + Ci\omega + \frac{1}{R} + \frac{1}{Z} \right) A(t) + C \left(1 + \frac{1}{\omega^2 LC} \right) \frac{dA(t)}{dt} \\
&= \left(Ci\omega \left(1 - \frac{1}{\omega^2 LC} \right) + \frac{1}{R} + \frac{1}{Z} \right) A(t) + C \left(1 + \frac{1}{\omega^2 LC} \right) \frac{dA(t)}{dt}
\end{aligned} \tag{2.21}$$

The next steps are to express the circuit properties in terms of cavity parameters. The theory of a parallel RLC circuit states that the resonant angular frequency is given by $\omega_0 = \frac{1}{\sqrt{LC}}$ [17]. Thereby the relation $LC = \frac{1}{\omega_0^2}$ exists, such that equation 2.21 becomes:

$$2I_g(t) - I_b(t) = \left(Ci\omega \left(1 - \frac{\omega_0^2}{\omega^2} \right) + \frac{1}{R} + \frac{1}{Z} \right) A(t) + C \left(1 + \frac{1}{\omega^2 LC} \right) \frac{dA(t)}{dt} \tag{2.22}$$

Only the first LC is substituted. The second LC term relates to the derivative of $A(t)$, and this can instead be approximated to $\omega^2 LC \approx 1$ [12]. Inserting this approximation and restructuring gives the following expression:

$$\begin{aligned}
2I_g(t) - I_b(t) &= \left(Ci\omega - \frac{Ci\omega_0^2}{\omega} + \frac{1}{R} + \frac{1}{Z} \right) A(t) + 2C \frac{dA(t)}{dt} \\
&= \left(\frac{Ci\omega^2}{\omega} - \frac{Ci\omega_0^2}{\omega} + \frac{1}{R} + \frac{1}{Z} \right) A(t) + 2C \frac{dA(t)}{dt} \\
&= \left(\frac{Ci(\omega^2 - \omega_0^2)}{\omega} + \frac{1}{R} + \frac{1}{Z} \right) A(t) + 2C \frac{dA(t)}{dt} \\
&= \left(Ci \frac{\omega^2 - \omega_0^2}{\omega} + \frac{1}{R} + \frac{1}{Z} \right) A(t) + 2C \frac{dA(t)}{dt}
\end{aligned} \tag{2.23}$$

Here ω_0 is the resonant angular frequency and ω is the RF frequency. Ideally these should be equal, but are not necessarily the same (however very close), which means detuning can be introduced $\Delta\omega = \omega_0 - \omega$. The term $\omega^2 - \omega_0^2$ becomes:

$$\begin{aligned}
\omega^2 - \omega_0^2 &= \omega^2 - (\omega + \Delta\omega)^2 \\
&= \omega^2 - \omega^2 - 2\omega\Delta\omega - \Delta\omega^2
\end{aligned} \tag{2.24}$$

The difference between ω and ω_0 is expected to be very small, and therefore $\Delta\omega^2$ is a very small number and is neglected:

$$\omega^2 - \omega_0^2 \approx -2\omega\Delta\omega \tag{2.25}$$

Substituting equation 2.25 in equation 2.23 results in:

$$2I_g(t) - I_b(t) = \left(-2i\Delta\omega C + \frac{1}{R} + \frac{1}{Z} \right) A(t) + 2C \frac{dA(t)}{dt} \tag{2.26}$$

The circuit quantities C , R and Z are still left to be expressed in terms of cavity parameters. For a capacitor carrying a charge q , it is known that [18]:

$$C = \frac{q}{|\Delta V|} \tag{2.27}$$

It will not be proven in this thesis, but in [12] it is shown that for a beam travelling through a cavity with a cavity-shape parameter (R/Q) , the capacitance can be expressed as:

$$C = \frac{1}{\omega (R/Q)} \tag{2.28}$$

Similarly, for a parallel resonant circuit a quality factor Q_0 is given as [17]:

$$\begin{aligned}
Q_0 &= \omega CR \\
C &= \frac{Q_0}{\omega R}
\end{aligned} \tag{2.29}$$

By inserting this into 2.28 results in the following equation for resistance:

$$\begin{aligned}\frac{Q_0}{\omega R} &= \frac{1}{\omega (R/Q)} \\ R &= \frac{\frac{Q_0}{\omega}}{\frac{1}{\omega (R/Q)}} \\ R &= Q_0(R/Q)\end{aligned}\tag{2.30}$$

Equivalent for Z which is the impedance of the transmission line, having quality factor Q_{ext} , a relation for Z expressed in cavity quantities is:

$$z = Q_{ext}(R/Q)\tag{2.31}$$

C , R and Z are now expressed in terms of physical cavity parameters in equation 2.28, 2.30 and 2.31 respectively. Substituting these into equation 2.26:

$$\begin{aligned}2I_g(t) - I_b(t) &= \left(-2i\Delta\omega \frac{1}{\omega (R/Q)} + \frac{1}{Q_0(R/Q)} + \frac{1}{Q_{ext}(R/Q)} \right) A(t) + 2\frac{1}{\omega (R/Q)} \frac{dA(t)}{dt} \\ I_g(t) &= \left(-2i\frac{\Delta\omega}{\omega (R/Q)} + \frac{1}{Q_0(R/Q)} + \frac{1}{Q_{ext}(R/Q)} \right) \frac{A(t)}{2} + \frac{1}{\omega (R/Q)} \frac{dA(t)}{dt} + \frac{I_b(t)}{2} \\ I_g(t) &= \left(\frac{1}{Q_0} + \frac{1}{Q_{ext}} - 2i\frac{\Delta\omega}{\omega} \right) \frac{A(t)}{2(R/Q)} + \frac{1}{\omega (R/Q)} \frac{dA(t)}{dt} + \frac{I_b(t)}{2}\end{aligned}$$

As the cavity is coupled to a resonating transmission line, a loaded quality factor can be introduced Q_L : [19]

$$\frac{1}{Q_L} = \frac{1}{Q_0} + \frac{1}{Q_{ext}}\tag{2.32}$$

This relation gives the following expression for $I_g(t)$:

$$I_g(t) = \left(\frac{1}{Q_L} - 2i\frac{\Delta\omega}{\omega} \right) \frac{A(t)}{2(R/Q)} + \frac{1}{\omega (R/Q)} \frac{dA(t)}{dt} + \frac{I_b(t)}{2}\tag{2.33}$$

Multiplying by $\omega(R/Q)$:

$$\left(I_g(t) - \frac{I_b(t)}{2}\right) \omega(R/Q) = \left(\frac{1}{Q_L} - 2i\frac{\Delta\omega}{\omega}\right) \frac{A(t)\omega}{2} + \frac{dA(t)}{dt} \quad (2.34)$$

$$= \left(\frac{\omega}{2Q_L} - i\Delta\omega\right) A(t) + \frac{dA(t)}{dt} \quad (2.35)$$

To achieve the final dynamics of the voltage amplitude, $V(t)$ is substituted for $A(t)$ and the voltage derivative is isolated:

$$\frac{dV(t)}{dt} = -\left(\frac{\omega}{2Q_L} - i\Delta\omega\right) V(t) + \omega(R/Q) \left(I_g(t) - \frac{I_b(t)}{2}\right) \quad (2.36)$$

This is the continuous-time model first order model of the voltage dynamics in an RF accelerating cavity. A particle accelerating RF cavity is usually modelled with I and Q modulation making the system complex (which is why the $\Delta\omega$ is complex). However as this modulation and demodulation happens in the Low Level RF (LLRF) firmware (or directly in the hardware), the control system itself will only deal with the complex envelope of the voltage signal. Therefore for control design the complex detuning can be neglected:

$$\frac{dV(t)}{dt} = -\frac{\omega}{2Q_L} V(t) + \omega(R/Q) \left(I_g(t) - \frac{I_b(t)}{2}\right) \quad (2.37)$$

The input to the cavity is the generator current I_g from a klystron, and the induced current I_b from beam loading. The state of the system is the voltage $V(t)$ in the cavity and the output of the system is the voltage itself. However there is a measurement delay from measuring the voltage output, which will be described in more detail in the following chapter 4. Setting this on state space form will result in:

$$\dot{V}(t) = \mathbf{A}V(t) + \mathbf{B}u(t) \quad (2.38)$$

$$\dot{V}(t) = \left[-\frac{\omega}{2Q_L}\right] V(t) + [\omega(R/Q)] I_g(t) + \left[-\frac{\omega(R/Q)}{2}\right] I_b(t) \quad (2.39)$$

$$Y(t) = V(t) \quad (2.40)$$

DISCRETISATION

The cavity model found above is continuous, however the hardware where the control system needs to be running on is discrete with a sampling time of $T_s = 45.45ns$. The model therefore has to be discretised. This is done using forward Euler numerical approximation [20]:

$$\Phi = [I + AT_s] \quad (2.41)$$

$$\Gamma = [BT_s] \quad (2.42)$$

Here I is the identity matrix with the same dimensions as A . This results in new system matrices, and the complete discrete time state space representation of the voltage in the cavity can be found in the following equation 2.43.

$$V_{n+1} = \left[1 - \frac{\omega T_s}{2Q_L}\right] V_n + \left[\omega(R/Q)\right] i_{g,n} - \left[\frac{\omega(R/Q)}{2}\right] i_{b,n} \quad (2.43)$$

This is a discrete first order state space model, which can be used for control design.

2.2 MODELLING A PARTICLE ACCELERATING RF CAVITY AS A 2ND ORDER SYSTEM

In the previous section a particle accelerating RF cavity was modelled as a first order system by neglecting the second order term in equation 2.17. The LCR circuit presented forming the basis of the model is of 2nd order as it contains two components to store energy, namely both an inductor and a capacitor. An assumption was made that the second order term would have little effect as it is weighted by the inverse squared angular frequency $\frac{1}{\omega^2}$, and the model therefore shifted to 1st order. While this might be perfectly adequate for designing control strategies from a result based engineering perspective, from an academic perspective, it is interesting to investigate how a second order system potentially differs, and if there is gains to be made in the control strategies either in performance, stability or robustness.

This section will therefore derive a 2nd order model by continuing from equation 2.13, but keeping the second order term. The referenced equation is repeated below for convenience.

$$2I_g(t) - I_b(t) = \frac{1}{L} \int V(t)dt + C \frac{dV(t)}{dt} + V(t) \left(\frac{1}{R} + \frac{1}{Z} \right) \quad (2.13 \text{ revisited})$$

Taking the derivative of the entire equation to get rid of the integral yields:

$$2 \frac{dI_g(t)}{dt} - \frac{dI_b(t)}{dt} = \frac{1}{L} V(t) + C \frac{d^2 V(t)}{dt^2} + \frac{dV(t)}{dt} \left(\frac{1}{R} + \frac{1}{Z} \right) \quad (2.44)$$

Restructuring the equation to isolate $\frac{d^2 V(t)}{dt^2}$:

$$\begin{aligned} 2 \frac{dI_g(t)}{dt} - \frac{dI_b(t)}{dt} &= \frac{1}{L} V(t) + C \frac{d^2 V(t)}{dt^2} + \frac{dV(t)}{dt} \left(\frac{1}{R} + \frac{1}{Z} \right) \\ C \frac{d^2 V(t)}{dt^2} &= -\frac{1}{L} V(t) - \frac{dV(t)}{dt} \left(\frac{1}{R} + \frac{1}{Z} \right) + 2 \frac{dI_g(t)}{dt} - \frac{dI_b(t)}{dt} \\ \frac{d^2 V(t)}{dt^2} &= -\frac{1}{LC} V(t) - \frac{dV(t)}{dt} \left(\frac{1}{CR} + \frac{1}{CZ} \right) + \frac{2}{C} \frac{dI_g(t)}{dt} - \frac{1}{C} \frac{dI_b(t)}{dt} \end{aligned} \quad (2.45)$$

From equation 2.45 a state space model can be formed. Setting states to be $x_1 = V(t)$ and $x_2 = \frac{dV(t)}{dt}$, input u to be $u = \frac{dI_g(t)}{dt}$ and disturbance $d = \frac{dI_b(t)}{dt}$. Thereby state vector X and input vector U can be formed:

$$X = \begin{bmatrix} x_1 \\ x_2 \end{bmatrix} \quad (2.46)$$

$$U = \begin{bmatrix} u \\ d \end{bmatrix} \quad (2.47)$$

State space model can now be retrieved from these equations:

$$\begin{aligned} \frac{dx_1}{dt} &= x_2 \\ \frac{dx_2}{dt} &= -\left(\frac{1}{LC} \right) x_1 - \left(\frac{1}{CR} + \frac{1}{CZ} \right) x_2 + \left(\frac{2}{C} \right) u - \left(\frac{1}{C} \right) d \end{aligned}$$

Putting these equations on matrix form yields:

$$\dot{X} = \begin{bmatrix} 0 & 1 \\ -\frac{1}{LC} & -\left(\frac{1}{CR} + \frac{1}{CZ} \right) \end{bmatrix} \begin{bmatrix} x_1 \\ x_2 \end{bmatrix} + \begin{bmatrix} \frac{2}{C} & 0 \\ 0 & -\frac{1}{C} \end{bmatrix} \begin{bmatrix} u \\ d \end{bmatrix} \quad (2.48)$$

Just like in the first order case, the electrical circuit parameters need to be replaced with cavity parameters. In resonant parallel circuits, there exists a relation $\omega_0 = \frac{1}{\sqrt{LC}}$, and therefore: [17]

$$LC = \frac{1}{\omega_0^2}$$

Using this relation will therefore transform equation 2.48 into:

$$\dot{X} = \begin{bmatrix} 0 & 1 \\ -\omega_0^2 & -\left(\frac{1}{C R} + \frac{1}{C Z}\right) \end{bmatrix} \begin{bmatrix} x_1 \\ x_2 \end{bmatrix} + \begin{bmatrix} \frac{2}{C} & 0 \\ 0 & -\frac{1}{C} \end{bmatrix} \begin{bmatrix} u \\ d \end{bmatrix} \quad (2.49)$$

In the section deriving the first order model, expressions for C , R and Z was derived to be:

$$C = \frac{1}{\omega(R/Q)} \quad (2.28 \text{ revisited})$$

$$R = Q_0(R/Q) \quad (2.30 \text{ revisited})$$

$$z = Q_{ext}(R/Q) \quad (2.31 \text{ revisited})$$

Inserting these expressions in the model will result in:

$$\dot{X} = \begin{bmatrix} 0 & 1 \\ -\omega_0^2 & -\left(\frac{1}{\frac{Q_0(R/Q)}{\omega(R/Q)}} + \frac{1}{\frac{Q_{ext}(R/Q)}{\omega(R/Q)}}\right) \end{bmatrix} \begin{bmatrix} x_1 \\ x_2 \end{bmatrix} + \begin{bmatrix} 2\omega(R/Q) & 0 \\ 0 & -\omega(R/Q) \end{bmatrix} \begin{bmatrix} u \\ d \end{bmatrix} \quad (2.50)$$

$$\dot{X} = \begin{bmatrix} 0 & 1 \\ -\omega_0^2 & -\left(\frac{\omega(R/Q)}{Q_0(R/Q)} + \frac{\omega(R/Q)}{Q_{ext}(R/Q)}\right) \end{bmatrix} \begin{bmatrix} x_1 \\ x_2 \end{bmatrix} + \begin{bmatrix} 2\omega(R/Q) & 0 \\ 0 & -\omega(R/Q) \end{bmatrix} \begin{bmatrix} u \\ d \end{bmatrix} \quad (2.51)$$

$$\dot{X} = \begin{bmatrix} 0 & 1 \\ -\omega_0^2 & -\omega\left(\frac{1}{Q_0} + \frac{1}{Q_{ext}}\right) \end{bmatrix} \begin{bmatrix} x_1 \\ x_2 \end{bmatrix} + \begin{bmatrix} 2\omega(R/Q) & 0 \\ 0 & -\omega(R/Q) \end{bmatrix} \begin{bmatrix} u \\ d \end{bmatrix} \quad (2.52)$$

The loaded quality factor Q_l can be introduced as:

$$\frac{1}{Q_l} = \frac{1}{Q_0} + \frac{1}{Q_{ext}}$$

Therefore the final 2nd order continuous state space model is presented in the following equations 2.53 and 2.54:

$$\dot{X} = \begin{bmatrix} 0 & 1 \\ -\omega_0^2 & -\frac{\omega}{Q_L} \end{bmatrix} \begin{bmatrix} x_1 \\ x_2 \end{bmatrix} + \begin{bmatrix} 2\omega(R/Q) & 0 \\ 0 & -\omega(R/Q) \end{bmatrix} \begin{bmatrix} u \\ d \end{bmatrix} \quad (2.53)$$

$$Y = \begin{bmatrix} 1 & 0 \end{bmatrix} \begin{bmatrix} x_1 \\ x_2 \end{bmatrix} \quad (2.54)$$

DISCRETISATION

Forward Euler was the chosen discretisation method for the first order system, and the principle can be seen in equation 2.55. However the 2nd order model becomes unstable using Forward Euler to discretise it, due to the very fast sample time.

$$X_{n+1} = [I + AT]X_n \quad (2.55)$$

$$\Gamma = [BT] \quad (2.56)$$

Using a bilinear transform (also known as Tustins method) guarentees discrete time stability if the continuous time model is stable. The bilinear transform maps the left half plane of the complex s-plane into the unit circle in the z-plane, and thereby preserving stability. The bilinear transform is a first order approximation and can be characterised by the following equations [21]:

$$z = e^{sT} \quad (2.57)$$

$$z \approx \frac{1 + \frac{T}{2}s}{1 - \frac{T}{2}s} \quad (2.58)$$

This report will not go into further details with the bilinear transformation, as it is outside the scope of the project. Matlabs *c2d* command will be used to convert the continuous time model presented in equations 2.53 and 2.54 into a discrete time system.

2.3 NOISE ANALYSIS IN VOLTAGE MEASUREMENT

This section will investigate the noise content in the voltage signal in the LINAC4 cavities with the purpose of evaluating if the noise signal need to be modelled and accounted for in future control design. A section of the steady state signal of the CCDTL7 cavity was recorded with a total sample size of 4000 and can be seen in figure 2.3.

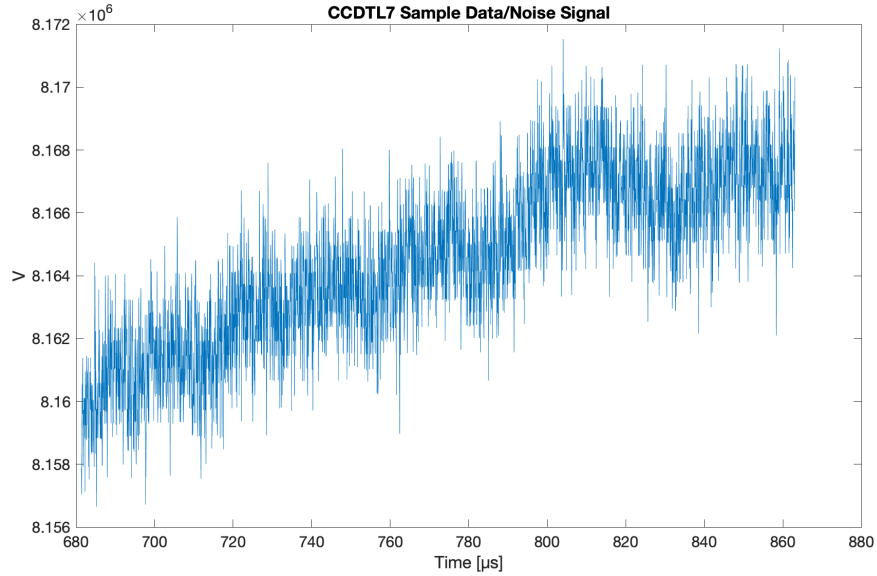


Figure 2.3: Voltage measurement of the CCDTL7 cavity in steady state. Sample size is $N=4000$.

It can be seen there is an upwards trend in the data due to the cavity being in open loop. The noise signal can be detrended without losing it's characteristics by using linear regression to achieve a model of the trend and subtract that from the noise signal. The detrended data compared to the sample data with subtracted mean can be seen in figure 2.4.

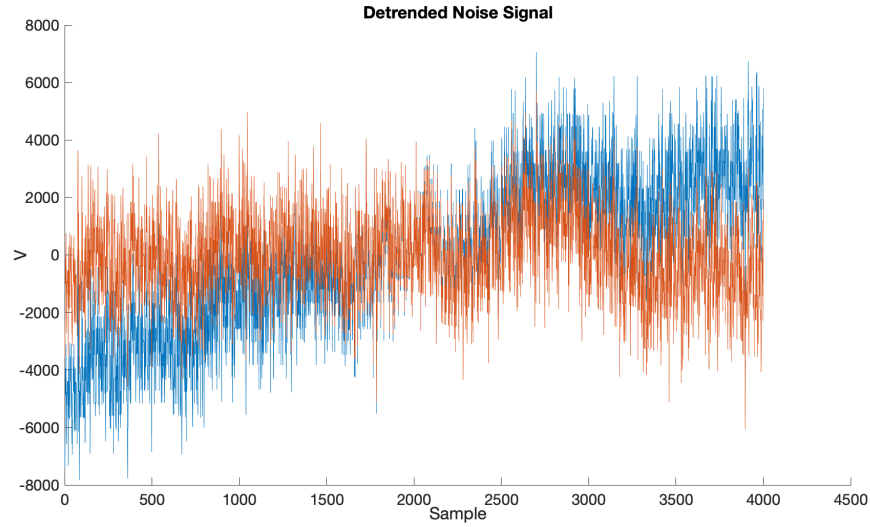


Figure 2.4: Detrended noise signal (orange) of the CCCTL7 cavity in steady state.

From the data it is hard to characterise the type of noise and its characteristics. To further investigate the type of noise signal, it is relevant to look at periodicity in the data. White noise has a special characteristic, that it should be completely random, meaning equal intensity over all frequencies and no correlation with lag-versions of it self. To investigate if the noise signal in the CCCTL7 cavity can be assumed white noise, the autocorrelation function of the sample signal can be obtained.

The auto correlation of the above signal, which can be seen in the following figure 2.5, indicates that it is not pure white noise. There is periodic behaviour in the data. For it to be white noise, it needs to only be correlated with it self, which the autocorrelation function in this case shows it clearly is not.

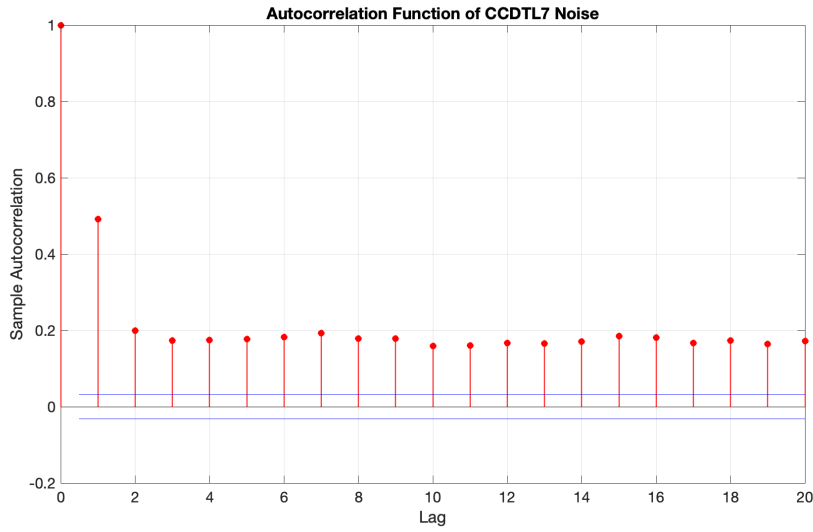


Figure 2.5: Auto correlation of the noise signal from a Voltage measurement of the CCDTL7 cavity.

That the noise signal is not white noise, might be due to analog to digital converters, amplifiers, klystrons and digital to analog converters all being in the loop. Looking at two other cavities namely CCDTL56 and PIMS0102, similar signals can be seen in figures 2.6 and 2.8, and their corresponding autocorrelations in figure 2.7 and 2.9. It can be seen that the noise characteristics displayed in the autocorrelation functions are quite different from all three cavities. None of the three cavities noise signal can be categorised as white noise. However looking at the raw noise signals they all vary between $-6000V$ to $+6000V$. The magnitude of the voltage variation in all three noise samples can therefore be concluded to be negligible compared to the magnitude of the cavity voltage. The noise will therefore not be modelled and included in future simulation environments.

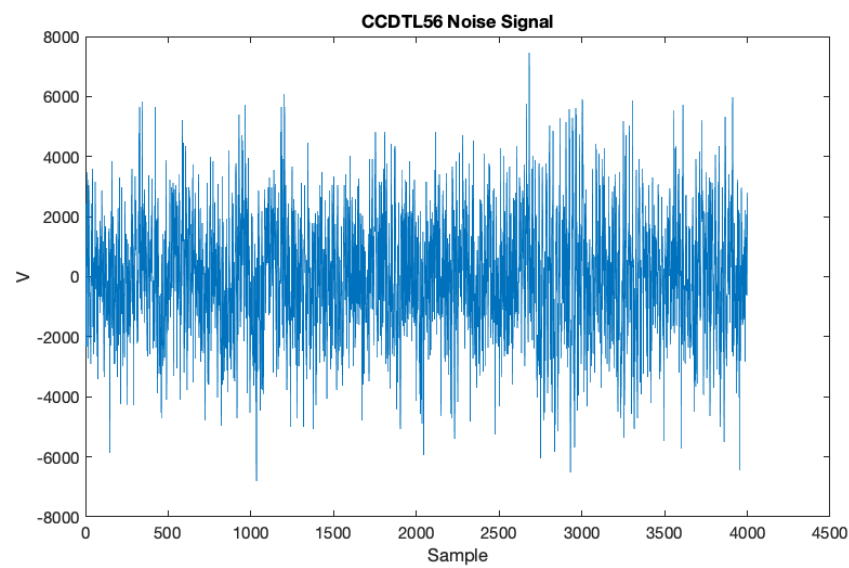


Figure 2.6: Noise signal of the CCDTL56 cavity with sample size of 4000.

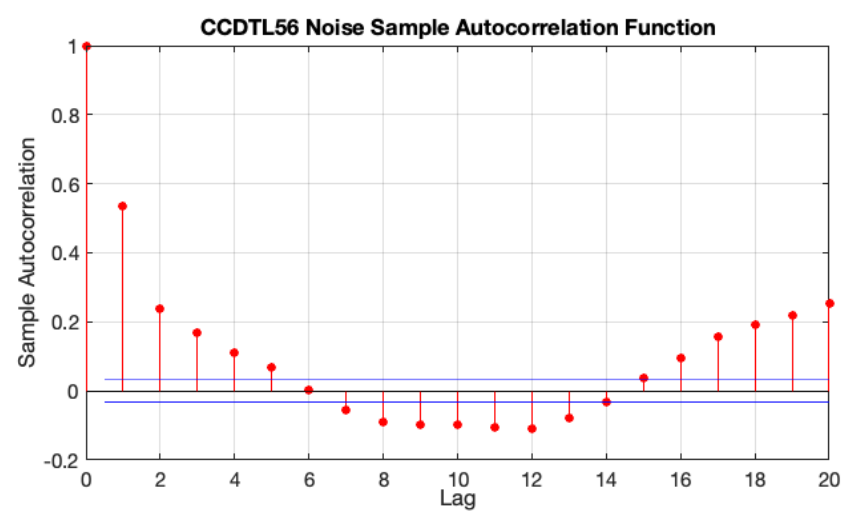


Figure 2.7: Auto correlation of the noise signal from a Voltage measurement of the CCDTL56 cavity.

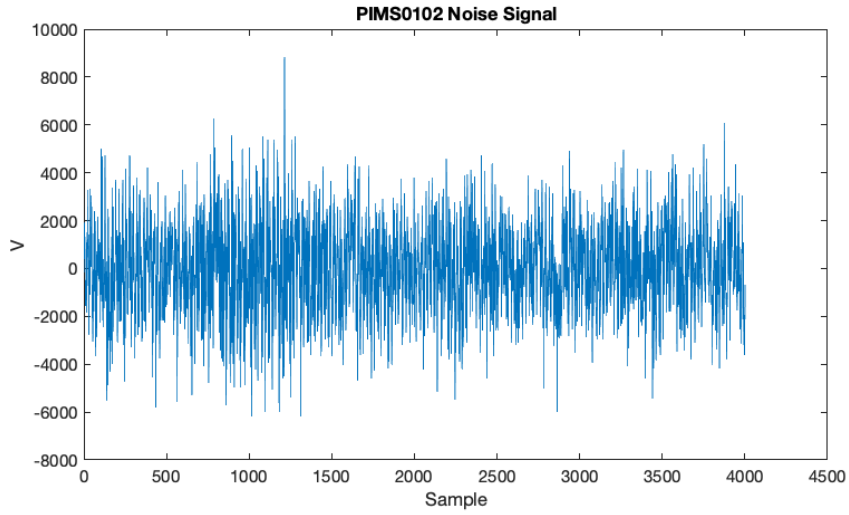


Figure 2.8: Noise signal of the PIMS0102 cavity with sample size of 4000.

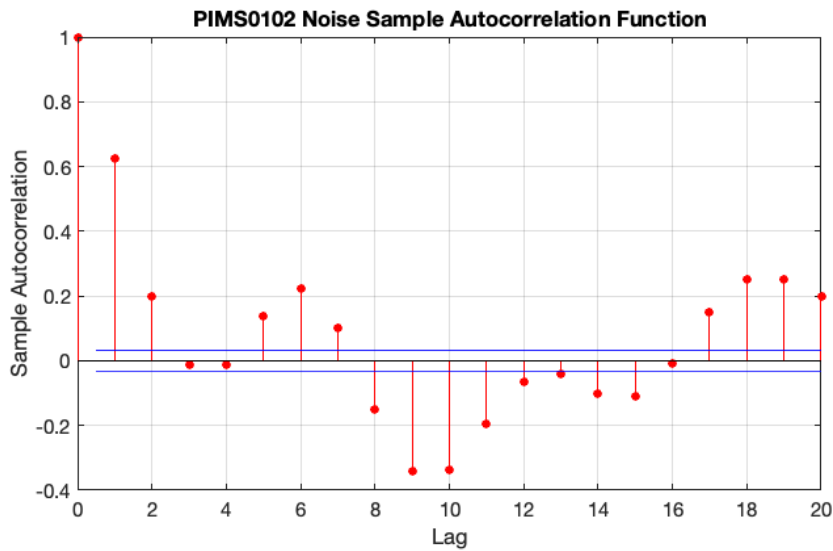


Figure 2.9: Auto correlation of the noise signal from a Voltage measurement of the PIMS0102 cavity.

2.4 MODEL VERIFICATION

The models derived in previous sections need verification before control strategies can be designed. The purpose of model verification is to confirm that a model emulates the behaviour of a real system, which makes it possible to test different control strategies in a simulation environment without the risk of breaking or damaging any hardware or possibly injuring people.

An open loop response of the real CCDTL7 cavity in LINAC 4 has been obtained with a reference of $8.1 \cdot 10^6 V$ including beam entering the cavity around $300\mu s$. In order to not trip the RF amplifiers on the cavity, the drive power (and thereby the voltage) is ramped to the setpoint in $25\mu s$. A small environment was set up in simulink to test the open loop response of the model with the same parameters as the CCDTL7 cavity. A 29 time step delay is added to the output to match the delay in the real cavity. When the beam enters the CCDTL7 cavity, a voltage drop of 10% is observed. A step of $-8.1 \cdot 10^5$ is added as process noise to the input of the model to mimic beam loading in the real cavity. The simulink setup can be seen in figure 2.10.

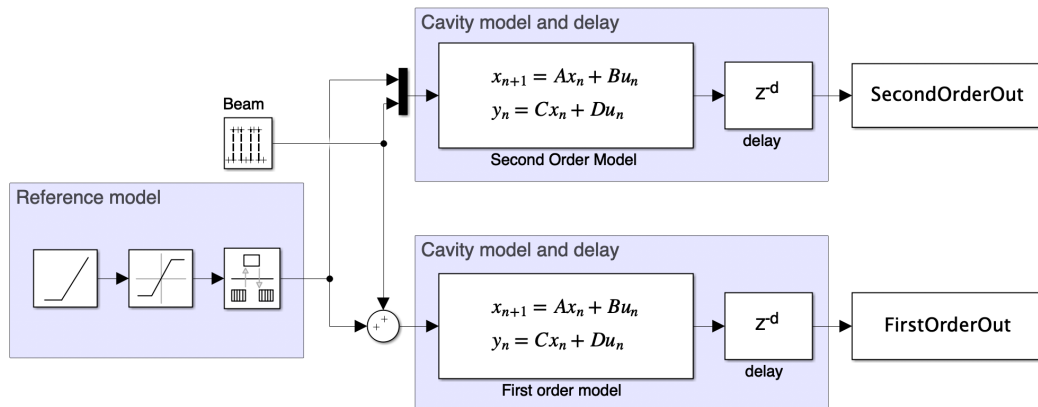


Figure 2.10: Simulink environment for getting open loop model responses with beam loading included.

Using the same model parameters for $Q_l = 15754.44$ and $R/Q = 1195.99$ for both the first order model and the second order model, responses were obtained, and can be seen compared to the open loop data response of the CCDTL7 model in the following figure 2.11

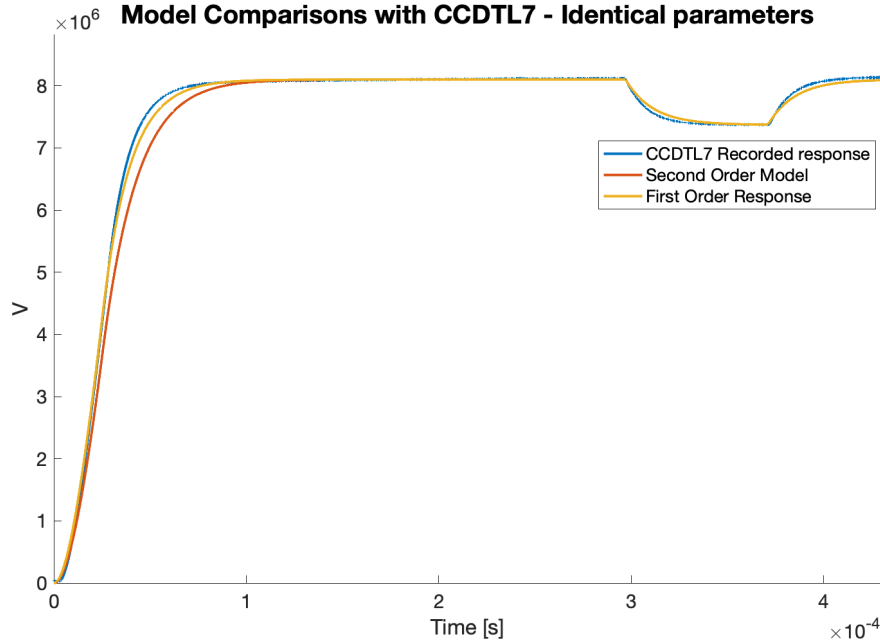


Figure 2.11: Model responses compared to CCDTL7 cavity open loop response with beam loading. The first and second order models use the same parameters.

As can be seen the models follows the behaviour of the real cavity both while ramping up, and during beam loading. There is however variations from model to cavity which can be due to model parameters not being estimated perfectly. In the comparison in figure 2.11 it is assumed that the parameters provided by CERN is valid for both a first order and second order model. As a cavity is a system of second order, it is expected that the second order model should be following the recorded cavity response closer than the first order model. If instead of using the same parameters as the first order model, the Q_l and R/Q parameters can be estimated given the data from the open loop response of the cavity. This is done using Matlabs *greyest* function which estimates Q_l and R/Q using the method of least squares. The new estimated parameters are then:

$$Q_l = 11400$$

$$R/Q = 5703$$

Using these new parameters in the second order model, the responses can again be compared. A full cycle can be seen in figure 2.12.

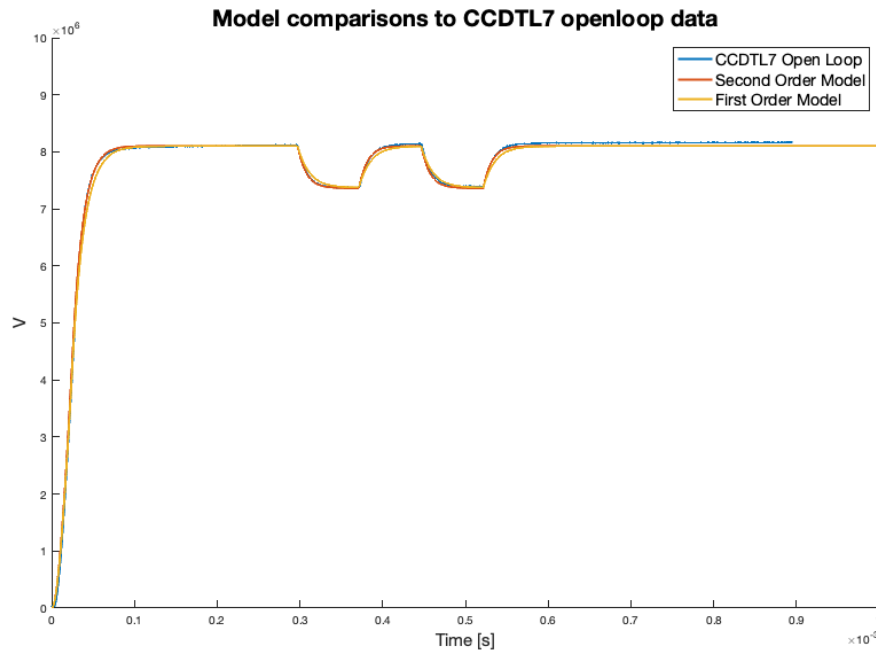


Figure 2.12: Model responses compared to CCDTL7 cavity open loop response with beam loading. The first and second order models use different model parameters.

Zooming in on the transient response can be seen in figure 2.13, showing a much close fit to the recorded data. It can be seen that the second order model follows the recorded data almost perfectly during the ramp up and transient. The first order model also behaves very similar to the behaviour of the real cavity.

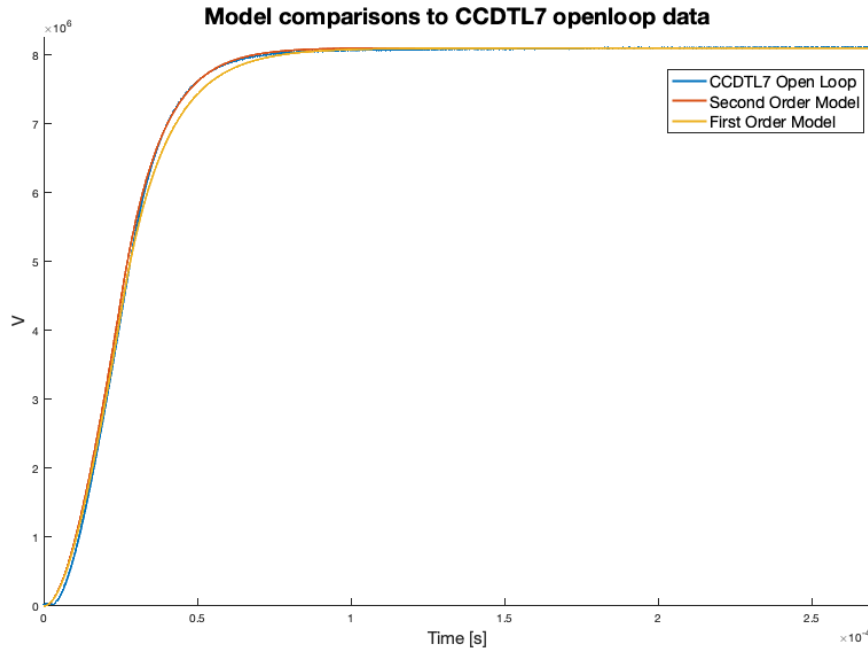


Figure 2.13: Transient model responses compared to CCDTL7 cavity open loop response. The first and second order models use different model parameters.

The big difference between the first order and second order model is during beam loading as can be seen in figure 2.14. The second order model follows the exact behaviour of the cavity whereas the first order model also follows the behaviour of the cavity but with some variations.

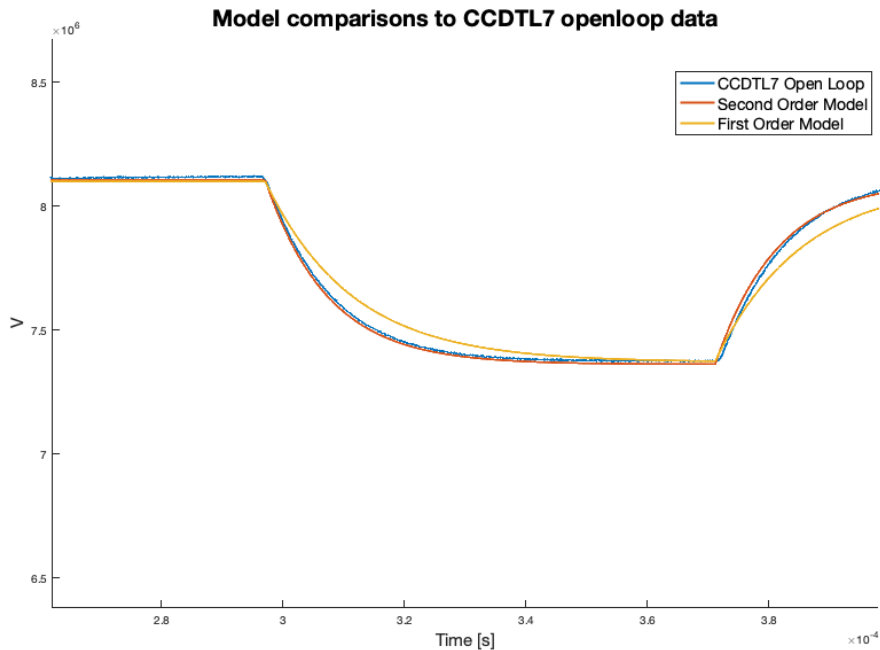


Figure 2.14: Model responses compared to CCDTL7 cavity open loop response during beam loading. The first and second order models use different model parameters.

It is clear that the second order model with grey box estimated cavity parameters describes the cavity more closely than the first order model. Root Mean Squared Errors of the models compared to the open loop data are presented in table 2.1. During the transient response, the second order model deviates 8.2% less from the reference cavity response than the first order model. The same tendency applies during beam loading where the second order model deviates 71.60% less than the first order model. Both models are however deemed to fit well enough to the actual cavity, and will both be used in the following chapters to design and test control strategies.

Table 2.1: Deviations measured by the Root Mean Squared Error (RMSE) comparing the two derived models to output data from a cavity. Only the same section of the response can be compared between the models, and therefore a separating horizontal line is added.

Model	Section of response	RMSE	RMSE visualised
1st	Transient	71226 V	<div></div>
2nd	Transient	65358 V	<div></div>
1st	Beam loading	267.5 V	<div></div>
2nd	Beam loading	76.96 V	<div></div>

SUMMARY OF INTERNSHIP PROJECT

A previous project for CERN investigated by the author of this thesis was to find ways to improve the cavity control systems running on the LINAC4 particle accelerator in terms of reducing computational complexity. This resulted in a report titled “Cavity Control Loop Optimisation For CERNs LINAC4 Linear Particle Accelerator” [1]. This chapter will summarise the motivation, methods and findings of that project, as some of the control design in this thesis builds on experiences from the previous project.

3.1 CAVITY CONTROL LOOP OPTIMISATION

The motivation for the project was to investigate if the computational complexity of the cavity control loops could be reduced without losing performance of the regulators. As all the control loop computations have to be completed within a strict deadline of $45.3ns$, large regulator matrices and multiplications caused some of the cavities control loops to fail timing tests. The author proposed to design a regulator based only on the estimate of the voltage in the cavity at that specific time instance, instead of regulating based on all delayed states. This would reduce the controller dimensions from $[1 \times N + 1]$, where N is the size of the delay in terms of time steps, to a single dimension, and thereby reducing the number of mathematical operations needed per iteration drastically.

This project modelled the cavity as a first order system, just as shown in this thesis, section 2.1. The discretised model is repeated here for convenience:

$$V_{n+1} = \left[1 - \frac{\omega T_s}{2Q_L}\right] V_n + \left[\omega(R/Q)\right] i_{g,n} - \left[\frac{\omega(R/Q)}{2}\right] i_{b,n} \quad (2.43 \text{ revisited})$$

Based on this model, a Kalman estimator was designed to predict the voltage in the cavity at the current time step based on N -delayed voltage measurement. This was done by expanding the system matrices by N -dimensions. The method of doing this will be explained in section 4.1 where a Kalman estimator is designed based on the derived second order model to estimate \hat{V}_n based on V_{n-N} measurements.

The output of the Kalman estimator would be the estimated states going from the current time instance to the N -delayed time instance.

Two different sets of LQR controllers were designed. One designed based only the most recent estimate of the voltage in the cavity, and the other designed using all the estimated states. The controllers were tuned with the same Q and R weights, and the outputs were tested and compared, both in simulation and on different real LINAC4 cavities, which the following sections will explain.

3.2 COMPARISON OF FULL STATE AND SINGLE STATE FEEDBACK IN SIMULATION

Simulink was used as the simulation environment for testing and comparing the single and full state regulators. The simulink setup can be seen in figure 3.1. The reference model was designed based on a ramp and an upper limit block. This was to reproduce the input drive to the real cavity, where the drive is ramped to reference in $25\mu s$. Next was a discrete time integrator before the integral gain, together adding integral action to prevent steady state errors. The derived 1st order state space model, Kalman estimator and LQR state feedback gain were implemented using prebuilt Simulink blocks taking in the system matrices as inputs. Worth noting is the beam was added as process noise using a pulse with a magnitude corresponding to 10% of the reference voltage, and white noise was added after a N time step delay to simulate measurement noise. The output of the plant (cavity voltage) was saved to the MATLAB workspace, for later evaluation. The entire simulation was running with a $45.3ns$ sample time and based on the CCCTL7 cavity in LINAC4.

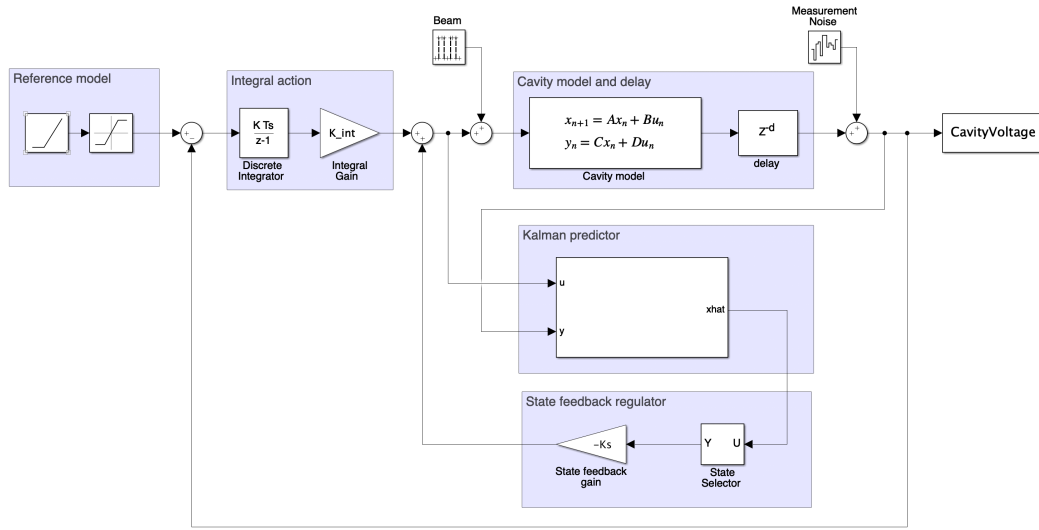


Figure 3.1: Simulation environment in Simulink of a single cavity loop based on a first order model.

This model was used to test both a full state feedback controller and a single state feedback controller. As shown in figure 3.1, a state selector was added just before the state feedback gain to only chose the first estimated state. If the state selector block is taken out, it becomes a full state feedback regulator and would require a state feedback vector as the gain.

RESULTS

The single state feedback controller was simulated selecting only the first state of the Kalman filter \hat{V}_n , and multiplying with the state feedback gain K_s . The full state feedback used all the estimated states $[\hat{V}_n, \hat{V}_{n-1}, \dots, \hat{V}_{n-N}]$ and the state feedback was a $N + 1 \times 1$ vector.

The purpose of the simulation was to check if performance was lost switching from a full state feedback to a single state feedback controller. This was compared by both visual inspection and average standard deviation from reference.

In simulation it was possible to achieve a very similar response from the single state regulator compared to the full state feedback regulator. The responses can be seen in figure 3.2 showing the full response including the ramping up and the beam loading at around $300\mu s$ to $400\mu s$. A closer look at the response to beam loading can be seen in figure 3.3.

In both figures the responses are very similar, and can almost not be distinguished, however the single state feedback had a slight edge when looking at the standard deviation.

During beam loading, the full state feedback deviated around 1% more from the reference than the single state regulator. This was however a very small difference, and it was therefore not concluded that the single state feedback strictly performed better. This was to be tested on real cavities before any conclusions could be drawn.

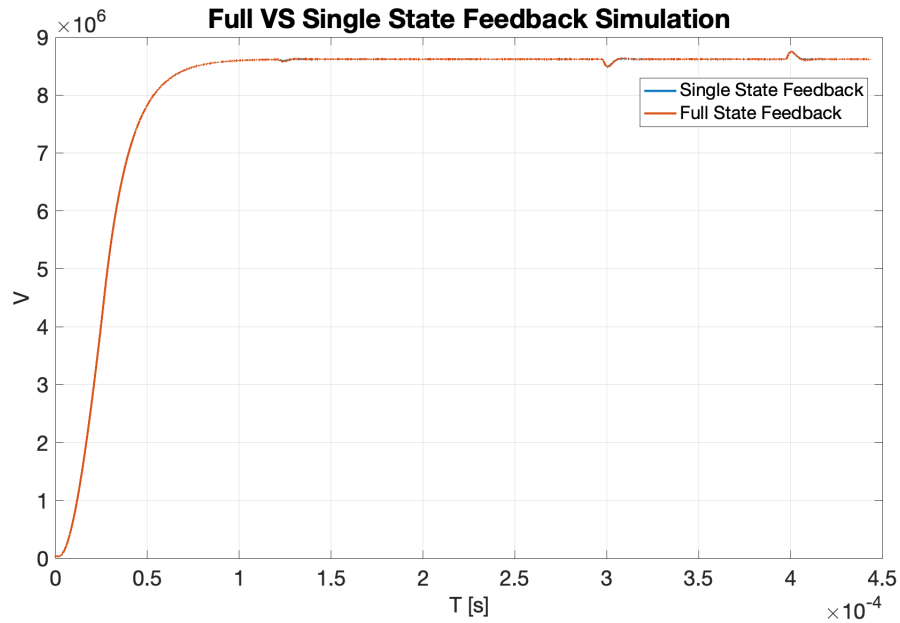


Figure 3.2: Simulation of full state feedback compared to single state feedback. Almost identical performance for the full response including ramp-up and beam loading.

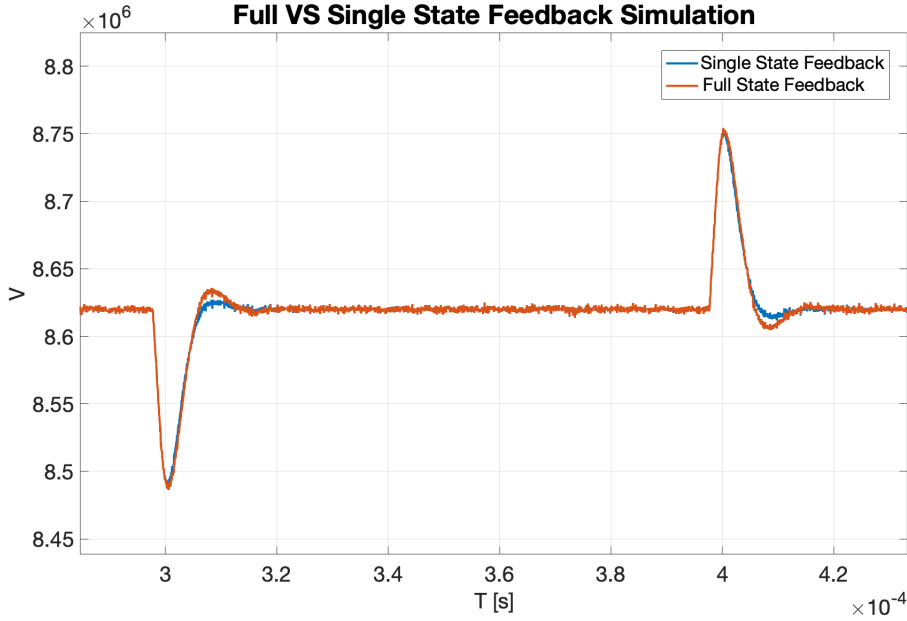


Figure 3.3: Zoomed in on beam loading. It can be seen response is very similar between the full state and single state feedback.

3.3 LINAC4 CAVITY TESTING

Both sets of regulators were implemented on multiple cavities in LINAC4, using the python control toolbox, explained in chapter B.1, to calculate the LQ and Kalman gains. Two types of cavities was used for testing. The first one was a Pi-mode structure cavity (PIMS0304) and the second was a Cell-Coupled Drift Tube Linac (CCDTL0506). They are designed for acceleration at different energy levels, but both modelled as a first order system as explained in the modelling chapter 2, and the difference will therefore not be explained further in this report.

PIMS0304 CAVITIES

Testing the full state feedback on the PIMS0304 cavity, resulted in a response as shown in the following figure 3.4. This was used as the benchmark behaviour, to compare the single state feedback regulator against.

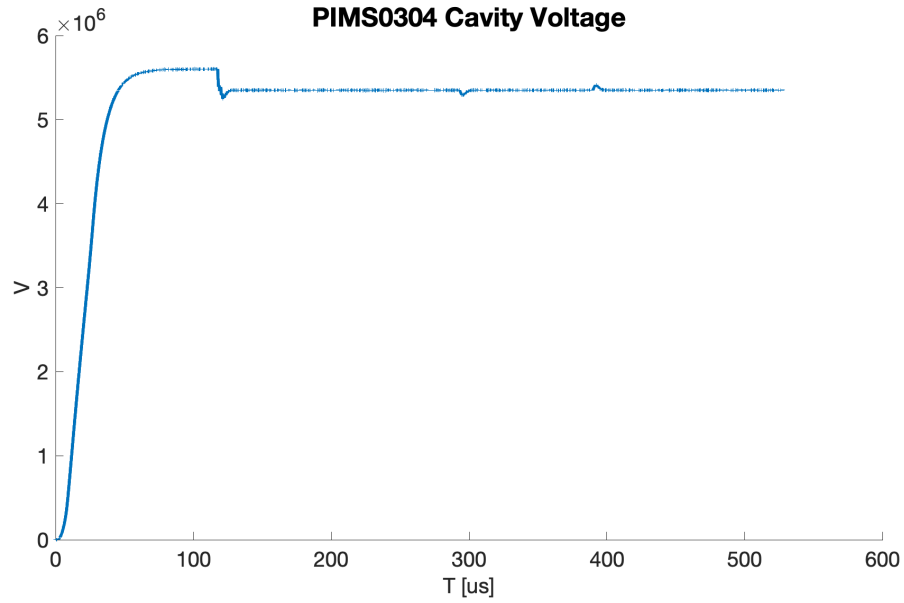


Figure 3.4: Full response data including transient (feedback on), and beam loading.

Two different tunes of the single state feedback was tested - an aggressive and a non aggressive tune. Below are presented two figures showing different LQR tunes on the same cavity. In Fig. 3.5 of transient responses, two examples of a single state feedback is shown together with a full state feedback. By adjusting the Q and R parameters, the single state feedback can be tuned to give both a response with more and less overshoot than the full state regulator. In this figure one of the single state feedback regulations achieves to settle faster than the full state feedback, with no overshoot and significantly less undershoot.

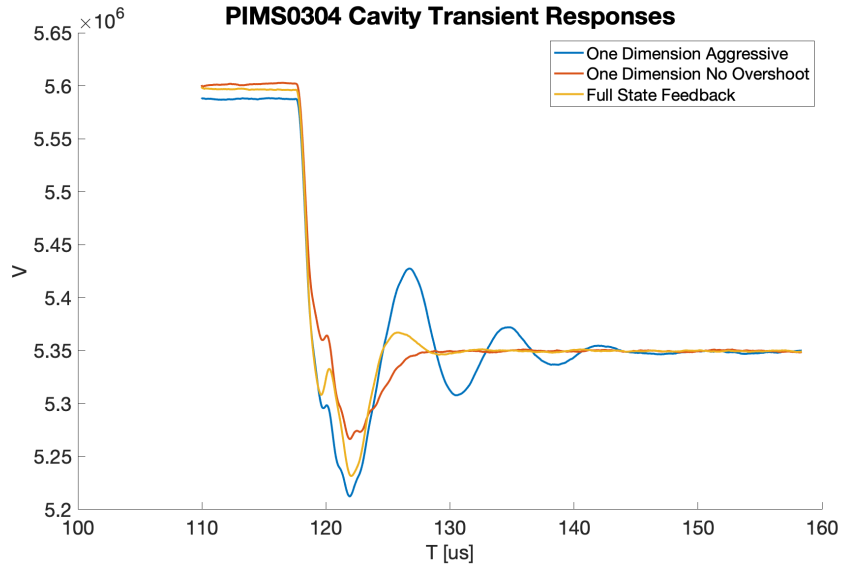


Figure 3.5: Transient responses of full state and single state feedback schemes in LINAC4 RF cavity PIMS0304.

The same behaviour can be seen in Fig. 3.6 showing the different controllers response to beam loading. No performance seem to have been lost from the single state feedback, although the full state response seem to have if not the same settling time then a little better. This data has been smoothed by a centred moving average filter for easier comparison of the responses as the signal was quite noisy.

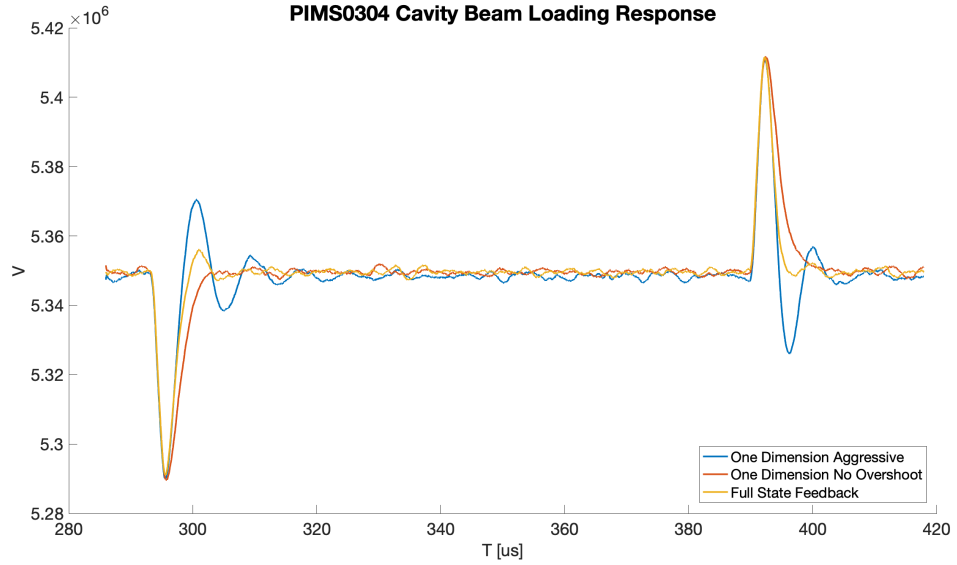


Figure 3.6: Responses to beam loading in LINAC4 RF cavity PIMS0304.

The performance was evaluated closer by the average standard deviation from the reference of $5.4 \cdot 10^6 \text{V}$. It was calculated and can be seen visualised in figure 3.7. It can be seen for the PIMS0304 cavity the non aggressive single state feedback controller performed slightly worse than the full state feedback. However the difference is very small. Being that the difference was that small, it seemed as though no crucial performance were lost switching to the single state feedback.

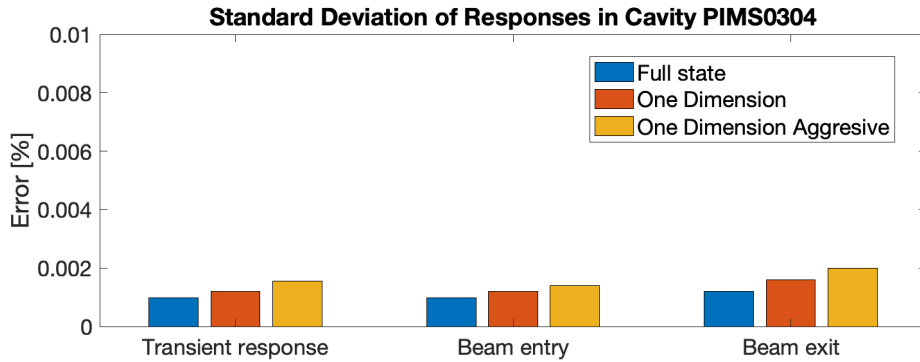


Figure 3.7: Standard deviation of the three responses RF cavity PIMS0304.

CCDTL0506 CAVITIES

Testing on cavity CCDTL0506 in LINAC4 as well showed similar behaviour. In Fig. 3.8 it can be seen, that on the transient response the single state feedback

regulator was superior to the full state regulator. There is a significant difference in overshoot and settling time. Comparing the beam loading responses, it was found to be comparable to the case of the PIMS0304 cavity.

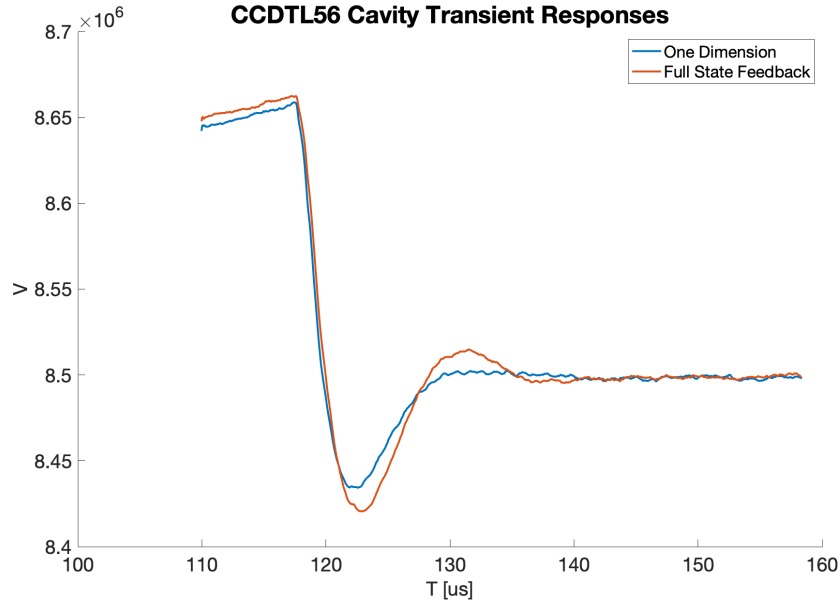


Figure 3.8: Transient responses of full state and single state feedback schemes in LINAC4 RF cavity CCDTL56.

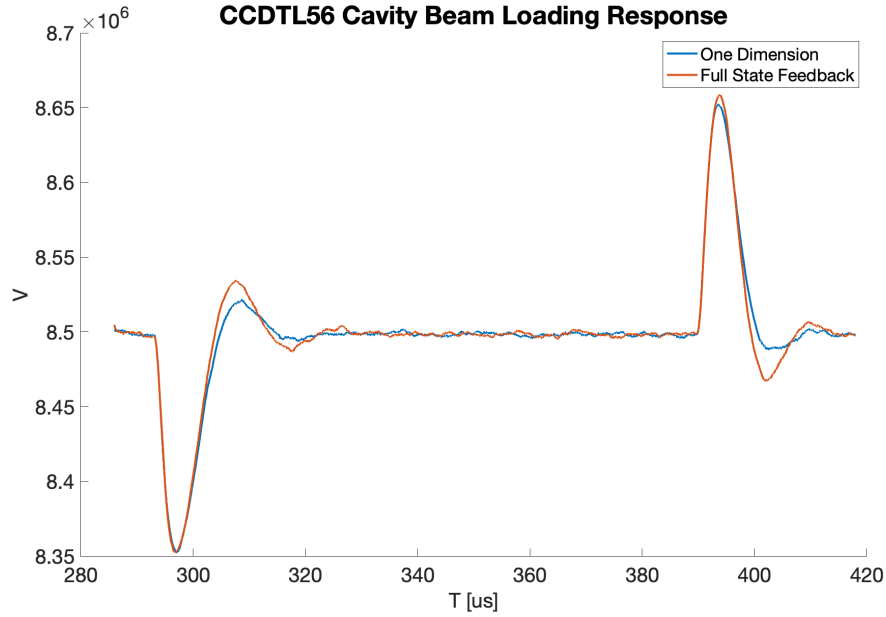


Figure 3.9: Responses to beam loading in LINAC4 RF cavity CCDTL56.

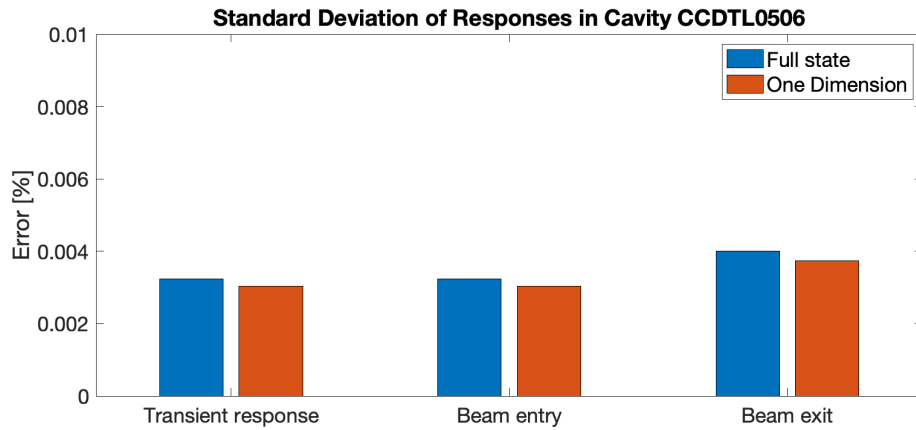


Figure 3.10: Standard deviation of the three responses RF cavity CCDTL0506.

Looking at the standard deviation in figure 3.10 from the reference of $8.5 \cdot 10^6 V$, it can be seen that the single state regulator performed slightly better than the full state regulator, with generally less deviation from the reference.

Based on these tests, it was concluded that there were no significant loss in performance going from full state to single state regulation. In some cases the single state had a more desirable response with less overshoot and faster settling time. This was therefore concluded to be a viable option to eliminate extensive matrix

multiplications and thereby passing the timing tests. Building upon this experience means that all control design in this thesis, will first and foremost be based on the second order model, and will not be designed using a full state feedback, but merely designed on the most recent estimates. This will be further explained in the following control design chapter 4.

CONTROL DESIGN

In chapter 2 both a first and second order model of an RF accelerating cavity was derived, and an open loop response was presented of both the model and recorded data from a cavity in LINAC4. The concept of beam loading was introduced: when charged particles enter the cavity, they absorb some of the energy stored in the cavity in order to accelerate. This results in the voltage in the cavity dropping while particles are accelerated through. This directly translates to the particles in a bunch being accelerated unevenly, as the fastest particles arrive when the voltage has not yet dropped and they therefore absorb the most energy. The slower particles in the same bunch that enters the cavity later, sees a smaller voltage, and therefore absorbs less energy causing a smaller acceleration. This chapter will focus on designing control systems to regulate the RF power to the cavity to minimise the effect of beam loading. The first order model presented in the previous chapter was purely derived to show what is generally used to design control systems for RF accelerating cavities, and will not be used for control design in the remainder of this thesis. Chapter 3 presented a use case and results of control systems designed around the first order model based on a previous project. All control design in this chapter will therefore be based on the grey box derived and verified second order model. First section 4.1 will design a Kalman observer to handle a measurement delay, section 4.2 will verify the designed Kalman estimator before section 4.3 will design an LQR regulator based on the Kalman estimated voltage.

All theory presented in this chapter is based on [22], [23] and [24].

4.1 KALMAN ESTIMATION OF VOLTAGE IN LINAC4 RF CAVITY

The second order model derived in equations 2.53 and 2.53 describes the cavity voltage over time. The voltage in the cavity can be measured at several different points in the cavity. However, these measurements are delayed with timestep N , and only the voltage V_{n-N} can be measured. In figure 4.1 a section of the LINAC4 is illustrated. The RF accelerating cavities sits in a tunnel below the ground while the electronics, computers and crates running the control systems sits above ground.

When dealing with particle acceleration, it is crucial to have a very fast reacting control system. The cavities run at 352.2MHz and the control system has a sample rate of 45ns . Since the wires connected to the voltage antennas are spanned out over some distance from the cavities under ground to the control computers above ground, they introduce fixed delays depending on the cable lengths. LINAC4 is 86 meters long, and is located 12 meters below the ground surface. All the Klystrons supplying the RF power to the cavities and the control computers are located in the same building, and therefore depending on the cavity and its location in the LINAC4 structure, the delay is different for each cavity as the length of the wires varies.

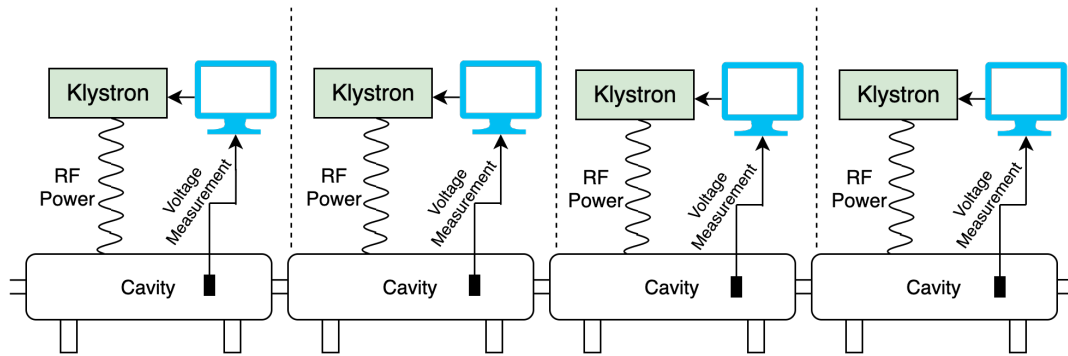


Figure 4.1: Illustration of a section of the LINAC4 accelerator and how the voltage measurements and control systems are connected to the RF power generator. Due to the very fast sample rate needed for the control system, 45 ns , the wire length from the voltage antenna in the cavity under ground, to the computers running the control systems above ground causes an N -timestep delay.

Due to the fast sample time, the delays can potentially be a large number of time steps. Therefore designing a fast control system based on very old measurements can mean, that the regulator can make the system unstable as it is regulating blindly. Figure 4.2 illustrates what effect a large time delay could have. When the beam enters and starts loading the cavity the voltage sensor picks up a dropping voltage (green alert on the figure). Due to the wire length and thereby the large delay, when the computer picks up the voltage starting to drop (red alert on the figure), the particle bunch will already have travelled a certain distance through the cavity, and the voltage will have dropped as shown. This is a very extreme case, and merely used to illustrate what a measurement delay in the system can mean.

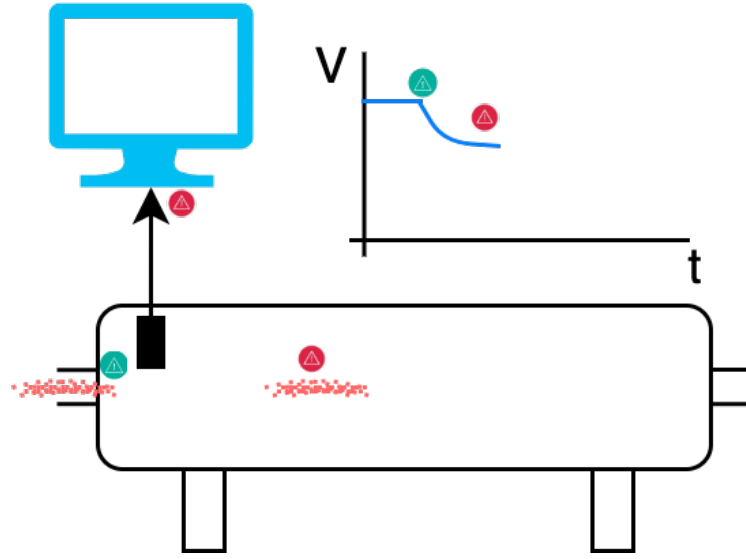


Figure 4.2: Illustration showing what effect an unhandled delay can have. When the particles enter the cavity at the green alert, the voltage sensor picks up that the voltage starts to drop. The red alert is the time instance when the control system computers receives the delayed voltage measurements and detects the beam loading, showing particles having travelled a distance through the cavity and a voltage drop.

Since the system is linear, a Kalman filter can be used in a Smith predictor configuration to estimate the voltage V_n given a V_{n-N} measurement. Simplified the system can be illustrated as in figure 4.3 where the output of the Kalman estimator is \hat{V}_n .

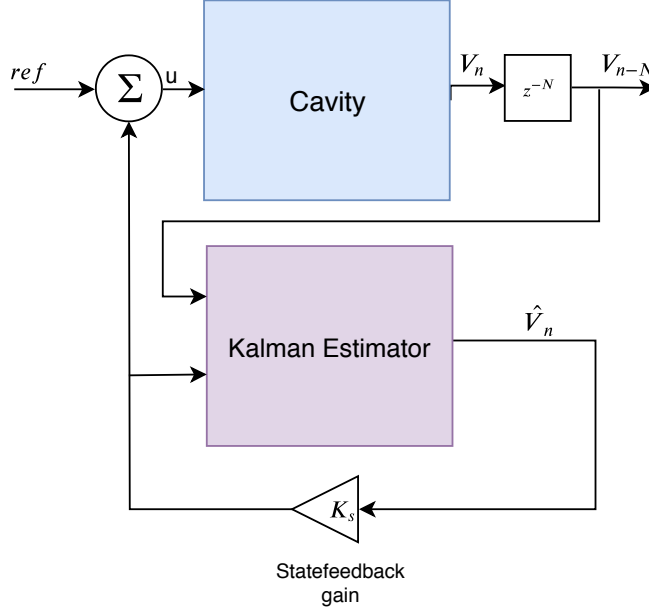


Figure 4.3: Illustration showing the Kalman estimator to estimate V_n , given the measurable V_{n-N} .

A Kalman estimator can be used to introduce a way to predict states of a system, given previous measurements and a model of the system. The 'delayed' discrete Kalman estimation equation for a system with X_n as the state vector and Y_n as the output are:

$$\hat{X}_n = \Phi \hat{X}_{n-1} + \Gamma u_{n-1} - L \left(Y_{n-1} \hat{Y}_{n-1} \right) \quad (4.1)$$

Here Φ and Γ are the discrete system and input matrices, \hat{X}_n is the estimated state vector, \hat{Y}_{n-1} is the estimated output of the previous time step, and Y_{n-1} is the real output of the system of the previous time step.

In the case of the cavity, the system model has two states, the voltage in the cavity and its derivative, where only the voltage itself can be measured. As illustrated in figure 4.3 the necessary state needed for the design of a state feedback controller is the latest voltage in the cavity. Therefore a reduced order observer need to be designed focusing only on the delayed states of voltage $x_{1,n}$. This should be estimated based on the measurement Y_{n-N} . As can be observed from equation 4.1, the current estimate is based recursively on the previous estimates. Each state estimate can then be substituted in to the equation until it is only dependent on the Y_{n-N} measurement, as illustrated with $N = 3$:

$$\begin{aligned}
\hat{X}_n &= \Phi \hat{X}_{n-1} + \Gamma u_{n-1} + L \left(Y_{n-1} - \hat{Y}_{n-1} \right) \\
\hat{X}_n &= \Phi \left(\Phi \hat{X}_{n-2} + \Gamma u_{n-2} + L \left(Y_{n-2} - \hat{Y}_{n-2} \right) \right) + \Gamma u_{n-1} + L \left(Y_{n-1} - \hat{Y}_{n-1} \right) \\
\hat{X}_n &= \Phi \left(\Phi \left(\Phi \hat{X}_{n-3} + \Gamma u_{n-3} + L \left(Y_{n-3} - \hat{Y}_{n-3} \right) \right) + \Gamma u_{n-2} + L \left(Y_{n-2} - \hat{Y}_{n-2} \right) \right) \\
&\quad + \Gamma u_{n-1} + L \left(Y_{n-1} - \hat{Y}_{n-1} \right)
\end{aligned}$$

The process of substituting and storing previous control inputs and system outputs are automated by extending the state space matrices to include all N-delay states of x_1 . The state vector will then be:

$$\bar{X}_n = \begin{bmatrix} x_{1,n} \\ x_{2,n} \\ x_{1,n-1} \\ x_{1,n-2} \\ \dots \\ x_{1,n-N} \end{bmatrix} \quad (4.2)$$

State matrix is extended to:

$$\bar{\Phi} = \begin{bmatrix} \Phi & 0 \\ I & 0 \end{bmatrix} \quad (4.3)$$

Here I is the identity matrix of $[N \times N]$ delay dimensions. Γ and H are extended to corresponding sizes with N zeros:

$$\bar{\Gamma} = \begin{bmatrix} \Gamma \\ 0 \end{bmatrix} \quad (4.4)$$

$$\bar{H} = \begin{bmatrix} 0 & H \end{bmatrix} \quad (4.5)$$

An important part to introduce before designing the estimator is process noise v_n and measurement noise w_n as shown in Fig. 4.4. This expands the system equations to:

$$\bar{X}_{n+1} = (\bar{\Phi} \bar{X}_n + \Gamma u_n + v_n) \quad (4.6)$$

$$y_n = \bar{H} \bar{X}_n + w_n \quad (4.7)$$

Here \bar{X}_n is the extended state vector, $\bar{\Phi}$ is the extended system matrix, y_n is the output of the system, \bar{H} is the extended output matrix.

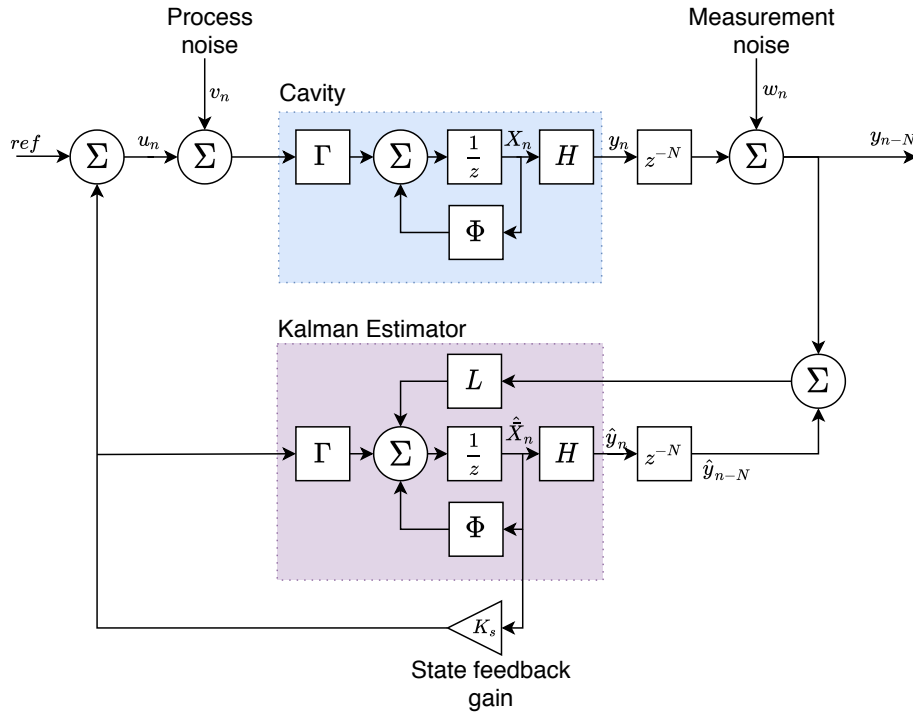


Figure 4.4: Illustration showing the Kalman estimator in more detail coupled with a state feedback gain K_s regulating based on the estimated \hat{V}_n .

Given the extended system matrices, a Kalman estimator can be implemented using two steps, predict and update. The predicting step includes a priori state estimate $\hat{X}_{n|n-1}$ and a priori error covariance estimate $P_{n|n-1}$.

$$\hat{X}_{n|n-1} = \bar{\Phi}_n \hat{X}_{n-1|n-1} + \Gamma_n u_{n-1} \quad (4.8)$$

$$P_{n|n-1} = \bar{\Phi}_n P_{n-1|n-1} \bar{\Phi}_n^T + Q_n \quad (4.9)$$

The update step estimates the output, calculates the Kalman gain L , and updates the state and covariance estimates.

$$\hat{y}_n = z_n - \bar{H}_n \hat{X}_{n|n-1} \quad (4.10)$$

$$S_n = \bar{H}_n P_{n|n-1} \bar{H}_n^T + R_n \quad (4.11)$$

$$L_n = P_{n|n-1} \bar{H}_n^T S_n^{-1} \quad (4.12)$$

$$\hat{X}_{n|n} = \hat{X}_{n|n-1} + L_n \hat{y}_n \quad (4.13)$$

$$P_{n|n} = (I - L_n \bar{H}_n) P_{n|n-1} \quad (4.14)$$

Q_n and R_n is the covariance of the process and measurement noise respectively. They are defined by:

$$Q_n = \mathbb{E} \left[v_n^T v_n \right] \quad (4.15)$$

$$R_n = \mathbb{E} \left[w_n^T w_n \right] \quad (4.16)$$

L_n is the Kalman gain which will be used in equation 4.1 to estimate the cavity voltage at time step n . L will be a $[N \times 1]$ dimensional vector. In reality on LINAC4 the estimation itself is implemented in the firmware, and needs only the Kalman gain vector L . As a cavity is a linear system, this gain can be calculated using the model of the cavity and equation 4.9, 4.11, 4.12 and 4.14 iteratively until the gain L converges. This implementation is explained further in section B.1 in the appendix.

4.2 VERIFICATION OF KALMAN VOLTAGE ESTIMATOR

The Kalman estimator from section 4.1, will in this section be tested and verified. The goal of the Kalman estimator is to predict the voltage in the cavity before the measurement delay, based on the delayed measurements. It will be tested both in simulation using the previously derived 2nd order model and given real openloop data from the CCDTL7 cavity in LINAC4.

KALMAN VERIFICATION USING MODEL OF SYSTEM

Two simulation setups was made to test the Kalman estimator using the plant model. Both setups added the beam loading to the input to the model, but only

one setup included beam loading to the input of the kalman estimator as well. The setups can be seen in figures 4.5 and 4.6.

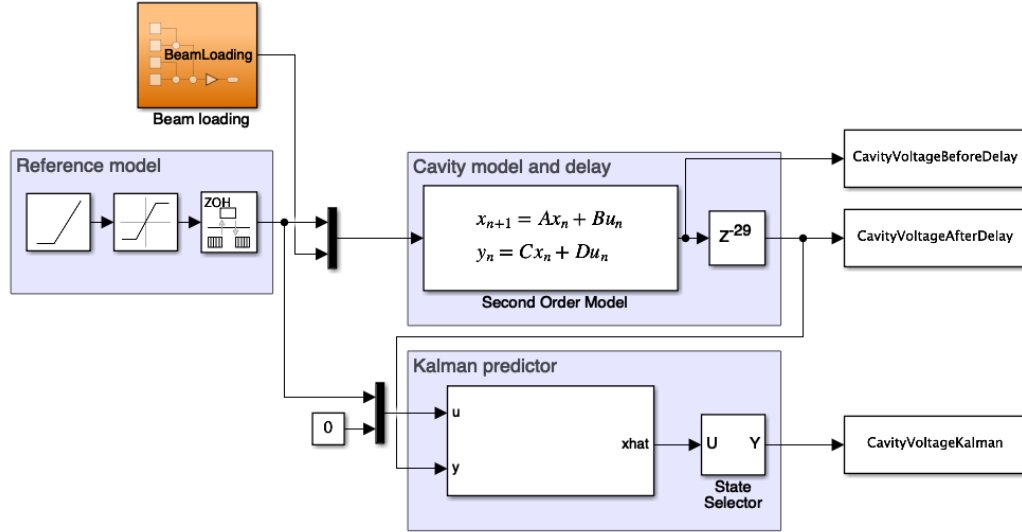


Figure 4.5: Simulink setup used to test and verify if the Kalman estimator outputs the expected state estimate compared to a delay model of a cavity without including the beam loading in the input to the kalman estimator.

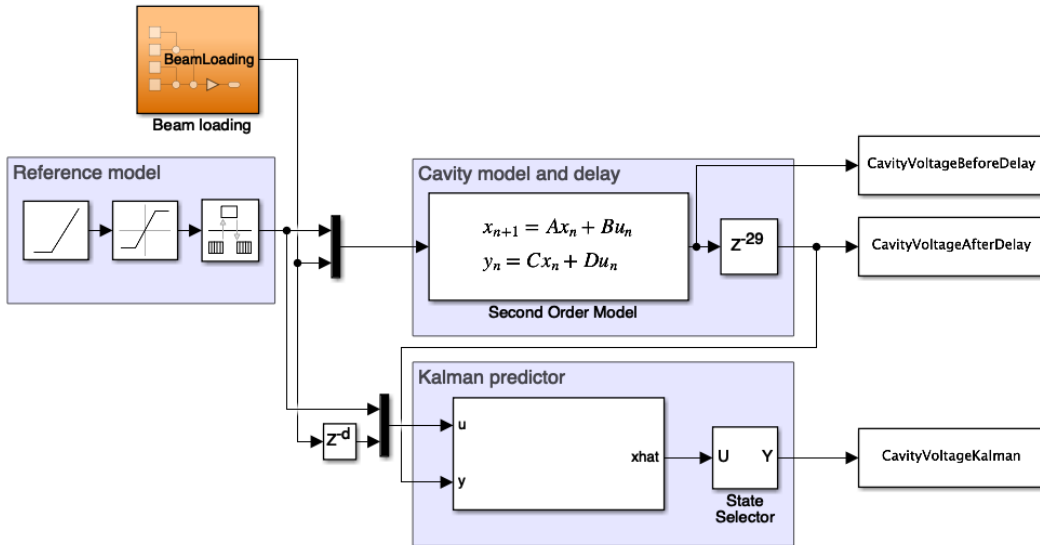


Figure 4.6: Simulink setup used to test and verify if the Kalman estimator outputs the expected state estimate compared to a delay model of a cavity and including the beam loading in the input to the kalman estimator - with the possibility to delay the beam loading signal to simulate the measurement delay.

Using these structures, and selecting the first state estimate from the Kalman estimator, \hat{V}_n , the estimates can be logged and compared to the model outputs before and after the measurement delay.

In figure 4.7 the Kalman voltage estimation is compared with the transient response of the model before the measurement delay. As expected since they are both based on the same model, the estimated state \hat{V}_n follows exactly the cavity voltage.

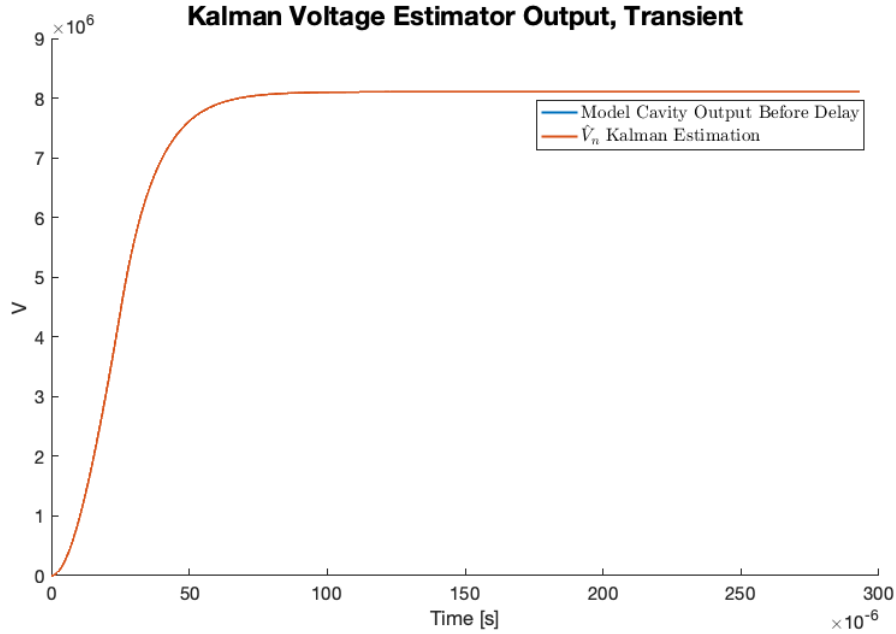


Figure 4.7: Comparison of the Kalman state estimate of \hat{V}_n and the cavity model voltage output before the added measurement delay. They match completely as expected.

Without including beam loading in the Kalman input, as in figure 4.5, the estimated voltage compared to the model output can be seen in figure 4.8. It is evident that the Kalman estimator is not able to detect the beam loading based on the output of the cavity model. This might be due to the 'forced' 0 beam loading input to the Kalman estimator coupled with the estimated output error $Y_n - \hat{Y}_n$ being of much lower magnitude than the states and inputs. This will make the previous estimated states and inputs dominant in the estimation of the new state.

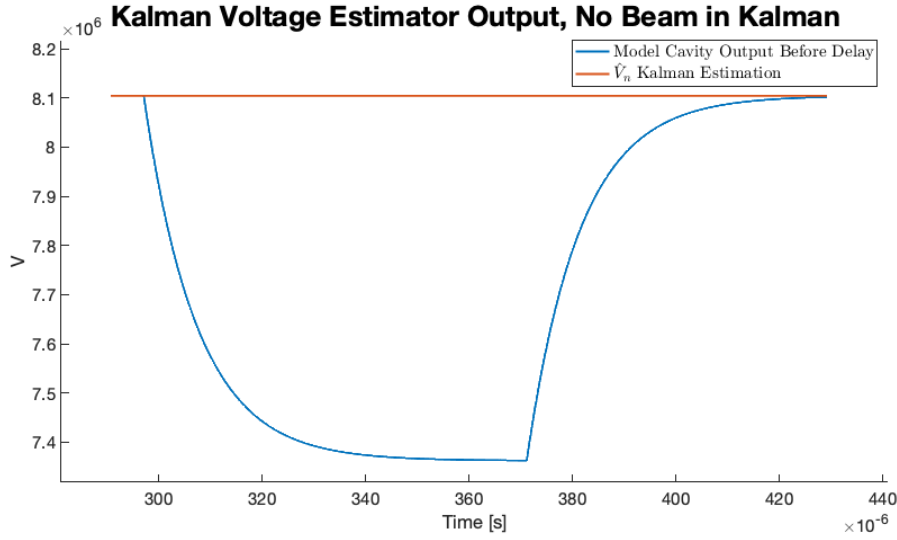


Figure 4.8: Comparison of the Kalman state estimate of \hat{V}_n and the cavity model voltage output before the added measurement delay during beam loading. The Kalman estimator is not able to estimate the beam loading without including it in the input.

Including beam loading in the Kalman input, as illustrated in figure 4.6, both with a delay to simulate the measurement delay and without yields the voltage estimations in figures 4.9 and 4.10. It can be seen in both situations the Kalman estimator is able to estimate the voltage drop in the cavity. Adding a delay to the beam loading signal results in a delayed beam loading estimate as expected.

It is expected that the Kalman estimator is able to estimate the exact output of the cavity before the delay, when the inputs to the system is identical to the Kalman inputs and both the system since the Kalman estimator uses the same model. In reality beam loading is seen as process noise, and therefore not a real signal that can just be included in the Kalman estimator. A suggestion can be to make an estimate of the expected voltage drop in the cavity from beam loading, and include that in the Kalman input in the real system. The effects of adding beam loading into the Kalman estimator will be investigated later when testing control systems, however designing a beam loading estimator is out of scope for this thesis.

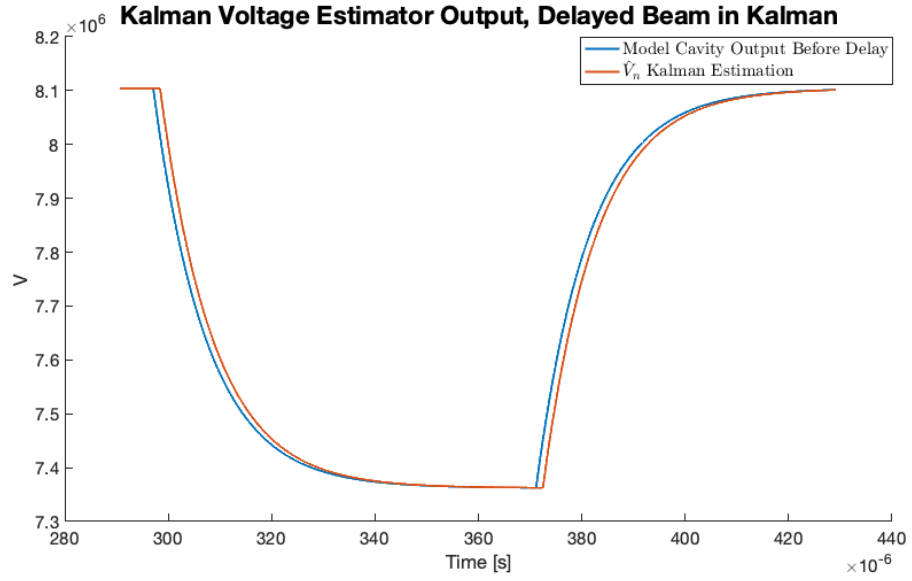


Figure 4.9: Comparison of the Kalman state estimate of \hat{V}_n and the cavity model voltage output before the added measurement delay during beam loading. The Kalman estimator is able to estimate the voltage during beam loading when it is included in the input, however delayed as the input signal is delayed too.

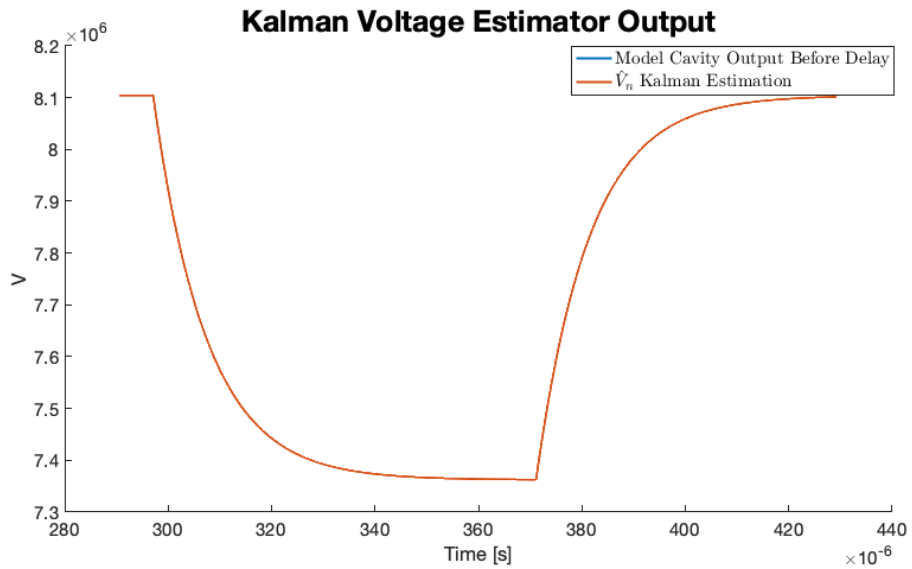


Figure 4.10: Comparison of the Kalman state estimate of \hat{V}_n and the cavity model voltage output before the added measurement delay during beam loading. The Kalman estimator is able to estimate the voltage during beam loading perfectly when it is included in the input with no delay.

KALMAN VERIFICATION USING CCDDL7 OPEN LOOP DATA

Having already recorded open loop data from the CCDDL7 cavity in LINAC4, the Kalman filter is also tested against a real cavity output. The data is the same response used in the verification of the cavity model, and can be seen in figure 2.11. The reference model including beam loading is replicated in Simulink and the cavity output data is loaded to the Kalman filter. The setup is shown in figure 4.11.

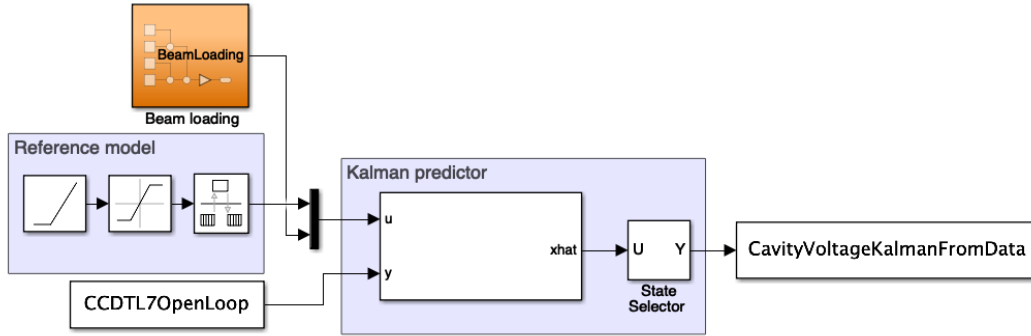


Figure 4.11: Simulink setup used to test the designed Kalman estimator against real open loop data from the cavity.

The output of the Kalman estimator compared to the open loop CCDDL7 data can be seen in the following figures 4.12 and 4.13. The same behaviour is observed as with using the model of the cavity. The estimated voltage during the transient response rises earlier than the output data of the real cavity. The beam loading signal was both tested with and without the measurement delay. Both situations the voltage estimate follows the voltage drop in the cavity very closely. The designed Kalman estimator for voltage estimation and measurement delay handling is hereby verified and will be used in the following sections to design control strategies.

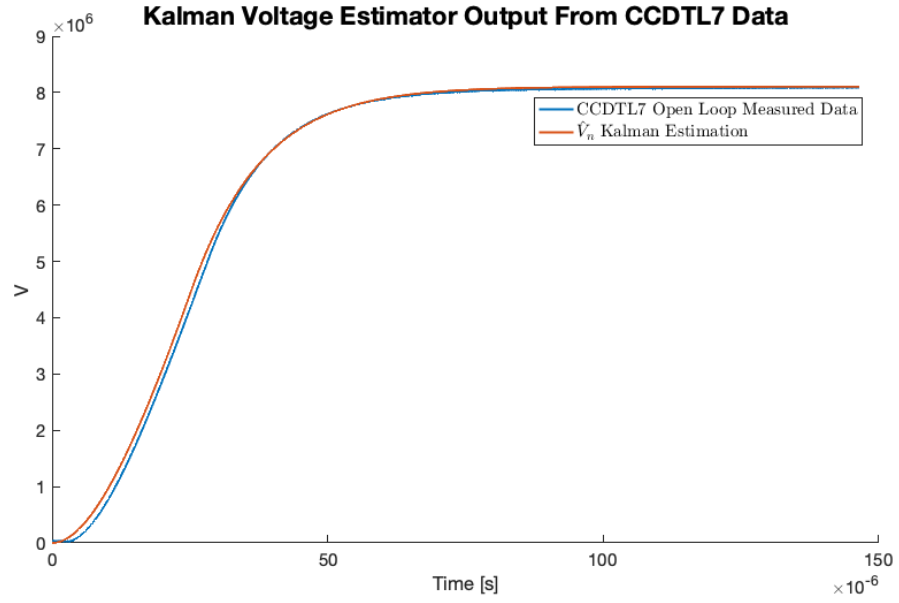


Figure 4.12: Zoomed in on transient response. It can be seen that the Kalman voltage estimation is ahead of the cavity output, as expected. Same behaviour as the simulation model.

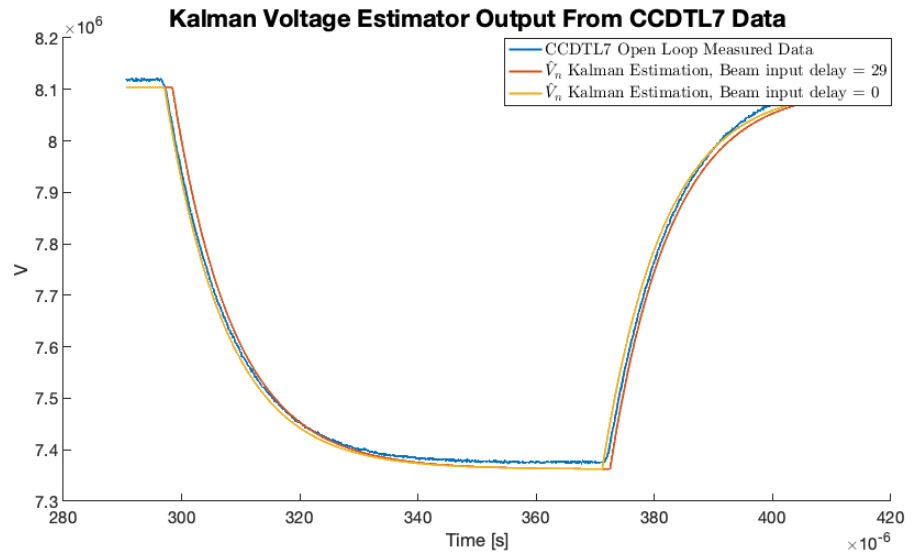


Figure 4.13: Zoomed in on response to beam loading. Same behaviour as in simulation.

4.3 LQR REGULATOR FOR CAVITY VOLTAGE CONTROL

Being able to estimate the cavity voltage \hat{V}_n a regulator can be designed. Section 2.3 investigated the measurement noise properties, and concluded it not to be white noise and thereby not Gaussian. Likewise the process noise in the system is not Gaussian and therefore the regulator is chosen to be a Linear Quadratic Regulator (LQR). The LQR regulator is represented as the state feedback gain K_s in the control loop shown in Fig. 4.4.

System equations as given by equations 4.17 and 4.18 can be used to obtain a state feedback gain K_s .

$$X_{n+1} = \Phi X_n + \Gamma u_n \quad (4.17)$$

$$Y_n = HX_n \quad (4.18)$$

An LQR controller is said to be an optimal controller, as the state feedback gain is found by solving an optimisation problem. A state feedback gain K_s needs to be found, such that the cost function J is minimised. The general finite-horizon discrete time cost function is given in the following equation 4.19 [22].

$$J = \mathbb{E} \left[x_K^T F x_K + \sum_{i=0}^{K-1} \left(x_i^T Q x_i + u_i^T R u_i \right) \right] \quad (4.19)$$

Here x_i and u_i is the current states and inputs respectively while x_K is the final state, and F is the weight on the final state. F can be used as a tuning parameter to punish the regulator to reach a certain final state. Q and R are also tuning matrices to weight states and inputs respectively.

Using discrete time notation, the state feedback gain can be found by:

$$K_s = \left(R + \Gamma^T S_{n+1} \Gamma \right)^{-1} \Gamma^T S_{n+1} \Phi \quad (4.20)$$

Here S is the solution to the Discrete Algebraic Ricatti Equation (DARE), which is found backwards in time:

$$S_n = Q + \Phi^T S_{n+1} \Phi - K_s^T \Gamma^T S_{n+1} \Phi \quad (4.21)$$

Having found the state feedback gain K_s , the control input to the plant can be found by the control law given in equation 4.22.

$$u_n = -K_s \hat{X}_n \quad (4.22)$$

ADDING INTEGRAL CONTROL

To eliminate any potential steady state error an integral part is added to the control scheme. The control diagram is therefore updated to incorporate the integral state and including integral gain K_{int} as shown in figure 4.14.

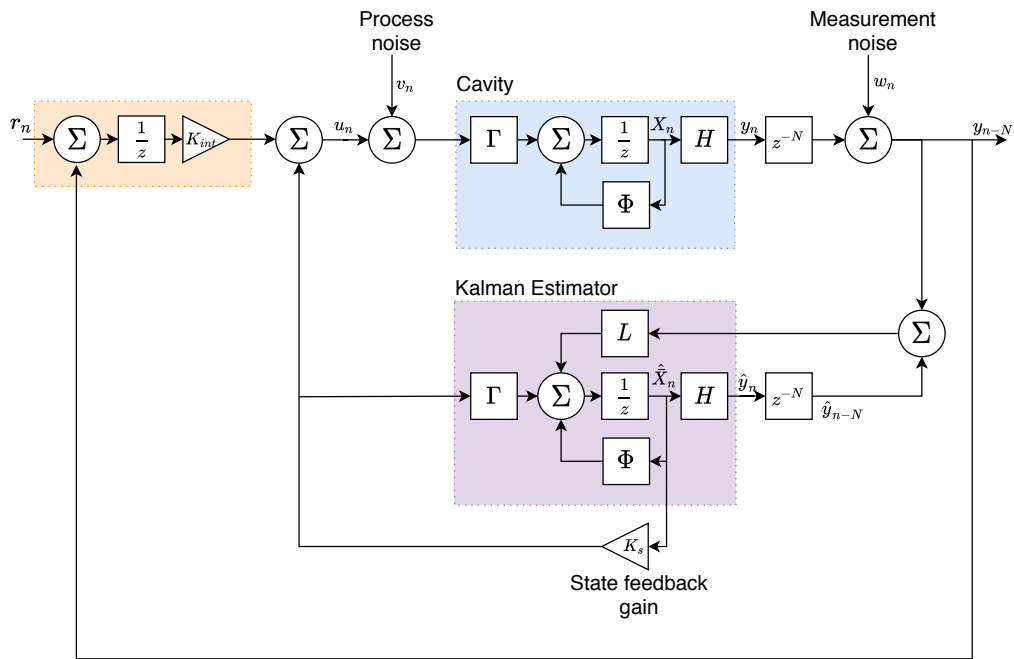


Figure 4.14: Illustration showing the Kalman estimator, LQG state feedback regulator and included integral control with reference r_n .

This is done by adding an integral state to the system $x_{i,n}$:

$$x_{i,n} = r_n - y_{n-N}$$

Here r_n is the reference input and y_{n-N} is the system output after the measurement delay. Essentially this means expanding the system matrices:

$$X_n = \begin{bmatrix} x_{i,n} \\ x_{1,n} \\ x_{2,n} \end{bmatrix} \quad (4.23)$$

$$\Phi_{int} = \begin{bmatrix} 1 & -H \\ 0 & \Phi \end{bmatrix} \quad (4.24)$$

$$\Gamma_{int} = \begin{bmatrix} 0 \\ \Gamma \end{bmatrix} \quad (4.25)$$

$$H_{int} = \begin{bmatrix} 0 & H \end{bmatrix} \quad (4.26)$$

This will result in the gain vector K , containing both the integral gain K_{int} and the state feedback gain K_s :

$$K = \begin{bmatrix} K_{int} & K_s \end{bmatrix} \quad (4.27)$$

CHOOSING Q AND R

For the design of the LQR controller, the state and input weights Q and R need to be chosen. Q and R can be chosen to obtain different responses of the controller. The choice is purely a design choice based on knowledge of the system and desired response. In this case the system with the added integral action has 3 states. Q has to be a symmetric positive semidefinite matrix with the same size as the system matrix, which in this case means Q must be a $[3 \times 3]$ matrix. R has to be symmetric positive definite matrix with the same size as number of inputs. In this case R has to be a $[2 \times 2]$ matrix, as the beam loading disturbance is considered an input.

The derivative of the voltage in the cavity can not be measured, only estimated and since there is a large difference in magnitude between the velocity state compared to voltage, a purely output estimate controller will be designed. The Q matrix will therefore be chosen so that the voltage derivative will have no effect. A possible choice of Q could be:

$$Q = \begin{bmatrix} 1 & 0 & 0 \\ 0 & 1 & 0 \\ 0 & 0 & 0 \end{bmatrix} \quad (4.28)$$

This would define the integral state and the voltage in the cavity to be of equal importance in terms of minimising the cost function. Several designs will in the next chapter be tested where different weights are put on the voltage estimate and the integral state.

As the system has 2 inputs, I_g and I_b where the beam loading current I_b is a disturbance to the system and can not be controlled, the R matrix is chosen to put a high weight on the controllable I_g input, and a very low weight on the beam loading current. An example could be:

$$R = \begin{bmatrix} 10 & 0 \\ 0 & 0.1 \end{bmatrix} \quad (4.29)$$

SIMULATION

Having designed a controller in chapter 4, the control loop is implemented in simulation. This is done to evaluate if the controllers perform as intended and to make sure that the controllers will stabilise the system, before implementing the control strategies on the real machine in the future. Avoiding any damage to equipment is of high priority, and therefore this section will describe setting up a simulation environment to mimic the behaviour of a LINAC4 cavity for the control strategies to be tested on.

5.1 SIMULATION ENVIRONMENT

Simulink is a powerful tool for simulating control systems and will be used for the simulation environment. The simulation is made up of different blocks connected by signal lines corresponding to either inputs or outputs.

The simulation environment can be seen in figure 5.1. Initially the beam loading is considered process noise and therefore not included in the Kalman estimator. The Kalman estimator will therefore behave as in figure 4.8, and it will be investigated how well a controller can regulate the voltage given the wrong \hat{V}_n state estimate during beam loading. The regulation effect of including beam loading in the Kalman estimator will be investigated later in the chapter. The reference model is designed based on a ramp and a upper limit block. This is to emulate the input drive to the real cavity, where the drive is ramped to reference in $25\mu s$. Next is a discrete time integrator before the integral gain, together adding integral action to prevent steady state errors. The previously derived state space model, the designed Kalman estimator and LQR state feedback gain are implemented using prebuilt Simulink blocks taking in the system matrices as inputs. Worth noting is the beam is added as process noise using a pulse with a magnitude corresponding to 10% of the reference voltage. The output of the plant (cavity voltage) is delayed by N timesteps before being saved to MATLAB workspace, for later evaluation. The entire simulation is running for a total of $1ms$ with a $45.43ns$ sample time and is based on the CCDTL7 cavity in LINAC4.

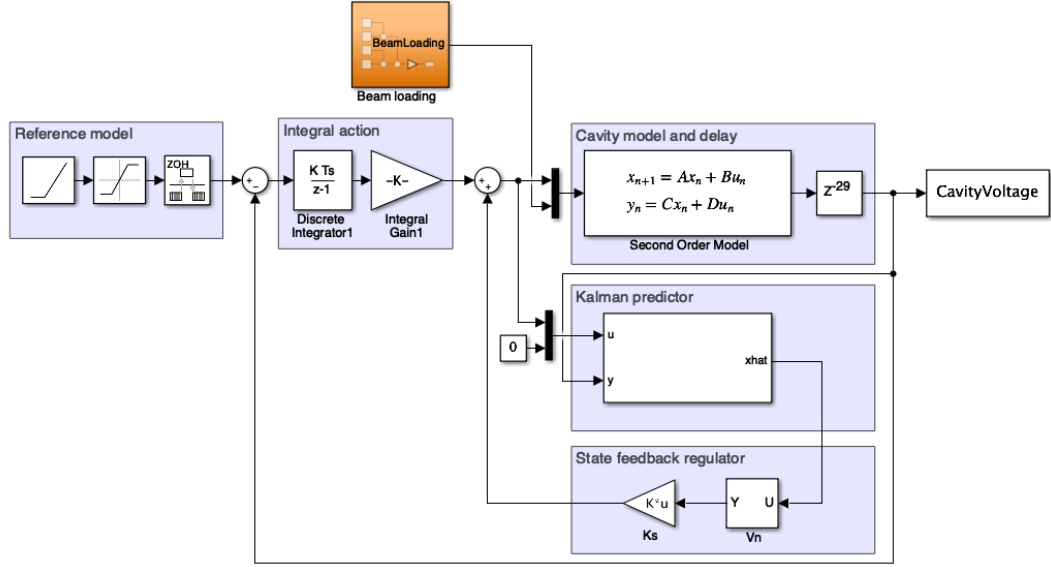


Figure 5.1: Simulation environment in Simulink of a single cavity loop.

As the designed controller is not regulating based on the delayed estimates, a state selector is added just before the state feedback gain to only choose the current estimated state, as it is shown in figure 5.1.

5.2 SIMULATING LQR RESPONSE TO BEAM LOADING

The purpose of designing a cavity control loop is to regulate the power to the cavity such that the voltage in the cavity reaches a desired reference voltage. This has been illustrated previously that it can be done in open loop by setting the reference voltage, however when a beam travels through the cavity the voltage drops. The designed LQ Regulators job is to minimise the deviation from the reference during beam loading. The reference ramped input of $8.1 \cdot 10^6 V$ can be seen in figure 5.2.

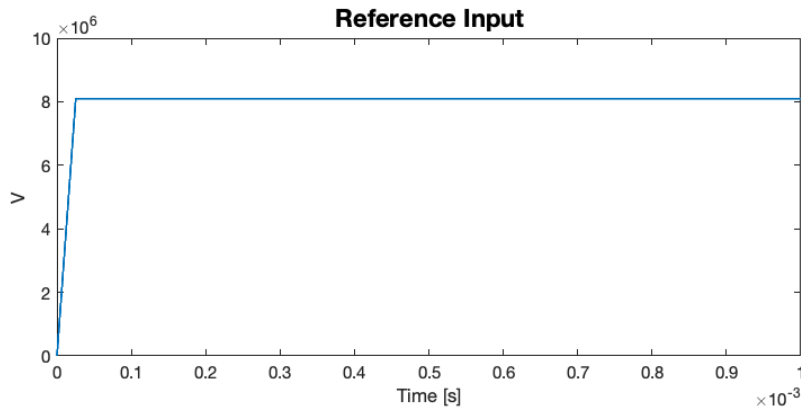


Figure 5.2: Reference input used showing the reference voltage being ramped to $8.1 \cdot 10^6 V$ in $25\mu s$.

Figure 5.3 shows the response of the LQ controller with integral action included compared to the open loop response of the system. It is clear that the LQ Regulator is stabilising, and is able to correct for beam loading. It can be seen that the voltage drops when the beam enters the cavity at $300\mu s$ and the voltage rises when the beam exits the cavity just before $380\mu s$. The crucial part is the first dip when the beam enters the cavity, as the voltage directly affects the acceleration of the beam. The rise of the voltage when the beam exits the cavity is due to integral wind-up and is not of importance as there are no particles under acceleration in the cavity at this point in time.

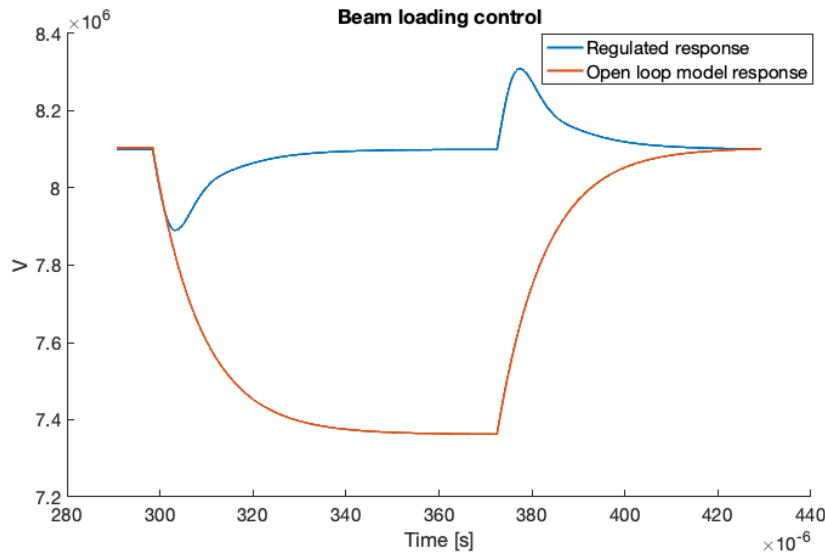


Figure 5.3: Verification of the designed controller regulating the voltage back to the reference during beam loading.

It is desirable to minimise the voltage dip to accelerate the particle bunch as evenly as possible. Two ways of doing that are investigated in this thesis. The first one being to tune the controller more aggressively by altering the penalising weights Q and R to allow the controller to regulate faster. In figure 5.4 various different LQ designs were tested to inspect the resulting response of the system. The RMSE of the different responses compared to the reference is outline in table 5.1 with the corresponding Q and R combinations shown in table 5.2.

It can be seen that the responses with the smallest deviations all use the Q_2 matrix which has a higher weight on the integral state penalising deviation. Varying the R matrix seems to have little impact on deviation from reference, however the higher the weight in R the higher the deviation for all Q s. It can be seen the Q and R combination of (Q_2, R_2) has the lowest deviation from reference of 778V on average when the beam is in the cavity. This corresponds to the light blue response with no oscillations in figure 5.4. The next section will investigate if inputting the beam loading in the Kalman estimator can improve the response of the closed loop system.

Table 5.1: Table showing the Root Mean Squared Error (RMSE) of the different gains tested. The RMSE is shown as both a value and a horizontal bar graph.

















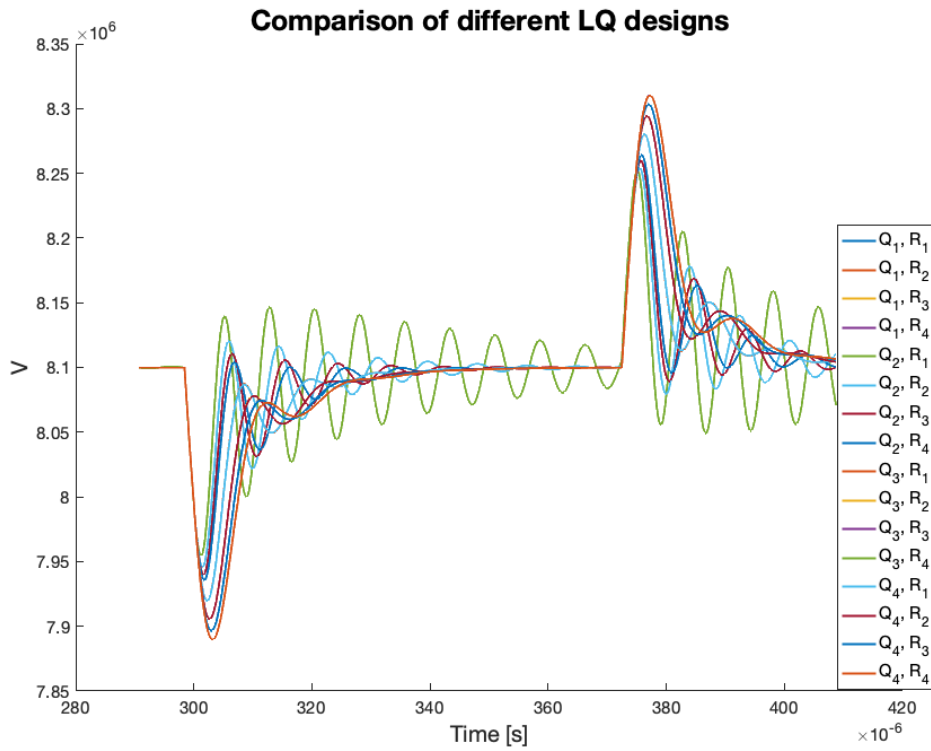
Q	R	RMSE	RMSE visualised
Q_1	R_1	979 V	
Q_1	R_2	1124 V	
Q_1	R_3	1223 V	
Q_1	R_4	1300 V	
Q_2	R_1	896 V	
Q_2	R_2	778 V	
Q_2	R_3	803 V	
Q_2	R_4	835 V	
Q_3	R_1	979 V	
Q_3	R_2	1124 V	
Q_3	R_3	1223 V	
Q_3	R_4	1300 V	
Q_4	R_1	980 V	
Q_4	R_2	1125 V	
Q_4	R_3	1224 V	
Q_4	R_4	1300 V	

Table 5.2: Table showing the different Q and R matrices used to obtain the various responses.

$$Q_1 = \begin{bmatrix} 1 & 0 & 0 \\ 0 & 1 & 0 \\ 0 & 0 & 0 \end{bmatrix} \quad Q_2 = \begin{bmatrix} 10 & 0 & 0 \\ 0 & 1 & 0 \\ 0 & 0 & 0 \end{bmatrix} \quad Q_3 = \begin{bmatrix} 1 & 0 & 0 \\ 0 & 0.1 & 0 \\ 0 & 0 & 0 \end{bmatrix} \quad Q_4 = \begin{bmatrix} 1 & 0 & 0 \\ 0 & 10 & 0 \\ 0 & 0 & 0 \end{bmatrix}$$

$$R_1 = \begin{bmatrix} 10 & 0 \\ 0 & 0.1 \end{bmatrix} \quad R_2 = \begin{bmatrix} 20 & 0 \\ 0 & 0.1 \end{bmatrix} \quad R_3 = \begin{bmatrix} 30 & 0 \\ 0 & 0.1 \end{bmatrix} \quad R_4 = \begin{bmatrix} 40 & 0 \\ 0 & 0.1 \end{bmatrix}$$

**Figure 5.4:** Comparison of different designs of the LQ controller showing that the performance of the LQ regulation can be improved by choosing different Q and R matrices.

5.3 INCLUDING BEAM LOADING IN KALMAN ESTIMATOR INPUT

The concept of adding the beam loading to the input of the Kalman estimator has been explained and pictured in section 4.2 and the simulation setup explained in section 5.1. This section will investigate whether introducing the beam loading in the Kalman estimator will improve the regulation. It was tested in simulation, as the beam loading can be directly connected to the input of the Kalman filter by adding it as shown in the following figure 5.5.

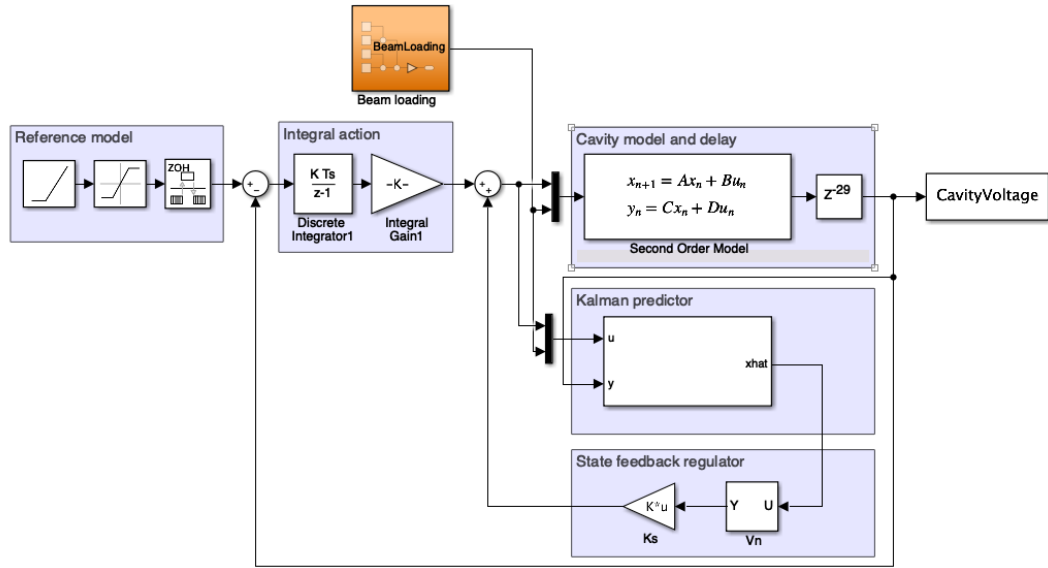


Figure 5.5: Simulation environment used for testing the Beam loading included in the input to the Kalman Estimator.

In simulation the exact beam loading amount can be inputted at the exact time it occurs in the cavity. As this might not be possible to know in reality, this section investigates effects of deviations in both timing and magnitude of beam loading. Starting with analysing adding a delay to the inputted beam loading signal to simulate a measurement and or estimation delay. Multiple cases are compared in figure 5.6. Relatively even distribution of delays are added to the beam loading input to the Kalman filter, from 0 time step delay up to full 29 time step delay of the CCDTL7 cavity. The resulting response showed to have an improvement of between 3.76 and 1.57 times less deviation from reference during beam loading, and thereby manage to correct for the beam loading faster than without including it in the input to the Kalman filter. The deviation is measured using the Root Mean Squared Error (RMSE). It is evident, both from the response graph and the data

Table 5.3: Table showing the Root Mean Squared Error (RMSE) of the different delays applied to the beam loading input in the Kalman estimator. The RMSE is shown as both a value, a percent improvement from the first row (reference deviation without beam in Kalman), and a horizontal bar graph.

Delay	RMSE	Improvement	RMSE visualised
– N/A –	424.7 V	–	<div></div>
0	89.24 V	376%	<div></div>
5	101 V	321%	<div></div>
10	113.8 V	273%	<div></div>
15	127.1 V	234%	<div></div>
20	140.7 V	202%	<div></div>
25	154.4 V	176%	<div></div>
29	165.3 V	157%	<div></div>

that including beam loading, even with a delay, into the Kalman estimator shows substantial potential for minimising the voltage drop during beam loading. In this case the state feedback and integral gain were kept constant for comparison, however coupled with a more aggressive tune as illustrated in the previous section could improve the response even further.

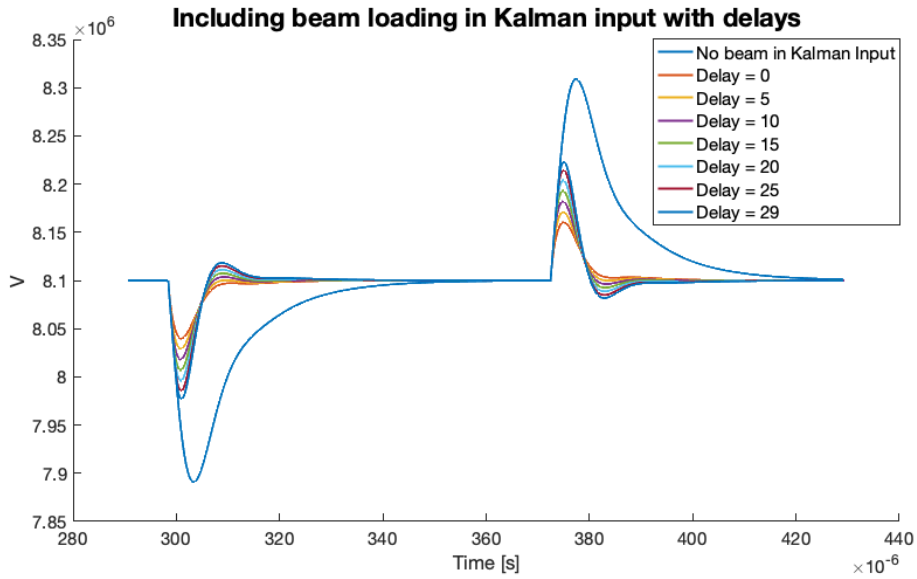


Figure 5.6: Including beam loading in the Kalman estimator input to artificially drive the input signal higher when the beam loading occurs. The controller is able to react and correct for beam loading much faster as no delay through measuring even with the signal being delayed.

Second part of this analysis is to investigate if the magnitude of the beam estimate varies from the actual beam loading. To test this, the beam loading was scaled evenly up to 30% larger and smaller and compared with not including the beam loading in the Kalman estimator. Figure 5.7 shows the responses of scaled beam loading in Kalman compared to the response without including beam loading in Kalman. Table 5.4 shows the beam loading scale factor, the RMSE from reference, the difference in RMSE compared to the non-scaled beam loading, the improvement over not including beam loading in Kalman and the RMSE visualised. In both the figure and the table it is evident, that even though the magnitude of the beam loading is not estimated perfectly, even with a deviation of more than 30%, it is still beneficiary to include beam loading in the Kalman estimator.

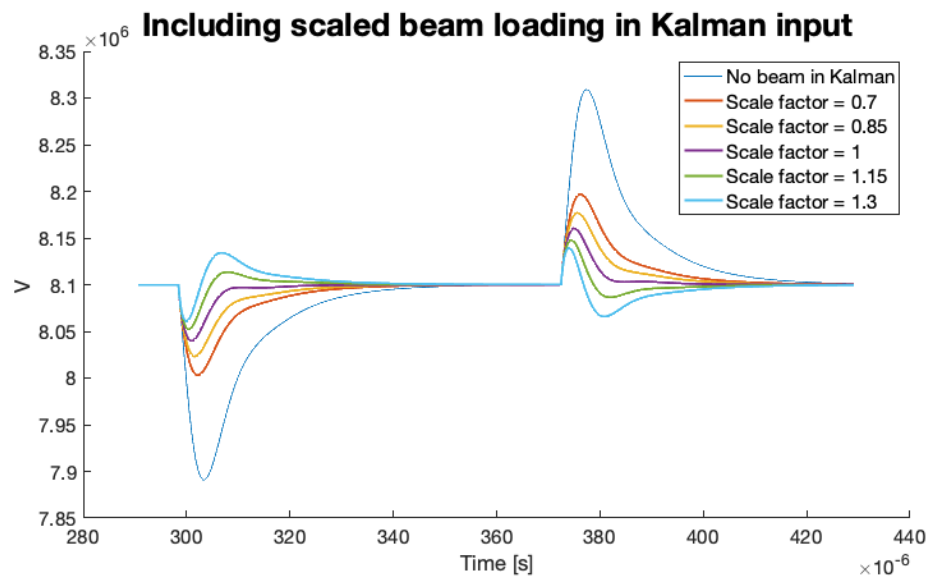


Figure 5.7: Including beam loading in the Kalman estimator input to artificially drive the input signal higher when the beam loading occurs. The beam loading signal was scaled to mimic that they magnitude of beam loading not being estimated correctly.

Table 5.4: Table showing the Root Mean Squared Error (RMSE) of the different scaled beam loading inputs in the Kalman estimator. The RMSE is shown as both a value, a percent difference in deviation from the non-scaled beam loading, improvement from the reference without beam in Kalman, and a horisontal bar graph.

Scale factor	RMSE	Difference	Improvement	RMSE visualised
– N/A –	424.7 V	–	–	<div></div>
0.70	180.9 V	-51%	135%	<div></div>
0.85	132.1 V	-32%	222%	<div></div>
1	89.24 V	–	376%	<div></div>
1.15	65.29 V	37%	550%	<div></div>
1.30	79.63 V	12%	433%	<div></div>

STABILITY ANALYSIS

The previous chapters have designed and tested different control strategies in order to minimise deviation from the reference voltage during beam loading. Two methods of minimising the deviation were introduced, namely designing the Q and R matrices differently and introducing beam loading estimate in the input to the Kalman estimator. Both methods were tested in previous chapter 5, and leads to the next discussion, namely stability of the system. This chapter will analyse the stability of a cavity control loop from two different perspectives: Stability in terms of how aggressive the controllers can be tuned while keeping the system stable, and in terms of parameter variations of the model used to design the cavity control loop. Both stability aspects will be tested using a Monte Carlo type simulation by simulating varying gains and model parameters. Section 6.1 will investigate the stability of the system when varying LQ gains, and 6.2 will investigate parameter variation stability of the system model.

6.1 CONTROLLER GAIN STABILITY

This section investigates how aggressive the controller gains can be tuned before the system becomes unstable. This is an important and interesting analysis as it will give an overview to CERN of limits to how aggressive the cavity controllers can be tuned without affecting stability. From CERNs perspective, it is desirable to have a controller that can react as fast as possible to beam loading, but still be stable. This section assumes the cavity model to be a perfect representation of the actual cavity. As the cavity control loops on LINAC4 are setup to take state feedback gains and integral gain, these will be the values of comparison in this section. A basis of state feedback and integral gains are used:

$$K_s = -14.7$$

$$K_{int} = 0.2150$$

Corresponding Q and R matrices:

$$Q = \begin{bmatrix} 0.05 & 0 & 0 \\ 0 & 125 & 0 \\ 0 & 0 & 0 \end{bmatrix} \quad R = \begin{bmatrix} 1 & 0 \\ 0 & 0.1 \end{bmatrix}$$

To test the stability of the system LQ gains were varied evenly from 33% of their original values up to 66% higher than their original values. 5 values were chosen for each gain:

$$K_s = \begin{bmatrix} -4.8517 & -9.7035 & -14.7023 & -19.5540 & -24.4058 \\ 0 & 0 & 0 & 0 & 0 \end{bmatrix}$$

$$K_{int} = [0.0710 \quad 0.1419 \quad 0.2150 \quad 0.2860 \quad 0.3569]$$

The simulation environments previously described were slightly modified to run 25 times and varying either K_s or K_{int} each run. The resulting responses are plotted in figure 6.1 and for comparison their corresponding RMSE listed in table 6.1. It can be seen that the controller causes the system to become unstable when the state feedback gain is $K_s = -4.86$ and the integral gain is either $K_{int} = 0.2860$ or $K_{int} = 0.3569$. In the case where $K_s = -4.86$ and $K_{int} = 0.2150$ there is a high amount of oscillations, but they seem to converge back to the reference. Generally it is observed that a high integral gain can potentially cause the system to become unstable due to integral windup, whereas a high state feedback gain makes the system have a slower response to beam loading, which is not desired.

It can also be concluded that adding beam loading to the Kalman input does not effect stability of the system. However this test further confirms that including an estimate of the beam loading in Kalman input reduces the deviation from reference significantly and makes the correction happen almost instantaneously. This is the ideal case where the exact beam loading is known, and the exact time it occurs, which makes the deviations presented in table 6.1 the best case scenario.

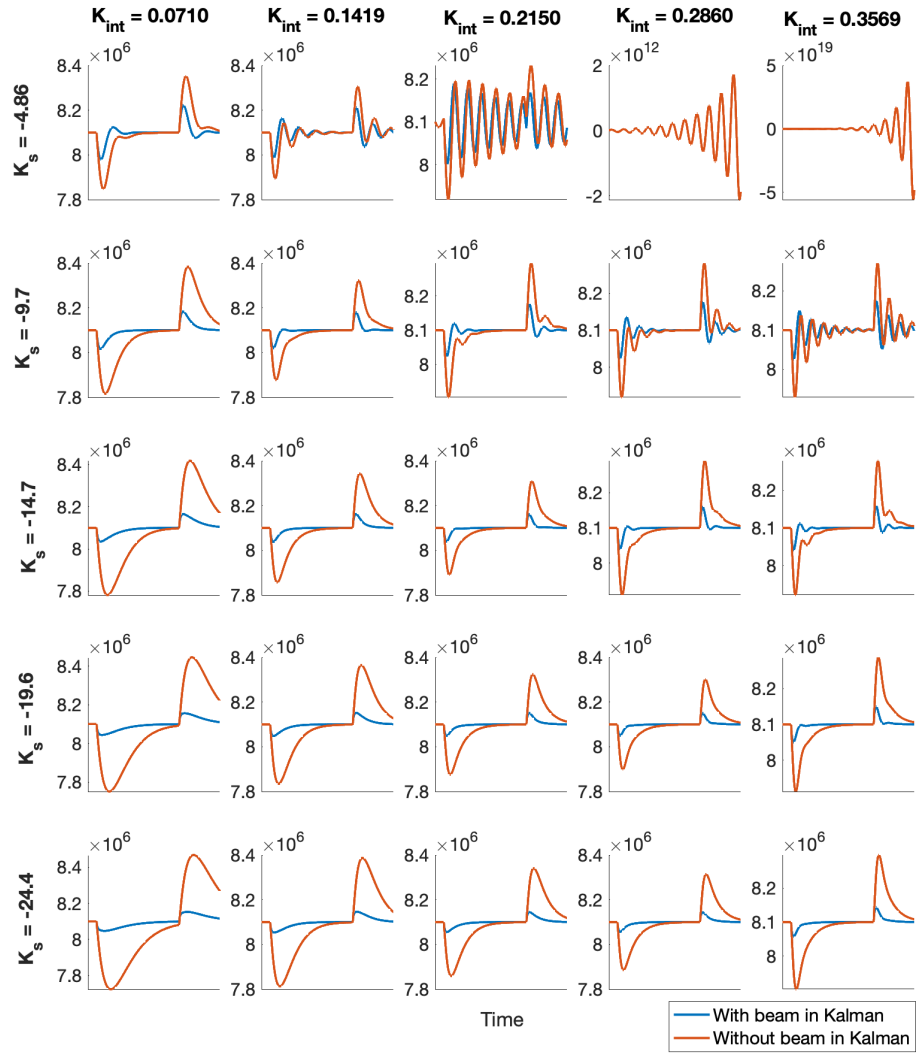


Figure 6.1: Responses of the cavity model in simulation varying the integral and state feedback gain to test the stability. It can be seen increasing the integral gain without increasing the state feedback gain leads to a faster response but also in some cases oscillations and even makes the system unstable.

Table 6.1: Overview of the 25 gain combinations tested for stability investigations. The gains together with the Root Mean Squared Error (RMSE) of the response both with beam loading included in Kalman input and without. The RMSE is shown as both as values and as combined horizontal bar graph.

State feedback Gain	Integral Gain	RMSE w/ beam	RMSE w/o beam	RMSE visualised
$K_s = -4.85$	$K_{int} = 0.071$	714 V	1783 V	
$K_s = -4.85$	$K_{int} = 0.142$	669 V	1208 V	
$K_s = -4.85$	$K_{int} = 0.215$	878 V	1298 V	
$K_s = -4.85$	$K_{int} = 0.286$	Unstable	Unstable	N/A
$K_s = -4.85$	$K_{int} = 0.357$	Unstable	Unstable	N/A
$K_s = -9.70$	$K_{int} = 0.071$	568 V	2600 V	
$K_s = -9.70$	$K_{int} = 0.142$	416 V	1549 V	
$K_s = -9.70$	$K_{int} = 0.215$	372 V	1143 V	
$K_s = -9.70$	$K_{int} = 0.286$	377 V	965 V	
$K_s = -9.70$	$K_{int} = 0.357$	435 V	925 V	
$K_s = -14.7$	$K_{int} = 0.071$	557 V	3367 V	
$K_s = -14.7$	$K_{int} = 0.142$	379 V	2031 V	
$K_s = -14.7$	$K_{int} = 0.215$	309 V	1469 V	
$K_s = -14.7$	$K_{int} = 0.286$	277 V	1177 V	
$K_s = -14.7$	$K_{int} = 0.357$	263 V	998 V	
$K_s = -19.6$	$K_{int} = 0.071$	573 V	3995 V	
$K_s = -19.6$	$K_{int} = 0.142$	382 V	2471 V	
$K_s = -19.6$	$K_{int} = 0.215$	300 V	1796 V	
$K_s = -19.6$	$K_{int} = 0.286$	257 V	1432 V	
$K_s = -19.6$	$K_{int} = 0.357$	232 V	1200 V	
$K_s = -24.4$	$K_{int} = 0.071$	595 V	4516 V	
$K_s = -24.4$	$K_{int} = 0.142$	397 V	2876 V	
$K_s = -24.4$	$K_{int} = 0.215$	307 V	2107 V	
$K_s = -24.4$	$K_{int} = 0.286$	258 V	1684 V	
$K_s = -24.4$	$K_{int} = 0.357$	227 V	1410 V	

6.2 MODEL PARAMETER VARIATION

This section will investigate the stability of the designed controllers in cases where the model of the cavity does not represent the real cavity well. This is tested by varying the model parameters Q_I and R/Q to investigate how the responses changes if the model used for control design varies from the actual cavity. Like in the case of the controller gain stability, 5 different values for both Q_I and R/Q were chosen and tested. Both parameters vary up to $\pm 50\%$ of the actual cavity parameters. The tested values for Q_I and R/Q is presented in the following arrays:

$$Q_I = [5700 \quad 8550 \quad 11400 \quad 14520 \quad 17100]$$

$$R/Q = [2852 \quad 4277 \quad 5703 \quad 7129 \quad 8555]$$

The stability of the system when the model parameters vary also depend on the tuning of the controller running in the cavity loop. As the controller gains themselves can cause instability as shown in the previous section, this section tests the same model parameter variations on three different sets of tuned controllers.

The first parameter variation test was done using the controller design with the least deviation from reference. The first parameter variation test is shown in figure 6.2. It can be seen that the system only becomes unstable in cases where Q_I in reality is between 25-50% smaller than the model used for control design, and in cases where R/Q is mostly higher than expected. In this case it seems R/Q is the most sensitive parameter as for all values of Q_I the smallest value of R/Q is able to stabilise the system.

The second parameter variation test used a slightly less aggressive controller tune and the resulting responses are shown in figure 6.3. As expected with a less aggressive tune, there are less cases of the system becoming unstable. The same behaviour is seen here where the system becomes unstable if R/Q is higher than the value used for control design and/or Q_I is significantly lower than expected.

The third and last parameter variation test was done using a very slow response tune of the controller, and the resulting responses is shown in figure 6.4. With this slower tune, all the responses are stable. It is also clear, that when Q_I increases, the dynamics of the system is smoothed out and becomes slower. Whereas the opposite is the case with R/Q making the responses sharper and faster when the value increases.

In all three tests inputting the beam loading into the Kalman filter does not affect stability of the system, and as in all previous tests shows mostly vast improvements in performance compared to not including it.

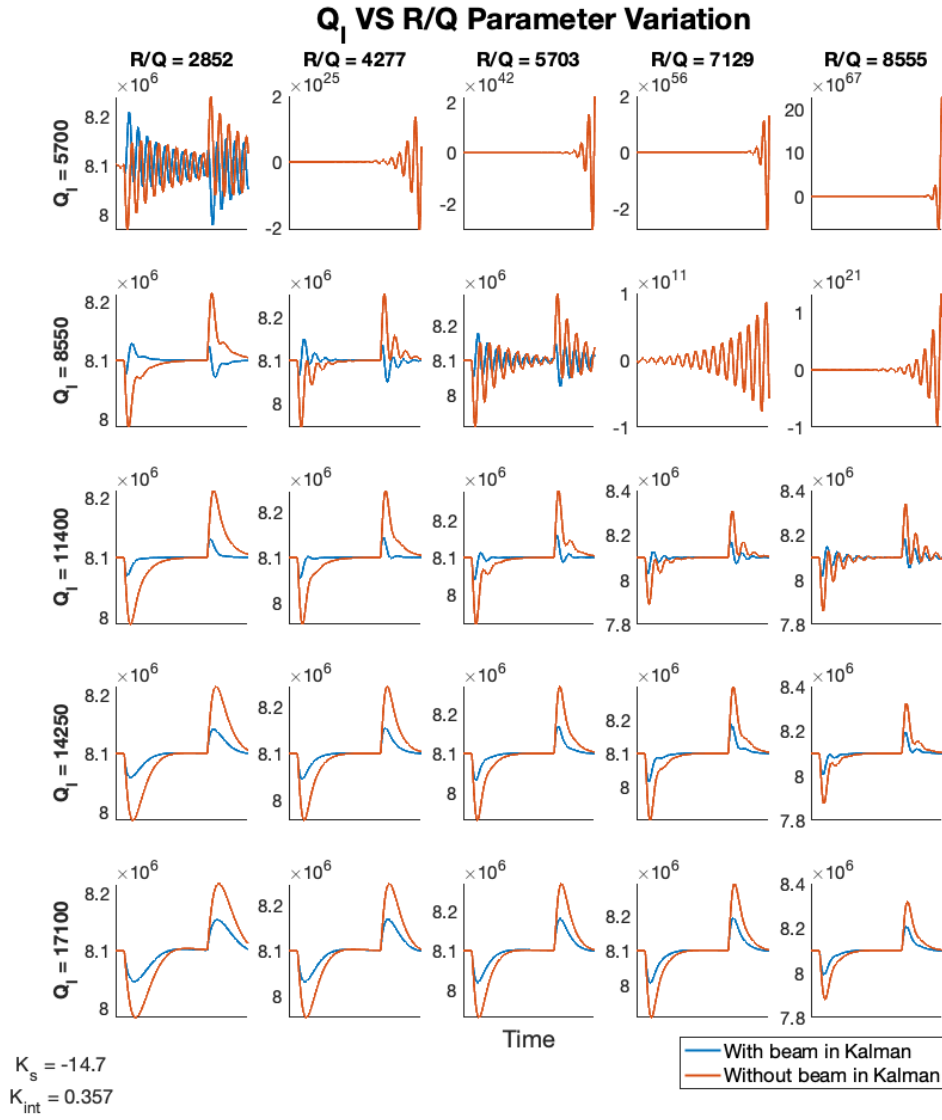


Figure 6.2: Stability of the system simulating cases where the model differs the 'real' cavity. The test used an aggressively tuned controller and shows cases of instability when Q_I is lower than expected and mostly when R/Q is higher than expected.

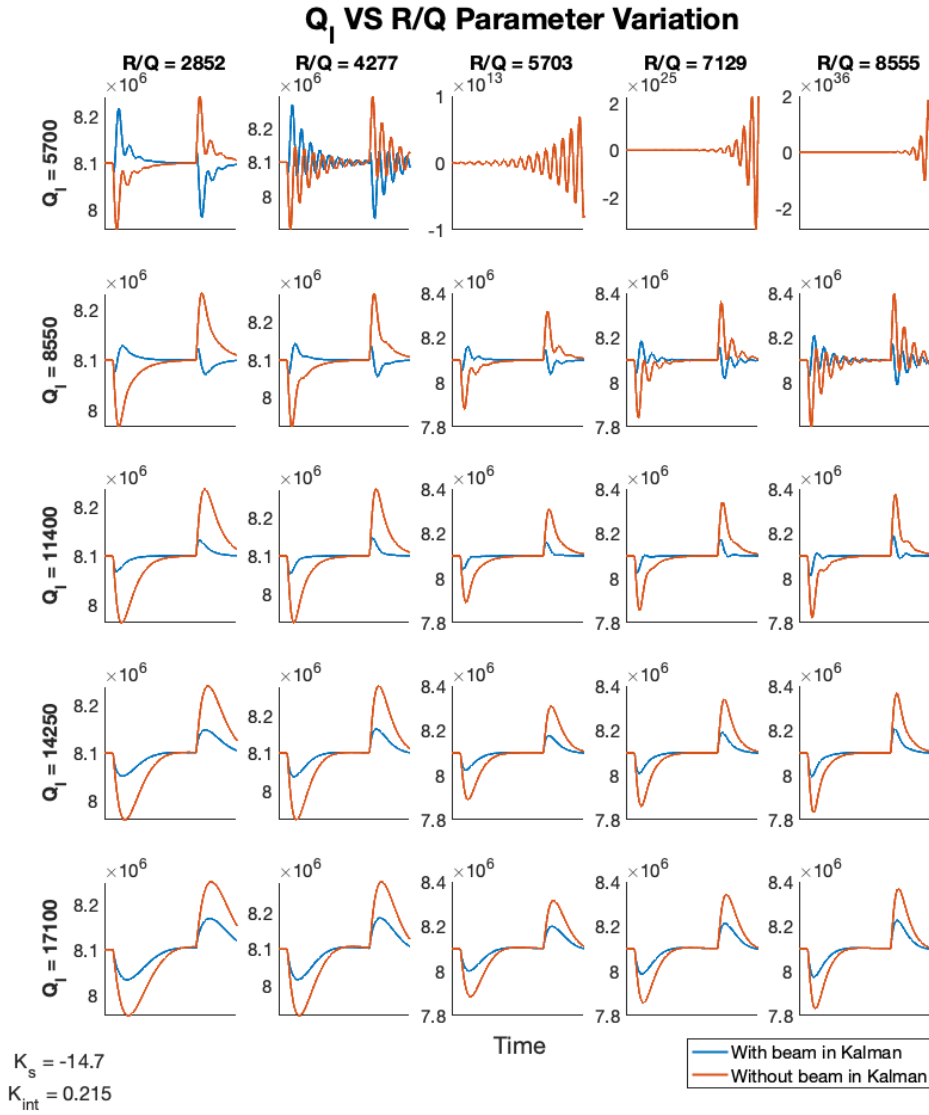


Figure 6.3: Stability of the system simulating cases where the model differs the 'real' cavity. The test used a moderately tuned controller and shows cases of instability only when Q_I is 50% lower than expected and mostly when R/Q is higher than expected.

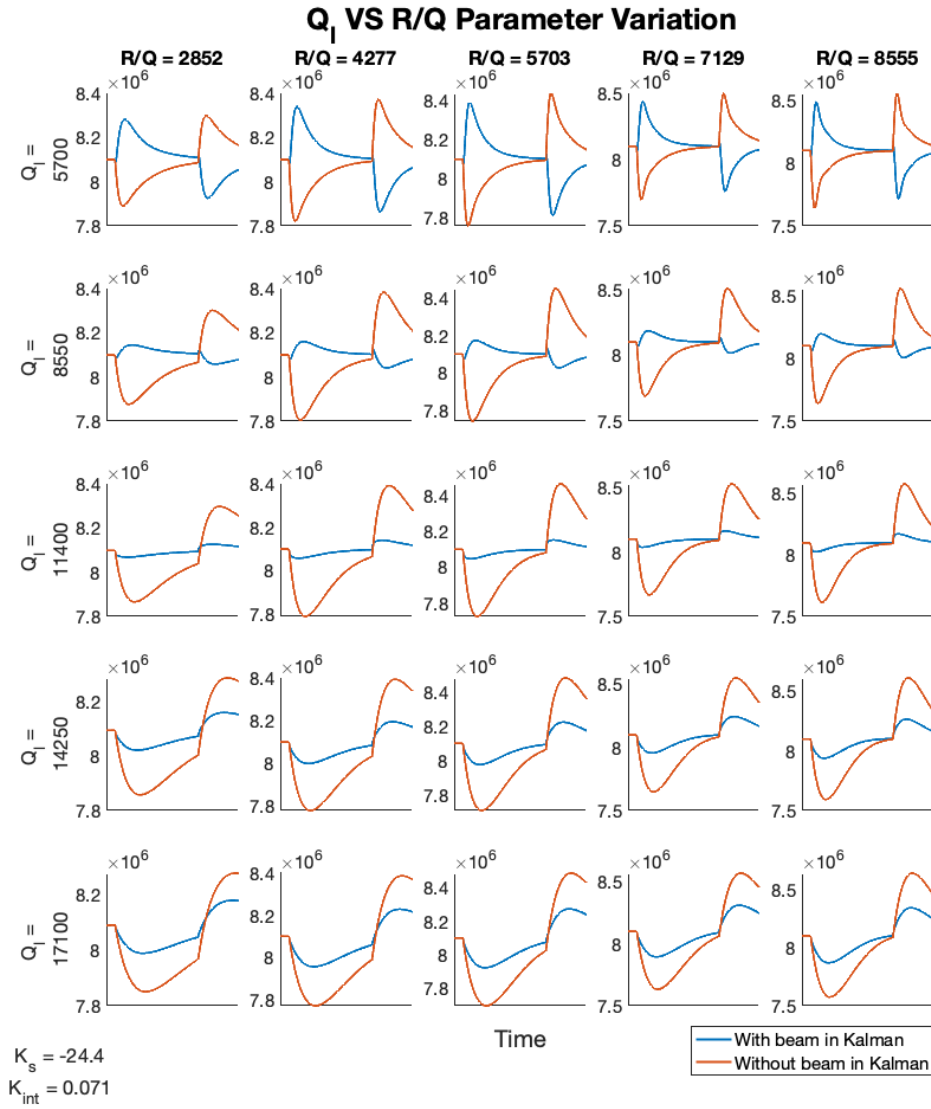


Figure 6.4: Stability of the system simulating cases where the model differs the 'real' cavity. The test used a slow tuned controller and shows no cases of instability.

Overall it was found that the parameters for the real cavity has to vary a somewhat large amount from the model used to design control strategies, before the system becomes unstable. Generally it was found that the R/Q parameter which has to do with the shape of the cavity, is the most sensitive parameter. The region of instability depends on the design of the controller, but is generally where the value of Q_l in reality is lower than the model, and where R/Q in reality is mostly higher than the model. From the three stability variation tests done in this thesis, it can be concluded that as long as the parameters vary less than 25% from reality, the

system is stable. Worth noting however is that this is only stability in terms of the cavity itself, and the Klystron supplying the power to the cavity might have lower stability thresholds, potentially causing the complete system to become unstable before the cavity does.

EVALUATION

7.1 CONCLUSION

This thesis set out to explore ways to optimise cavity control loops for CERNs newest linear particle accelerator - the LINAC4. The concept of beam loading was introduced as charged particles absorb energy stored in an RF cavity to accelerate. This results in the voltage in the cavity dropping, and ultimately causes the quality of the beam to decrease as the individual particles in a bunch gets accelerated differently and uneven.

It was analysed and found that most linear particle accelerators used around the world are modelled as a first order low pass filter, and uses either PI or LQ Regulators to correct for beam loading. This thesis modelled the cavity both as a first and second order system for comparison. The second order model proved to be a more precise representation of the dynamics of an RF accelerating cavity, and deviates 71.6% less from the real cavity response during beam loading and 8.2% less during the transient response.

The second order model was chosen as the superior representation and control design was based on this. The voltage in the cavity can be measured, but with a large time delay (29 time steps on the CCDTL7 cavity). A Kalman observer was designed to estimate the voltage in the cavity at the current time instance based on delayed output measurements. The Kalman estimator was verified, and concluded that including beam loading in the input to the Kalman estimator gave the most fitting estimation.

LQR controllers was designed based on the output estimate \hat{V}_n of the Kalman estimator. Combined with integral action the LQR controller was able to correct for beam loading as intended, and several different designs were tested in terms of how fast the control system responds to beam loading. It was here also investigated what effect including the beam loading in the Kalman estimator input had on the control response. It was found, that including an estimate of the beam loading in the Kalman estimator, greatly improved the response to be both faster and to deviate much less than not including it. Depending on the estimated beam loading size, and simulated measurement delay, including it in the Kalman input reduced

the deviation from reference with a factor between 1.57 to 3.76 compared to not including the estimate.

Lastly a stability analysis was made investigating the stability of the designed closed loop system. Firstly varying controller feedback and integral gains were simulated. This was mainly done as it can be used by CERN to see how much the gains can be tweaked before the system becomes unstable. It was found that mostly a high integral gain coupled with a low feedback gain causes instability.

More interestingly stability was investigated in terms of possible parameter variation. The main idea was to probe how robust the system is to differences in the model parameters compared to the actual cavity. This was simulated in a Monte Carlo type simulation varying the model parameters while keeping the controller parameters constant. It was found that depending on how aggressive the controller is tuned, the model parameters can be varied a large amount before the system becomes unstable. With the tested scenarios it was seen that one of the model parameters had to vary at least 25% before the system became unstable. It was here also concluded that the R/Q -parameter was the most sensitive parameter to variations.

Overall the thesis succeeded in modelling an RF accelerating cavity as a 2nd order system, designing a Kalman estimator to handle time delays, designing a regulator to correct for beam loading and analysing the closed loop stability of the designed system.

7.2 FUTURE WORK

The derived 2nd order model deemed to be a better fit to a cavity than a first order model, and therefore implementing the Kalman estimator using the 2nd order on LINAC4 may improve the voltage estimation, and thereby the closed loop response. This would have to be implemented in the LINAC4 firmware. As the order increases so does the computational complexity and the benefit in the voltage estimation need to be big enough for this to happen, but might be worth investigating.

What definitely is worth adding computational complexity is finding a way to include beam loading in the Kalman estimator input, as it showed to have great effect on the speed and settling time of the responses. This would involve making an estimator of the expected voltage drop in the cavity due to beam loading, and inputting it at the correct time to the Kalman filter.

In terms of stability of the system, it was in this thesis investigated by Monte Carlo simulations. If a more specific stability margin was to be needed, a Lyapunov stability analysis could be conducted. This is the analytical approach to stability

analysis by introducing polyhedral parametric uncertainty. Here it would be obvious to also include modelling of the non-linear Klystron supplying power to the RF cavity, and thereby analysing stability of the whole system.

BIBLIOGRAPHY

- [1] Martin Søndergaard Andersen. *Cavity Control Loop Optimisation For CERNs LINAC4 Linear Particle Accelerator*. Tech. rep. Aalborg University and CERN, 2019.
- [2] CERN. <https://home.cern/science/physics/early-universe>. The Early Universe.
- [3] <https://home.cern/science/physics/standard-model>. CERNs introduction to matter and the standard model.
- [4] CERN. <https://home.cern/science/physics/higgs-boson>. The Brout-Englert-Higgs mechanism (The Higgs Boson).
- [5] Esma Mobs. “The CERN accelerator complex - 2019. Complexe des accélérateurs du CERN - 2019”. In: (2019-07). General Photo. URL: <https://cds.cern.ch/record/2684277>.
- [6] CERN. <https://home.cern/science/accelerators/linear-accelerator-4>. Linear Accelerator 4 description.
- [7] CERN. <https://home.cern/science/accelerators/accelerator-complex>. CERNs accelerator complex description.
- [8] CERN. <https://home.cern/science/accelerators/high-luminosity-lhc>. CERNs High-Luminosity LHC project.
- [9] A. M. Lombardi. “Overview of Linacs”. In: *Proceedings of the CAS-CERN Accelerator School: Accelerators for Medical Applications* (2017).
- [10] Duncan A. Bryant. “The roles of static and dynamic electric fields in the auroral acceleration region”. In: *Journal of Geophysical Research* 107 (2002).
- [11] Daniel Dominguez and Arzur Catel Torres. *RF Cavity Animation*. <https://videos.cern.ch/record/1709737>. 2005.
- [12] Joachim Tückmantel. *Cavity-Beam-Transmitter Interaction Formula Collection with Derivation*. Tech. rep. ATS-Note-2011-002 TECH. CERN, 2011.
- [13] Fumihiko Tamura et al. “Simulations of beam loading compensation in a wideband accelerating cavity using a circuit simulator including a LLRF feedback control”. In: *Journal of Physics: Conference Series* 1350.1 (2019). ISSN: 1742-6588.

- [14] Y. Lee et al. "Design and development progress of a LLRF control system for a 500 MHz superconducting cavity". eng. In: *Journal of the Korean Physical Society* 61.2 (2012), pp. 203–207. ISSN: 0374-4884.
- [15] Zheqiao Geng. "Superconducting Cavity Control and Model Identification Based on Active Disturbance Rejection Control". eng. In: *IEEE Transactions on Nuclear Science* 64.3 (2017), pp. 951–958. ISSN: 0018-9499.
- [16] Bartosz Bielawski, Philippe Baudrenghien, and Robert Borner. "Recent developments in LLRF and its controls at CERN Linac4". In: (20190927).
- [17] Andrew McHutchon. "RLC Resonant Circuits". In: (2013-04). URL: <http://mlg.eng.cam.ac.uk/mchutchon/ResonantCircuits.pdf>.
- [18] MIT. "Capacitance and Dielectrics". In: (). Chapter 5, MIT course notes. URL: <http://web.mit.edu/8.02t/www/802TEAL3D/visualizations/coursenotes/modules/guide05.pdf>.
- [19] *Handbook of accelerator physics and engineering* /. eng. Elektronisk udgave. -2nd ed. Singapore: World Scientific Pub. Co., 2013. ISBN: 9789814415859.
- [20] Finn Haugen. *Discrete-time signals and systems*. http://teachtech.no/publications/discretetime_signals_systems/discrete.pdf. Euler discretisation of continuous time state space model. 2005.
- [21] Alan V. Oppenheim. *Discrete-Time Signal Processing*. eng. 3. ed. Upper Saddle River, N.J: Pearson. ISBN: 9780132067096.
- [22] G. F. Franklin, J.D. Powell, and A. Emami-Naeini. *Feedback Control of Dynamic Systems*. 7th Edition. Pearson, 2014.
- [23] M. Hou, P. Zitek, and R. J. Patton. "An observer design for linear time-delay systems". In: *IEEE Trans. on Automatic Control* 47.1 (2002), pp. 121–125.
- [24] A. E. Pearson and Y. A. Fiagbedzi. "An observer for time lag systems". In: *IEEE Trans. on Automatic Control* 34.4 (1989), pp. 775–777.
- [25] CERN. <https://wikis.cern.ch/display/ST/PyJapc>. PyJapc Documentation.

INTERFACING WITH LINAC4

This chapter explains the general methods of interfacing with LINAC4 controls software for setting up, monitoring and tuning RF Cavities.

A.1 INTRODUCTION TO INTERFACING WITH CERNs ACCELERATORS

As CERN is a high profile research facility, it is also a popular target for hackers. Obviously a lot of damage can be done if parameters are set wrongly, and CERNs machines can therefore only be accessed through virtual machines, with no internet access. When using a virtual machine on the CERN technical network (TN), operational and control panels can be launched through the Common Console Manager (CCM). In figure A.1 it is shown where to find and launch the cavity loop panel for the CCDTL7 cavity.

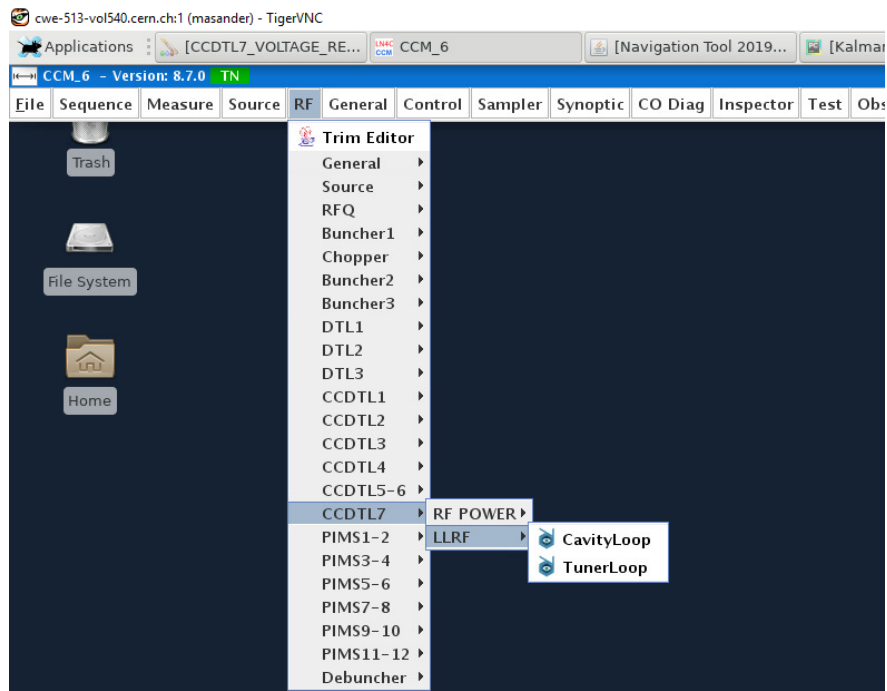


Figure A.1: CCM panel and navigating the menu to find the Cavity loops panel.

Opening up the cavity loop panel, all the important parameters can be accessed, as shown in figure A.2. The voltage set point, LQG feedback and Kalman settings, diverse filters and data acquisition can be accessed from this panel. In the “Kalman state” panel the LQG and Kalman vectors can be modified. However it is usually better to write the new settings to the FESA class using the FESA navigator or via a Python API (PyJAPC) explained in the following section A.2.

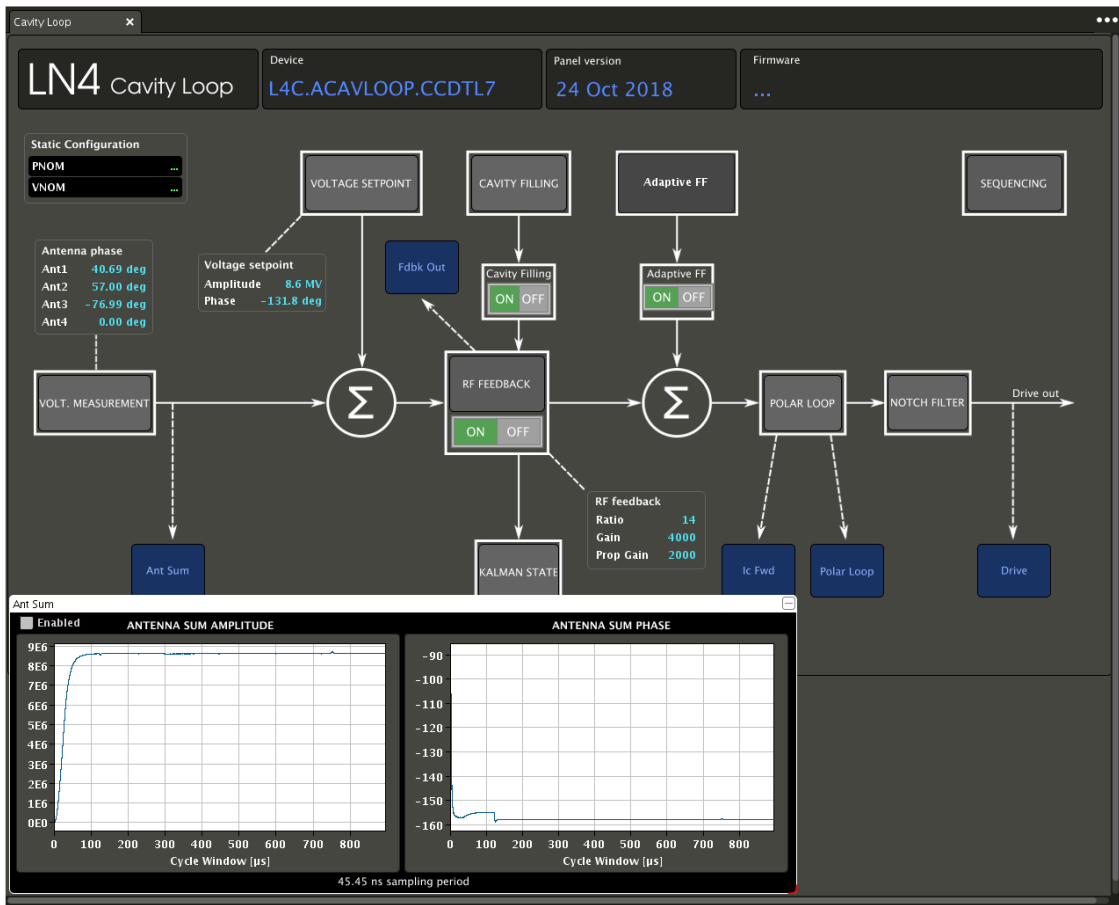


Figure A.2: CCDTL7 cavity loop panel.

In the CCM, global status and voltage data acquisition can also be found for all the cavities at once for better overview as shown in figure A.3 and A.4 respectively.

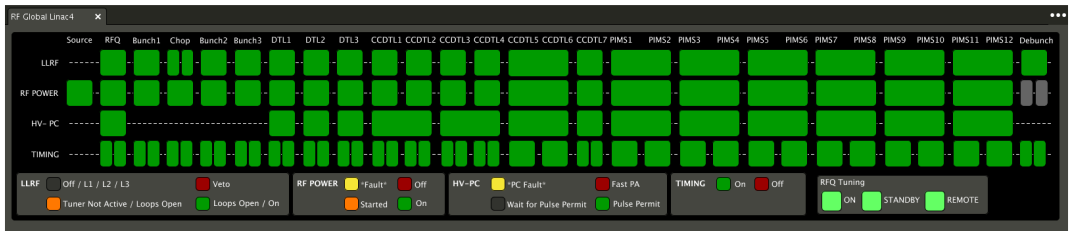


Figure A.3: LINAC4 global status panel showing state of all the cavities and feedback loops.

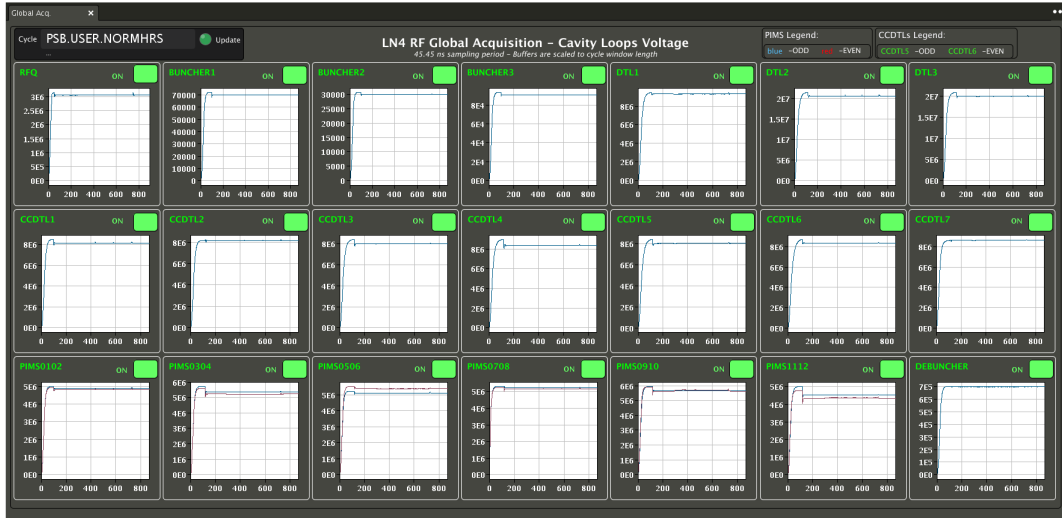


Figure A.4: LINAC4 global acquisition panel showing the voltage in all the cavities.

A.2 FESA CLASSES, PYJAPC AND NAVIGATORS

The CCM panels shown in the previous section is a great way of visually getting an overview of the state of the machine, cavities or make small adjustments. A more convenient way of changing multiple parameters and getting a collection of the parameters is through the underlying Front-End Software Architecture (FESA) classes. Via FESA classes, parameters of specific devices can be accessed and written. Using a FESA navigator and accessing the cavity loop of the CCCTL7 device, the Kalman properties is graphically viewed as shown in figure A.5.

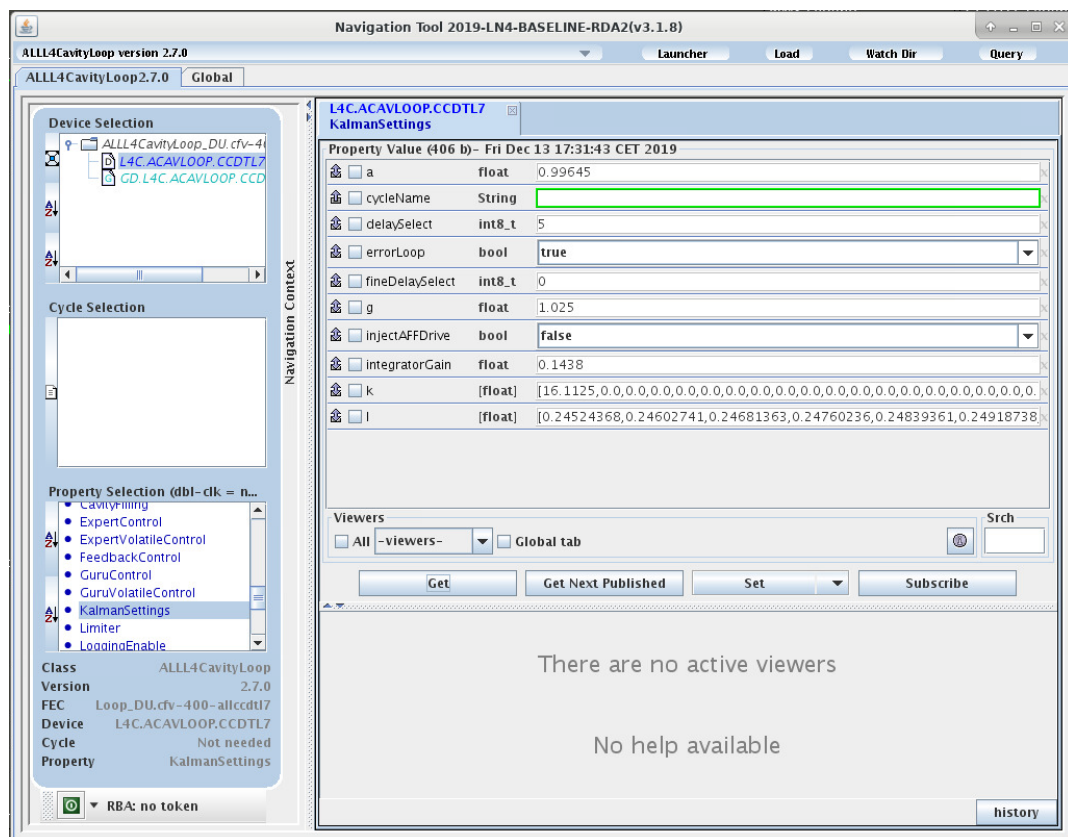


Figure A.5: CCCTL7 Kalman settings in the FESA navigator

Here all the parameters regarding the cavity loop can be set such as model parameters a , $delaySelect$ and g . Also the LQG *integratorGain*, state feedback vector k and the Kalman gain vector l .

The FESA classes parameters can also be accessed through a Python API called “PyJapc” [25]. It is easy to use, and is often the preferred choice to automate the parameter setting. An example of the usage can be seen in the following python code snippet of initialising PyJapc and getting/setting parameters.

```
1 import pyjapc
2
3 p = pyjapc.PyJapc()
4
5 p.setSelector("")
6
7 print(p.getParam("{device}/KalmanSettings"))
8
9 p.setParam("{device}/KalmanSettings", data_to_set)
```

This is used in the following chapter, where a description of how a Python Control toolbox was made to tune the LQG and Kalman gains for the cavities.

PYTHON CONTROL TOOLBOX

This chapter is included from the internship project [1] to support the theory and design of the Kalman observer and LQR controller in the thesis. This chapter explains how the algorithms for calculating the Kalman Gain vector and the LQR gains were implemented in python for automated setup and tuning of the cavities.

The LQG controllers designed in section 4.3 and simulated in section 3.2 will in this section be tested on several actual cavities. First section B.1 and B.2 will describe the implementation of a python control toolbox developed to automatically calculate the LQG and Kalman gains. This was previously done using Matlab, but as CERN is no longer considered as an educational institute, the cost of licenses have gone up drastically. Therefore the need for a custom in-house toolbox arose, and it was chosen to make a python implementation of well-known Matlab control algorithms. Also, the previous Matlab-Python implementation was not reliable. The matlab code was wrapped in a python container, where the python code was designed to start Matlab execute the control algorithms, write the Kalman and LQ gains to a text file, that can then be retrieved in python afterwards. The time required to startup matlab is not constant, and sometimes it would take too long, and the python code would time out. A flowchart of the python-matlab implementation can be seen in figure B.1. The first part of this chapter will explain how a python control toolbox will replace the blue matlab box.

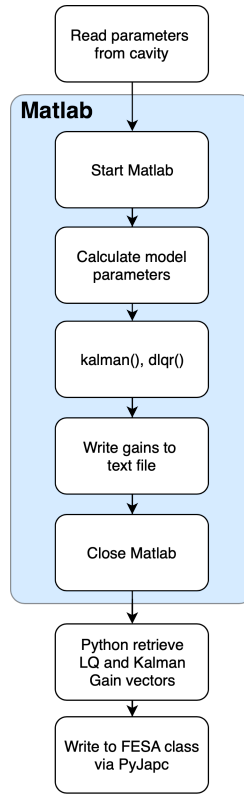


Figure B.1: Flowchart of the Python-Matlab implementation of calculating the LQ and Kalman gains and writing them to the cavity FESA class.

After the description of this implementation, testing the control schemes on several real cavities and a comparison between a full state feedback and a single state feedback controller will be presented in section 3.3.

B.1 IMPLEMENTATION OF A PYTHON TOOLBOX FOR CALCULATING KALMAN GAIN

A Kalman filter consist of mainly 6 equations presented in section 4.1. The two steps include an apriori prediction, and given some measurement data, the prediction is thereafter updated. However, as the state estimation is already implemented in the firmware, only the Kalman gain vector L needs to be calculated and written to the FESA class through PyJpc as described in A.2. This can be done in “open loop”, meaning only the model is needed - no actual data to calculate the Kalman gain. As the system is linear and a linear Kalman filter is used, it is expected that looping over 4 equations will eventually make the Kalman gain L converge. It was discovered that Matlab uses a slightly different algorithm than the one presented in

section 4.1. Matlab has a modified $P_{n|n-1}$ where instead of just adding the weight Q_n in the end, it is multiplied (squared) with Γ .

$$\begin{aligned}
 P_{n|n-1} &= \bar{\Phi}_n P_{n-1|n-1} \bar{\Phi}_n^T + \Gamma Q_n \Gamma^T \\
 S_n &= \bar{H}_n P_{n|n-1} \bar{H}_n^T + R_n \\
 L_n &= P_{n|n-1} \bar{H}_n^T S_n^{-1} \\
 P_{n|n} &= (I - L_n \bar{H}_n) P_{n|n-1}
 \end{aligned} \tag{B.1}$$

Programmatically this is done by initialising the equations to:

$$\begin{aligned}
 P_{n|n-1} &= 1 + \Gamma Q_n \Gamma^T \\
 S_n &= \bar{H}_n P_{n|n-1} \bar{H}_n^T + R_n \\
 L_n &= P_{n|n-1} \bar{H}_n^T S_n^{-1} \\
 P_{n|n} &= (I - L_n \bar{H}_n) P_{n|n-1}
 \end{aligned}$$

Secondly a variable L_{old} is introduced. This variable will be used in a while loop to check if the Kalman gain L_n has converged. L_{old} is initialised to $L_{old} = c + L_n$, where c is some constant to make sure that L_{old} is significantly different to L_n . The process itself of finding the converged gain L , is found in a while loop defined to iterate as long as the norm of L_n varies more than 0.01% different than the previous iteration. L_{old} is the Kalman gain of the previous iteration. When the gain has converged to within 0.01% of its previous value, the function will return L just like the Matlab implementation `kalman`. The code can be seen in the appendix in section B.3.

B.2 IMPLEMENTATION OF A PYTHON TOOLBOX FOR CALCULATING LQ CONTROLLER GAIN

The implementation of an algorithm for calculating the discrete LQ gains is of a similar structure to the Kalman algorithm presented in the previous section. By structure, it is meant, that a set of equations are iterated over until the LQ gain K is found. However, in contrast to the Kalman algorithm where the equations are iterated over until the gain converges, there are for LQ algorithms mainly two methods of iterating, namely with either *finite* or *infinite horizon*. The *infinite horizon*

case is similar to the case of the Kalman gain, where a while loop iterates until the gain K converges. The *finitehorizon* is as the name suggests, a loop that iterates a finite number of times, defined by a prediction horizon N . The equations for calculating the LQ gain K has previously been presented in section 4.3, and are outlined below.

$$K_s = \left(R + \bar{\Gamma}^T S_{n+1} \bar{\Gamma} \right)^{-1} \bar{\Gamma}^T S_{n+1} \bar{\Phi} \quad (\text{B.2})$$

$$S_n = Q + \bar{\Phi}^T S_{n+1} \bar{\Phi} - K_s^T \bar{\Gamma}^T S_{n+1} \bar{\Phi} \quad (\text{B.3})$$

First S_n is initialised to be equal to the weight matrix Q , the first iteration of K and S is calculated before entering the loop of calculating the gain. For the *infinite* case, the function returns a single K , specifically the one that converged. The *finite* case returns a vector K of N length. The code of the implementation can be seen in the appendix section B.4.

B.3 KALMAN GAIN CODE

```

1 def _kalman(Phi, Gamma, H, Q, R):
2
3     P_k_p = 1 + mul(mul(Gamma, Q), Gamma.transpose())
4     S_k = mul(mul(H, P_k_p), H.transpose()) + R
5     S_k_inv = np.linalg.inv(S_k)
6     L_k = mul(mul(P_k_p, H.transpose()), S_k_inv)
7     P_k_k = mul((np.eye(L_k.shape[0]) - mul(L_k, H)), P_k_p)
8
9     L_old = (10 + L_k)
10
11     while np.linalg.norm(L_k - L_old) > 0.0001 * np.linalg.norm(L_k):
12
13         L_old = L_k
14
15         P_k_p = mul(mul(Phi, P_k_k), Phi.transpose()) + mul(mul(Gamma, Q), Gamma.
16             ↪ transpose())
17
18         S_k = mul(mul(H, P_k_p), H.transpose()) + R
19
20         S_k_inv = np.linalg.inv(S_k)
21
22         L_k = mul(mul(P_k_p, H.transpose()), S_k_inv)
23
24         P_k_k = mul((np.eye(L_k.shape[0]) - mul(L_k, H)), P_k_p)
25
26     return L_k, P_k_k

```

B.4 LQ GAIN CODE

```

1 def _infinite(Phi, Gamma, Q, R):
2
3     S = Q # Initial value of the solution to the discrete algebraic ricatti
4         ↪equation (DARE)
5
6     K_old = -1 # Initial value of the previous gain. (only used in the first
7         ↪iteration)
8
9     # Calculate first iteration of gain (K) and solution (S) to DARE
10    K = mul(mul(mul(np.linalg.inv(R + mul(mul(Gamma.transpose(), S), Gamma)), Gamma
11        ↪.transpose()), S), Phi)
12
13    S = Q + mul(mul(Phi.transpose(), S), Phi) - mul(mul(mul(K.transpose(), Gamma.
14        ↪transpose()), S), Phi)
15
16    # loop until K gain stabilises to within 0.01% of its previous value.
17    while np.linalg.norm(K-K_old) > 0.0001*np.linalg.norm(K):
18
19        K_old = K
20
21        K = mul(mul(mul(np.linalg.inv(R + mul(mul(Gamma.transpose(), S), Gamma)),
22            ↪Gamma.transpose()), S), Phi)
23
24        S = Q + mul(mul(Phi.transpose(), S), Phi) - mul(mul(mul(K.transpose(),
25            ↪Gamma.transpose()), S), Phi)
26
27    return K, S, 'infinite'
28
29 def _finite(Phi, Gamma, Q, R, N):
30
31    n = Phi.shape[0] # Number of rows in Phi
32    p = Gamma.shape[1] # Number of columns in Gamma
33
34    # Initial value of the solution to the discrete algebraic ricatti equation (
35        ↪DARE)
36    S = Q
37
38    # Calculate first iteration of gain (K) and solution (S) to DARE
39    Kp = mul(mul(mul(np.linalg.inv(R + mul(mul(Gamma.transpose(), S), Gamma)),
40        ↪Gamma.transpose()), S), Phi)
41
42    S = Q + mul(mul(Phi.transpose(), S), Phi) - mul(mul(mul(Kp.transpose(), Gamma.
43        ↪transpose()), S), Phi)
44
45    K = np.zeros((p, n, N-1))
46
47    for k in range(N-1, 0, -1):
48
49        Kp = mul(mul(mul(np.linalg.inv(R + mul(mul(Gamma.transpose(), S), Gamma)),
50            ↪Gamma.transpose()), S), Phi)
51
52        S = Q + mul(mul(Phi.transpose(), S), Phi) - mul(mul(mul(Kp.transpose(),
53            ↪Gamma.transpose()), S), Phi)
54
55        K[0:p, 0:n, k-1] = Kp
56
57    return K, S, 'finite'

```

LINAC4 COMMISSIONING

This chapter is included from the internship project [1] to showcase a different task during the authors stay at CERN.

C.1 COMMISSIONING OF LINAC4

This is not considered as part of the report, but it is something the author aided with during the internship. LINAC4 is the newest linear particle accelerator at CERN. During the fall of 2019 it had to be commissioned after some hardware upgrade. The commissioning of LINAC4 took place in various control rooms and a Farady Cage at CERN. The process involved setting up the cavity loops from scratch and setting up the Adaptive Feed-Forward (AFF), to correct for beam loading. This chapter will not go into detail with the process, but merely highlight a few moments during the 2-3 week commissioning process. In figure C.1 the main building housing all the electronics and amplifiers for LINAC4 can be seen. The picture shows the radiation area housing all the Klystrons that provide the RF power to the cavities.



Figure C.1

Figure C.2 is a picture of the process of setting up the AFF filter, where it is discussed how well the beam loading is corrected for.



Figure C.2

Figure C.3 is a picture of the Faraday cage for LINAC4 housing all the sensitive hardware running the cavity loops, and getting the feedback from the cavities. Each cavity has its own rack containing various timing and control equipment. In the foreground to the left a computer with access to the cavities can be seen. These were used during setup and commissioning of the machine.



Figure C.3

Figure C.4 is a picture from the RF control room again showing some setup of the AFF filter on a different cavity.

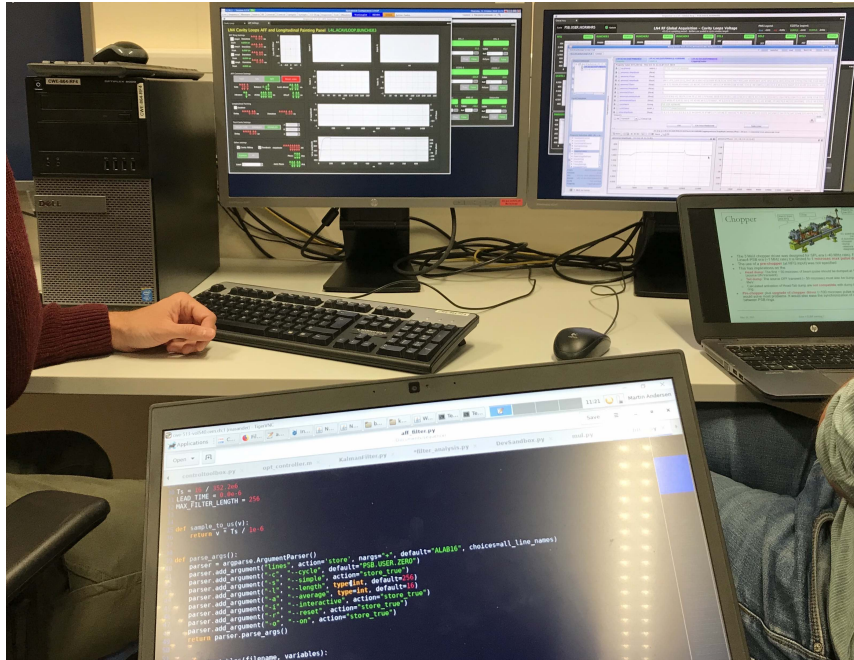


Figure C.4

MODELLING

This chapter takes a different approach to modelling the RF accelerating cavity as a 2nd order system, namely keeping the complex terms in the model. The model derived here is not put on state space form, or used for any control design, but merely presented as an alternative approach to modelling the system.

D.1 MODELLING A PARTICLE ACCELERATING RF CAVITY AS A 2ND ORDER SYSTEM

The LCR circuit presented forming the basis of the model is of 2nd order as it contains two components to store energy, namely both an inductor and a capacitor. An assumption was made that the second order term would have little effect as it is weighted by the inverse squared angular frequency $\frac{1}{\omega^2}$, and the model therefore shifted to 1st order. While this might be perfectly adequate for designing control strategies from a result based engineering perspective, from an academic perspective, it is interesting to investigate how a second order system potentially differs, and if there is gains to be made in the control strategies either in performance, stability or robustness.

This section will therefore derive a 2nd order model by continuing from equation 2.13, but keeping the second order term. The referenced equation is repeated below for convenience.

$$2I_g(t) - I_b(t) = \frac{1}{L} \int V(t)dt + C \frac{dV(t)}{dt} + V(t) \left(\frac{1}{R} + \frac{1}{Z} \right) \quad (2.13 \text{ revisited})$$

As in the previous 1st order model, the derivative and integral of $V(t)$ is to be found. The derivative of $V(t)$ was found to be:

$$\frac{dV(t)}{dt} = \left(i\omega A(t) + \frac{dA(t)}{dt} \right) e^{i\omega t} \quad (2.15 \text{ revisited})$$

The integral of $V(t)$ after a few iterations of integration by parts was found to be:

$$\int V(t)dt = \left(\frac{A(t)}{i\omega} + \frac{1}{\omega^2} \frac{dA(t)}{dt} \right) e^{i\omega t} + \int \frac{1}{\omega^2} \frac{d^2 A(t)}{dt^2} e^{i\omega t} dt \quad (2.17 \text{ revisited})$$

This is where the 2nd order model will differ from the 1st order progression. Another iteration of integration by parts is needed to keep the second order term:

$$\begin{aligned} \int V(t)dt &= \left(\frac{A(t)}{i\omega} + \frac{1}{\omega^2} \frac{dA(t)}{dt} \right) e^{i\omega t} + \frac{1}{i\omega^3} e^{i\omega t} \frac{d^2 A(t)}{dt^2} - \int \frac{1}{i\omega^3} \frac{d^3 A(t)}{dt^3} e^{i\omega t} dt \\ &= \left(\frac{A(t)}{i\omega} + \frac{1}{\omega^2} \frac{dA(t)}{dt} + \frac{1}{i\omega^3} \frac{d^2 A(t)}{dt^2} \right) e^{i\omega t} - \int \frac{1}{i\omega^3} \frac{d^3 A(t)}{dt^3} e^{i\omega t} dt \end{aligned} \quad (D.1)$$

The last integral term containing the third derivative term, can be neglected, mainly due to the system only being second order, but also that the third order derivative weighted by the inverse angular frequency cubed is expected to be a very small number. Therefore the final integral of $V(t)$ can be defined as:

$$\int V(t)dt = \left(\frac{A(t)}{i\omega} + \frac{1}{\omega^2} \frac{dA(t)}{dt} + \frac{1}{i\omega^3} \frac{d^2 A(t)}{dt^2} \right) e^{i\omega t} \quad (D.2)$$

Inserting the new expression for $\int V(t)$ and the expression for $\frac{dV(t)}{dt}$ into equation 2.13 yields:

$$\begin{aligned} 2I_g(t) - I_b(t) &= \frac{1}{L} \left(\frac{A(t)}{i\omega} + \frac{1}{\omega^2} \frac{dA(t)}{dt} + \frac{1}{i\omega^3} \frac{d^2 A(t)}{dt^2} \right) e^{i\omega t} \\ &\quad + C \left(i\omega A(t) + \frac{dA(t)}{dt} \right) e^{i\omega t} + A(t) e^{i\omega t} \left(\frac{1}{R} + \frac{1}{Z} \right) \end{aligned} \quad (D.3)$$

As in the first order model, according to [12] all variables including $I_g(t)$ and $I_b(t)$ are proportional to $e^{i\omega t}$. By therefore dividing by $e^{i\omega t}$ results in:

$$\begin{aligned} 2I_g(t) - I_b(t) &= \frac{1}{L} \left(\frac{A(t)}{i\omega} + \frac{1}{\omega^2} \frac{dA(t)}{dt} + \frac{1}{i\omega^3} \frac{d^2 A(t)}{dt^2} \right) + C \left(i\omega A(t) + \frac{dA(t)}{dt} \right) \\ &\quad + A(t) \left(\frac{1}{R} + \frac{1}{Z} \right) \end{aligned}$$

Multiplying out the parentheses to put $A(t)$, $\frac{dA(t)}{dt}$ and $\frac{d^2A(t)}{dt^2}$ outside parentheses:

$$\begin{aligned}
 2I_g(t) - I_b(t) &= \frac{A(t)}{Li\omega} + \frac{1}{L\omega^2} \frac{dA(t)}{dt} + \frac{1}{Li\omega^3} \frac{d^2A(t)}{dt^2} + Ci\omega A(t) \\
 &\quad + C \frac{dA(t)}{dt} + \frac{A(t)}{R} + \frac{A(t)}{Z} \\
 2I_g(t) - I_b(t) &= \left(\frac{1}{Li\omega} + Ci\omega + \frac{1}{R} + \frac{1}{Z} \right) A(t) + \left(\frac{1}{L\omega^2} + C \right) \frac{dA(t)}{dt} \\
 &\quad + \left(\frac{1}{Li\omega^3} \right) \frac{d^2A(t)}{dt^2}
 \end{aligned}$$

Just like the 1st order model case, restructuring the equation a bit helps introduce cavity specific relations later on.

$$\begin{aligned}
 2I_g(t) - I_b(t) &= \left(-\frac{i}{L\omega} + Ci\omega + \frac{1}{R} + \frac{1}{Z} \right) A(t) + C \left(\frac{1}{LC\omega^2} + 1 \right) \frac{dA(t)}{dt} \\
 &\quad + C \left(-\frac{i}{LC\omega^3} \right) \frac{d^2A(t)}{dt^2} \\
 2I_g(t) - I_b(t) &= \left(Ci\omega \left(1 - \frac{1}{\omega^2 LC} \right) + \frac{1}{R} + \frac{1}{Z} \right) A(t) + C \left(\frac{1}{\omega^2 LC} + 1 \right) \frac{dA(t)}{dt} \\
 &\quad + C \left(-\frac{i}{\omega^3 LC} \right) \frac{d^2A(t)}{dt^2} \tag{D.4}
 \end{aligned}$$

In resonant parallel circuits, there exists a relation $\omega_0 = \frac{1}{\sqrt{LC}}$, and therefore: [17]

$$LC = \frac{1}{\omega_0^2}$$

Using this relation will therefore transform equation D.4 into:

$$\begin{aligned}
2I_g(t) - I_b(t) &= \left(Ci\omega \left(1 - \frac{\omega_0^2}{\omega^2} \right) + \frac{1}{R} + \frac{1}{Z} \right) A(t) + C \left(1 + \frac{\omega_0^2}{\omega^2} \right) \frac{dA(t)}{dt} \\
&\quad + C \left(-\frac{i\omega_0^2}{\omega^3} \right) \frac{d^2A(t)}{dt^2} \\
2I_g(t) - I_b(t) &= \left(Ci\omega - \frac{Ci\omega_0^2}{\omega} + \frac{1}{R} + \frac{1}{Z} \right) A(t) + C \left(\frac{\omega^2}{\omega^2} + \frac{\omega_0^2}{\omega^2} \right) \frac{dA(t)}{dt} \\
&\quad - C \left(\frac{i\omega_0^2}{\omega^3} \right) \frac{d^2A(t)}{dt^2} \\
2I_g(t) - I_b(t) &= \left(Ci \frac{(\omega^2 - \omega_0^2)}{\omega} + \frac{1}{R} + \frac{1}{Z} \right) A(t) + \left(C \frac{(\omega^2 + \omega_0^2)}{\omega^2} \right) \frac{dA(t)}{dt} \\
&\quad - Ci \left(\frac{\omega_0^2}{\omega^3} \right) \frac{d^2A(t)}{dt^2} \tag{D.5}
\end{aligned}$$

Detuning can now be introduced $\Delta\omega = \omega_0 - \omega$, such that the three parts including ω_0 becomes:

$$\begin{aligned}
(\omega^2 - \omega_0^2) &= \omega^2 - (\Delta\omega + \omega)^2 \\
&= \omega^2 + \Delta\omega^2 - \omega^2 - 2\omega\Delta\omega \\
&= -2\omega\Delta\omega
\end{aligned}$$

$$\begin{aligned}
(\omega^2 + \omega_0^2) &= \omega^2 + (\Delta\omega + \omega)^2 \\
&= \omega^2 + \Delta\omega^2 + \omega^2 + 2\omega\Delta\omega \\
&= 2\omega^2 + 2\omega\Delta\omega
\end{aligned}$$

$$\begin{aligned}
\omega_0^2 &= (\Delta\omega + \omega)^2 \\
&= \Delta\omega^2 + \omega^2 + 2\omega\Delta\omega \\
&= \omega^2 + 2\omega\Delta\omega
\end{aligned}$$

As the cavity is expected to be close to in-tune, $\Delta\omega$ is expected to be small, and therefore its square, $\Delta\omega^2$ can be neglected in all of the above cases. Using these three expressions, and inserting them in equation D.5 results in:

$$\begin{aligned}
 2I_g(t) - I_b(t) &= \left(-2i\Delta\omega C + \frac{1}{R} + \frac{1}{Z} \right) A(t) + \left(C \frac{2\omega^2 + 2\omega\Delta\omega}{\omega^2} \right) \frac{dA(t)}{dt} \\
 &\quad - Ci \left(\frac{\omega^2 + 2\omega\Delta\omega}{\omega^3} \right) \frac{d^2A(t)}{dt^2} \\
 2I_g(t) - I_b(t) &= \left(-2i\Delta\omega C + \frac{1}{R} + \frac{1}{Z} \right) A(t) + 2C \left(1 + \frac{\Delta\omega}{\omega} \right) \frac{dA(t)}{dt} \\
 &\quad - Ci \left(\frac{1}{\omega} + \frac{2\Delta\omega}{\omega^2} \right) \frac{d^2A(t)}{dt^2} \tag{D.6}
 \end{aligned}$$

Now as in the first order case C , R and Z has to be expressed in terms of cavity parameters. Expressions for these, have previously been found to be:

$$C = \frac{1}{\omega(R/Q)} \tag{2.28 revisited}$$

$$R = Q_0(R/Q) \tag{2.30 revisited}$$

$$z = Q_{ext}(R/Q) \tag{2.31 revisited}$$

Using these relations equation D.6 becomes:

$$\begin{aligned}
 2I_g(t) - I_b(t) &= \left(-2i\Delta\omega \frac{1}{\omega(R/Q)} + \frac{1}{Q_0(R/Q)} + \frac{1}{Q_{ext}(R/Q)} \right) A(t) \\
 &\quad + 2 \frac{1}{\omega(R/Q)} \left(1 + \frac{\Delta\omega}{\omega} \right) \frac{dA(t)}{dt} \\
 &\quad - \frac{1}{\omega(R/Q)} i \left(\frac{1}{\omega} + \frac{2\Delta\omega}{\omega^2} \right) \frac{d^2A(t)}{dt^2} \tag{D.7}
 \end{aligned}$$

$$I_g(t) = \left(-2i\frac{\Delta\omega}{\omega} + \frac{1}{Q_0} + \frac{1}{Q_{ext}} \right) \frac{A(t)}{2(R/Q)} + \left(\frac{1}{\omega(R/Q)} + \frac{\Delta\omega}{\omega^2(R/Q)} \right) \frac{dA(t)}{dt} - \left(\frac{i}{2\omega^2(R/Q)} + \frac{2i\Delta\omega}{\omega^3(R/Q)} \right) \frac{d^2A(t)}{dt^2} + \frac{I_b(t)}{2}$$

Just as in the first order case, the cavity is coupled with a transmission line, and a loaded quality factor Q_L can be introduced $\frac{1}{Q_L} = \frac{1}{Q_0} + \frac{1}{Q_{ext}}$ [19]:

$$I_g(t) = \left(\frac{1}{Q_L} - 2i\frac{\Delta\omega}{\omega} \right) \frac{A(t)}{2(R/Q)} + \left(\frac{1}{\omega(R/Q)} + \frac{\Delta\omega}{\omega^2(R/Q)} \right) \frac{dA(t)}{dt} - \left(\frac{i}{2\omega^2(R/Q)} + \frac{2i\Delta\omega}{\omega^3(R/Q)} \right) \frac{d^2A(t)}{dt^2} + \frac{I_b(t)}{2}$$

$$\left(I_g(t) - \frac{I_b(t)}{2} \right) \omega(R/Q) = \left(\frac{\omega}{2Q_L} - i\Delta\omega \right) A(t) + \left(1 + \frac{\Delta\omega}{\omega} \right) \frac{dA(t)}{dt} - \left(\frac{i}{2\omega} + \frac{2i\Delta\omega}{\omega^2} \right) \frac{d^2A(t)}{dt^2}$$

$V(t)$ can now be substituted back in for $A(t)$ to end up with the final dynamics:

$$\left(I_g(t) - \frac{I_b(t)}{2} \right) \omega(R/Q) = \left(\frac{\omega}{2Q_L} - i\Delta\omega \right) V(t) + \left(1 + \frac{\Delta\omega}{\omega} \right) \frac{dV(t)}{dt} - \left(\frac{i}{2\omega} + \frac{2i\Delta\omega}{\omega^2} \right) \frac{d^2V(t)}{dt^2}$$

$$\left(\frac{i}{2\omega} + \frac{2i\Delta\omega}{\omega^2} \right) \frac{d^2V(t)}{dt^2} = \left(\frac{\omega}{2Q_L} - i\Delta\omega \right) V(t) + \left(1 + \frac{\Delta\omega}{\omega} \right) \frac{dV(t)}{dt} - \left(I_g(t) - \frac{I_b(t)}{2} \right) \omega(R/Q) \quad (D.8)$$

Isolating $\frac{d^2V(t)}{dt^2}$ in the above equation would result in the complex 2nd order dynamics of the voltage in an RF accelerating cavity.